1225-0767(ISSN Print)
2287-6715(ISSN Online)
한국연구재단 우수등재학술지

Journal of Ocean Engineering and Technology

Vol. 37, No. 3 (Serial Number 172) June 2023

한국해양공학회지

KSOE

www.joet.org

KSOE The Korean Society of Ocean Engineers

Journal of Ocean Engineering and Technology
한국해양공학회지
Vol. 37 No. 3
(Serial Number 172)
June 30, 2023
www.JOET.org

Published on June 30, 2023
Published by The Korean Society of Ocean Engineers (KSOE)
Room 1302, 13, Jungang-daero 180beon-gil, Dong-gu, Busan, 48821, Korea
TEL: +82-51-759-0656 FAX: +82-51-759-0657 E-mail: ksoehj@ksoe.or.kr URL: http://www.ksoe.or.kr
Printed by Hanrimwon Co., Ltd., Seoul, Korea E-mail: hanrim@hanrimwon.co.kr
ISSN(print) 1225-0767 **ISSN(online)** 2287-6715

This journal was supported by the Korean Federation of Science and Technology Societies (KOFST) grant funded by the Korean government.

Journal of Ocean Engineering and Technology
한국해양공학회지

CONTENTS

Volume 37, Number 3 June, 2023

<Original Research Articles>

GENERAL INFORMATION

The **"Journal of Ocean Engineering and Technology" (JOET)** was launched in 1987 and is published bimonthly in February, April, June, August, October, and December each year by "The Korean Society of Ocean Engineers (KSOE)." Its ISO abbreviation is "J. Ocean Eng. Technol." JOET publishes original research articles, technical articles, and review articles on all aspects of ocean engineering, including experimental, theoretical, numerical, and field observations. All manuscripts undergo peer-review by two or more reviewers.

The scope of JOET encompasses the following research areas:

- Ships and offshore engineering:

  Design of ships and offshore structures; Resistance and propulsion; Seakeeping and maneuvering; Experimental and computational fluid dynamics; Ocean wave mechanics; Fatigue strength; Plasticity; Optimization and reliability; Arctic technology and extreme mechanics; Noise, vibration, and acoustics; Concrete engineering; Thermodynamics and heat transfer; Hydraulics and pneumatics; Autonomous and unmanned ship; Greenship technology; Digital twin of ships and offshore structures; Marine materials

- Coastal engineering:

  Coastal, port, and harbor structures; Waves transformation; Coastal and estuary hydrodynamics; Sediment transport and morphological change; Subsea geotechnics; Coastal groundwater management; Prevention or mitigation of coastal disaster; Coastal zone development and management; Shore protection technique; Coastal environmental process; Beach safety

- Ocean energy engineering:

  Offshore wind turbines; Wave energy platforms; Tidal current energy platforms; Floating photovoltaic energy platform; Small modular reactor; Combined energy platforms

- Marine robot engineering:

  Robot sensor system; Autonomous navigation; Robot equipment; Marine robot control; Environment mapping and exploration; Underwater communication and networking; Design of marine robots

 It is indexed in databases such as the Korean Citation Index (KCI), Google Scholar, Science Central, Korea Science, and the Directory of Open Access Journals (DOAJ). JOET offers PDF or XML versions for free on its website (https://www.joet.org). For business matters, authors need to contact KSOE Secretariat by email or phone (e-mail: ksoehj@ksoe.or.kr or Tel: +82 51 759 0656). Correspondences for publication matters can be asked via email to the Editor-in-Chief (e-mail: heroeswise2@gmail.com).

KSOE

Journal of Ocean Engineering and Technology 37(3), 81-88, June, 2023
https://doi.org/10.26748/KSOE.2023.008

pISSN 1225-0767
eISSN 2287-6715

Original Research Article

Study on the Development of the Maneuvering Mathematical Model Considering the Large Angle Motion of Submarine

Jae Hyuk Choi[1], Sungwook Lee[2] and Jinhyeong Ahn[3]

[1]*Graduated Student, Dept. of Naval Architecture and Ocean Systems Engineering, Korea Maritime and Ocean University, Busan, Korea*
[2]*Associate Professor, Dept. of Naval Architecture and Ocean Systems Engineering, Korea Maritime and Ocean University, Busan, Korea*
[3]*Principal Research Engineer, Maritime Technology Research Institute - 1st Directorate, Agency for Defense Development, Jinhae, Korea*

KEYWORDS: Submarine, Large motion, CFD, Maneuvering, Mathematical model

ABSTRACT: *Maneuverability is a crucial factor for the safety and success of submarine missions. This paper introduces a mathematical model that considers the large drift and angle of attack motions of submarines. Various computational fluid dynamics (CFD) simulations were performed to adapt Karasuno's fishery vessel maneuvering mathematical model to submarines. The study also presents the procedure for obtaining the physics-based hydrodynamic coefficients proposed by Karasuno through CFD calculations. Based on these coefficients, the reconstructed forces and moments were compared with those obtained from CFD and to the hydrodynamic derivatives expressed by a Taylor expansion. The study also discusses the mathematical maneuvering model that accounts for the large drift angles and angles of attack of submarines. The comparison results showed that the proposed maneuvering mathematical model based on modified Karasno's model could cover a large range of motions, including horizontal motion and vertical motions. In particular, the results show that the physics-based mathematical maneuvering model can represent the forces and moments acting on the submarine hull during large drift and angle of attack motions. The proposed mathematical model based on the Karasuno model could obtain more accurate results than the Taylor third-order approximation-based mathematical model in estimating the hydrodynamic forces acting on submarines during large drift and angle of attack motions.*

1. Introduction

In the design of submarines, frequent reviews are conducted regarding the hydrodynamic characteristics acting on the hull. A review of the hydrodynamic characteristics may include speed performance, maneuverability, and exceptional purpose performance. Generally, shipyards and research institutions worldwide have accumulated data (model tests, sea trials, and numerical analysis) based on their technology, research, development, and experience in surface ships for an extended period. These data are used frequently in the initial and detailed design of surface ships. On the other hand, in the case of submarines, unlike in surface ships, only a minimal amount of model test data, sea trial data, and numerical analysis data can be relied upon. This situation is also characterized by significantly reduced accessibility. Furthermore, in the case of submarines, the maneuvering performance in underwater operation is mentioned as an important factor closely related to submarine construction. In particular, submarines require considering the maneuvering performance for six degrees of freedom (DOF) of the hull, which makes it more challenging to deal with than maneuvering surface ships.

Thus far, the performance estimation of submarine maneuverability has followed the same procedure (using the mathematical model of maneuvering motion based on captive model tests) as that used in surface ships, but the complexity of the procedure must be considered as the degree of freedom of the considered maneuvering increases.

On the other hand, a representative method of estimating maneuvering performance using the six degrees of freedom (hereinafter 6DOF) maneuvering mathematical model proposed by Gertler and Hagen (1967) and Feldman (1979) is to use the mathematical model-based methods for submarine maneuvering. Generally, in methods based on mathematical models, it is essential to obtain hydrodynamic derivatives, which are the hydrodynamic forces included in the mathematical model. In the case of submarines, it is also essential to obtain hydrodynamic forces acting on the hull

Received 14 April 2023, revised 30 May 2023, accepted 14 June 2023
Corresponding author Sungwook Lee: +82-51-410-4303, swlee@kmou.ac.kr

using the same approach. Several methods of captive model tests, theoretical calculations, and empirical equations are used to obtain hydrodynamic derivatives that act on the hull during submarine maneuvering. On the other hand, captive model tests are mainly used for submarines. Nevertheless, these mathematical model-based maneuvering performance estimation methods are mainly for the 6DOF motion of the general submarine (hereafter normal motion), and it is difficult to apply them to emergency rising motion, one of the special maneuvers of submarines (hereafter excessive motion).

Generally, the mathematical models used to represent the hydrodynamic forces included in the equations of motion of a submarine in normal motion use Taylor's third-order approximation expression for a multivariate function with the motion states of a submarine as variables. These mathematical models are represented considering the accuracy and complexity of the equations, based on the assumption that submarine motion is not excessive. On the other hand, the assumption that submarine motion is not excessive is no longer valid, and Taylor's third-order approximation expression is no longer valid when the submarine performs low-speed or emergency maneuvers. Hence, if the terms of Taylor's approximation are extended to higher-order terms of the third order, the expression for the hydrodynamic forces becomes more complex, and the expression becomes even more complicated because the six-degrees-of-freedom motion must be considered. Therefore, studies have been conducted to represent hydrodynamic forces more concisely and reflect physical phenomena more rigorously. Hooft (1994) proposed a mathematical model that separates the hydrodynamic forces acting on the surface ship hull into linear and nonlinear terms and expresses the linear term based on slender body theory and the nonlinear term based on cross-flow drag based on the drag coefficient when the yaw angle is 90°. Bohlmann (1990) proposed a similar mathematical model proposed by Hooft for submarines. Shin et al. (2005) applied the same mathematical model as Bohlmann (1990) to submarines and validated the proposed mathematical model using theoretical equations for various submarines. Furthermore, Watt (2007) proposed a mathematical model that includes a Fourier series form of a multivariable function representing the hydrodynamic forces acting on a submarine when it moves at various angles based on a mathematical model similar to Gertler and Hargen (1976). Park et al. (2017) proposed a mathematical model that uses a polynomial function form of a multivariable function instead of a Fourier series form, similar to Watt (2007) model. Although the mathematical models proposed by Watt (2007) and Park et al. (2017) considered the behavior of submarines at various angles, they have limitations in that they do not consider large-angle motions.

Karasuno et al. (1991, 1992) proposed a new mathematical model for maneuvering a fishing vessel with a large drift maneuvering motion. The mathematical model suggested by Karasuno et al. is composed of fluid dynamic coefficients commonly used in aerodynamics (such as lift and drag coefficients) and cross-flow drag coefficients. Karasuno et al.'s research presents results that can express various maneuvering motions, including forward, backward, and large turning motions of a fishing vessel. The mathematical model proposed by Karasuno et al. does not use complex coefficients and has the advantage of incorporating physical meaning into the coefficients and describing turning motion using the hydrodynamic coefficients obtained from the drift motion. Therefore, this study examined the applicability of the mathematical model proposed by Karasuno et al. for a submarine and proposed a mathematical model applicable to a submarine. Chapter 2 introduces the 6DOF maneuvering equations of a submarine and the hydrodynamic mathematical model proposed by Karasuno. In Chapter 3, large drift angle and angle of attack calculations are performed on horizontal and vertical planes using computational fluid dynamics (CFD) for the MARIN BB2. Chapter 4 confirms the utility of the mathematical model by deriving the hydrodynamic coefficients proposed by Karasuno et al. from these calculations and comparing them with the calculation results of the existing Taylor 3rd approximation formula.

2. Mathematical Model for the Maneuvering Motion of Submarine

2.1 6DOF Maneuvering Equation of Motion for Submarine

Assuming a submarine as a rigid body and symmetric about the *x-z* plane, the 6DOF maneuvering equation of motion for the submarine can be expressed as Eqs. (1)–(6) using Newton's equations of motion, with a coordinate system fixed to a submarine as shown in Fig. 1 (Sohn et al., 2006).

Each force and moment includes the hull, propeller, elevator and stern plane, and hydrostatic forces, and the superscripts $\cdot$ and G indicate differentiation with respect to time and the center of gravity, respectively. As mentioned in the introduction, the forces and moments on the left-hand side of Eqs. (1)–(6) can be expressed using the equations proposed by Gertler and Hargen (1967) or Kim et al. (2021). As stated previously, this study proposes a mathematical model using a new approach for these external forces and validates the model accuracy. This study investigated the applicability of Karasuno et al.'s mathematical model to submarines.

$$X = m\left\{\dot{u} + qw - ru - x_G(q^2 + r^2) + z_G(pr + \dot{q})\right\} \tag{1}$$

$$Y = m\left\{\dot{v} + ru - pw + z_G(qr - \dot{p}) + x_G(qp + \dot{r})\right\} \tag{2}$$

$$Z = m\left\{\dot{w} + pv - qu - z_G(p^2 + q^2) + x_G(rp - \dot{q})\right\} \tag{3}$$

$$K = I_{xx}\dot{p} + (I_{zz} - I_{yy})qr - m\left\{z_G(\dot{v} + ru - pw) + x_G z_G(pq + \dot{r})\right\} \tag{4}$$

$$\begin{aligned} M = {} & I_{yy}\dot{q} + (I_{xx} - I_{zz})rp + m\left\{z_G(\dot{u} + qw - ru)\right. \\ & \left. - x_G(\dot{w} + pv - qu) + x_G z_G(p^2 - r^2)\right\} \end{aligned} \tag{5}$$

$$N = I_{zz}\dot{r} + (I_{yy} - I_{xx})pq + m\left\{x_G(\dot{v} + ru - pw) + z_G x_G(rq - \dot{p})\right\} \tag{6}$$

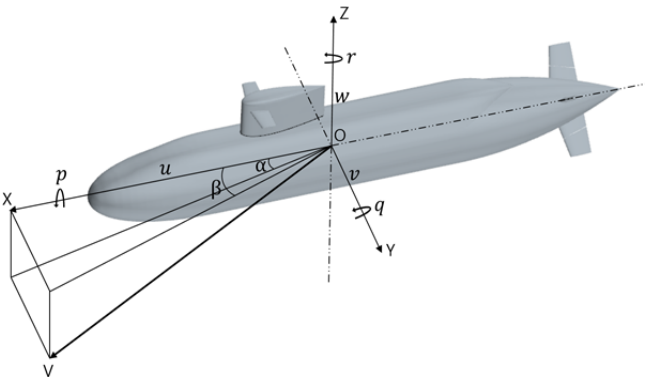

Fig. 1 Coordinate system

2.2 Physical-Based Hydrodynamic Model (Karasuno Model)

Karasuno et al. separated the hydrodynamic forces acting on the hull in a situation where the submarine is moving (Fig. 2) into seven elements: Munk moment, lift, drag, cross-flow lift, cross-flow drag, frictional force, and correction force due to the stall.

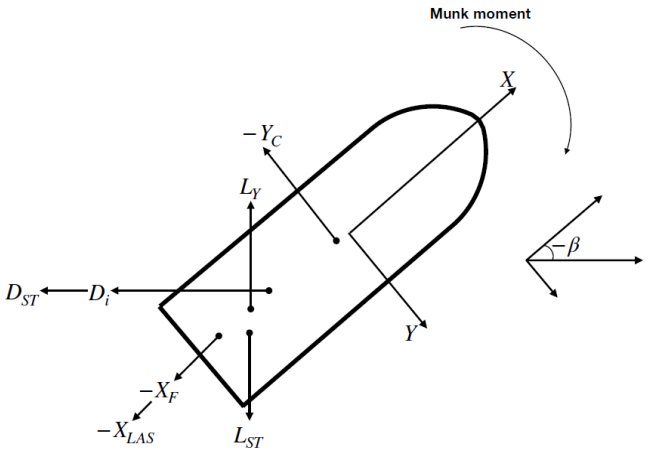

Fig. 2 Components of the hydrodynamic forces and moment proposed by Karasuno et al. (1991, 1992)

Table 1 lists the seven elements that make up the mathematical model proposed by Karasuno et al. (1991, 1992)

In the formulae presented in Table 1, the symbol ′ represents a non-dimensional value; u and v represent the longitudinal velocity and the transverse velocity, respectively; U represents the total speed of the submarine; m and m' represent mass and transverse addedmass, respectively; L_{pp} represents the length of the hull; ΔC_L and ΔC_{Di} represent the lift and drag correction coefficients due to stall, respectively; C_L and C_{Di} represent the lift and drag coefficients; C_{D90} represents the cross-flow drag coefficient; C_F is the friction coefficient; m_0 and m_1 represent the area and first moment of the lateral projection of the body center, respectively. Using the seven elements in Table 1, the force and moment acting on the body can be expressed as Eqs. (7)–(9).

$$X' = C'_L \cdot u' \cdot v' - C'_{Di} \cdot u'^3 \cdot v'^2 - (\Delta C'_L u' \cdot v'^2 - \Delta C'_{Di} u'^3 \cdot v'^2) - C'_{LAS} \cdot v'^2 - C'_F \cdot |u'| \cdot u' \quad (7)$$

$$Y' = C'_L \cdot u'^2 \cdot v' - C'_{Di} \cdot u'^2 \cdot v'^3 - C_{D90} \cdot m'_0 \cdot (1 + p \cdot cos^2\beta) \cdot v'^3 \quad (8)$$

$$N' = (m'_x - m'_y) \cdot u'v' - C'_L l'_{v0} \cdot u'^2 \cdot v' - C'_{Di} \cdot l'_{i0} \cdot u'^2 \cdot v'^3 - C_{D90} \cdot m'_1 \cdot (1 + p \cdot cos^2\beta) \cdot v'^3 \quad (9)$$

Here, where l'_{v0} and l'_{i0} represent the lever moment's lever due tobecause the lift and drag forces, respectively, and $(1 + p \cdot cos^2\beta)$ is a term introduced to correct the cross-flow drag. Eqs. (7)–(9) represents the hydrodynamic forces and moment acting on the hull, and to use it in the equations of motion, it is necessary to obtain the seven elements that make upin Eqs. (7)–(9) to use it in the equations of motion. To obtain each element, Karasuno et al. proposed an analysis procedure using a fishing vessel as the target ship to obtain each element, as described listed in Table 2.

Table 1 Detailed information for each element of hydrodynamic force and moment from Karasuno's mathematical model

Component force or moment	Mathematical expression
Munk moment	$(m_x' - m'_y)u'v'$
Lift	$L_c = \frac{1}{2}\rho L_{pp} dU^2 C_L' u'v'$
Drag	$D_i = \frac{1}{2}\rho L_{pp} dU^2 C_{Di}' u'^2 v'^2$
Cross-flow drag	$Y_c = \frac{1}{2}\rho L_{pp} dU^2 C_{D90} m'_0 v'^3$, $N_c = \frac{1}{2}\rho L_{pp}^2 dU^2 C_{D90} m'_1 v'^3$
Cross-flow lift	$X_{LAS} = \frac{1}{2}\rho L_{pp} dU^2 C_{LAS}' v'^2$
Friction	$X_F = \frac{1}{2}\rho L_{pp} dU^2 C_F' \lvert u' \rvert u'$
Correction force for stall effect	$(L_{ST}' + D_{ST}')_x = -\Delta C_L' u'v'^2 + \Delta C_{Di}' u'^3 v'^2$

Table 2 Analysis procedure for obtaining the hydrodynamic coefficient of Karasuno's model

Hydrodynamic coefficients	Descriptions
$C_{D90}\cdot m_0'$, $C_{D90}\cdot m_1'$	When drift angle β = 90°, obtaining $C_{D90}\cdot m_0'$ and $C_{D90}\cdot m_1'$ from $u'=0$, $v'=1$ and the experiment or calculation (Y' and N')
C_L', $C_L'\cdot l_{vo}'$	When drift angle β = 0°–30°, obtaining C_L' after removing known terms ($C_{D90}\cdot m_0'$) from the experiment or calculation (Y' and N') by using least square method
C_{Di}', $C_{Di}'\cdot l_{i0}'$, p	When drift angle β = 0°–90°, obtaining C_{Di}' after removing known terms($C_{D90}\cdot m_0'$, C_L') from the experiment or calculation (Y' and N') by using least square method
C_F', C_{LAS}'	When drift angle β = 0°, obtaining C_F'(=Resistance coefficient) and when drift angle β = 90°, obtaining C_{LAS}' after removing known terms ($C_{D90}\cdot m_0'$, C_L', $C_{Di}'$and C_F') from the experiment or calculation (X') by using the least square method
$\Delta C_L'$, $\Delta C_{Di}'$	When drift angle β = 0°–90°, obtaining $\Delta C_L'$ and $\Delta C_{Di}'$ after removing known terms obtained from previous procedures from the experiment or calculation (X') by using the least square method
$L_{ST}+D_{ST}$	When drift angle β = 0°–30°, obtaining $L_{ST}+D_{ST}$ after removing known terms obtained from previous procedures from the experiment or calculation by using the least square method

3. Numerical Analysis

3.1 Numerical Method

Chapter 2 introduced the physics-based mathematical model proposed by Karasuno et al. to estimate the hydrodynamic forces for the six degrees of freedom motion of a submarine at large angles of attack in detail. As previously mentioned, model tests or numerical calculations are necessary to obtain the hydrodynamic forces suggested in the Karasuno model. For submarines, however, facilities capable of performing model tests for large drift angle motions (or large angle of attack motion) are rare compared to surface ships. Furthermore, this study presents a methodology for reconstructing the hydrodynamic forces based on the proposed mathematical model using information obtained from model tests or numerical calculations. Therefore, this study performed numerical analysis using CFD instead of model tests. The commercial CFD software STAR-CCM+ was used for the numerical analysis, and Table 3 lists the basic numerical techniques used in this study. In addition, all forces and moments in this study were non-dimensionalized using Eq. (10).

$$F'=\frac{F}{0.5\rho L^2V^2},\quad M'=\frac{M}{0.5\rho L^3V^2} \tag{10}$$

MARIN BB2 in Table 4 was selected as a target ship, and CFD analysis was performed with the conditions listed in Table 5 and shown in Fig. 3.

Table 3 Numerical setup

Item	Description
Code	STAR-CCM+ V.16
Turbulence model	Reynolds Stress model
Temporal / Convection term	Backward / 2nd order upwind
Grid type	Unstructured grid (Trimmer)
Pressure-Velocity coupling	Unsteady SIMPLE

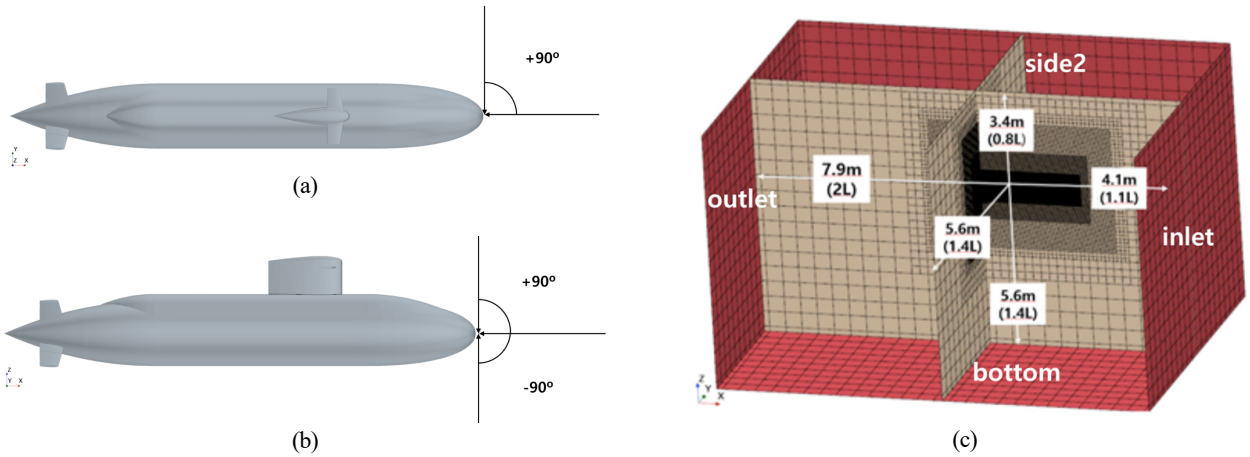

Fig. 3 Calculation conditions for the CFD calculation: (a) Definition of flow direction for horizontal motion; (b) Definition of flow direction for vertical motion; (c) Layout of the domain for CFD calculations

Table 4 Main particulars of MARIN BB2

Vessel	Full scale	Model scale
Lpp (m)	70.2	3.826
Breadth (m)	9.6	0.5232
Draft to deck (m)	10.6	0.5777
Displacement (m^3)	4440	0.7012
LCG from nose	32.31	1.761
VCG from kell	4.90	0.267
Scale Ratio	1	18.348

Table 5 Conditions for CFD calculation

Motion	Velocity (m/s)	Drift angle	Angle of attack
Horizontal	1.2009	0°–90° (interval: 10°)	0°
Vertical	1.2009	0°	-90° to 90° (interval: 10°)

3.2 Calculation Results for Horizontal Static Drift and Vertical Static Angle of Attack Motion

Fig. 4(a) shows the calculation results for the horizontal static motion. The longitudinal force (in green), lateral force (in orange), and pitching moment (in blue) increase Aas the yaw angle increases according to Fig. 4. On the other hand, the longitudinal and lateral forces decreased around yaw angles of 75° and 60°. The pitching moment reached a maximum around the yaw angle of 50° and then decreased. In the case of horizontal static motion, only the yaw angles from 0° to 90° were calculated because the submarine shape is symmetric, and they did not consider the astern motion. The lateral force decreased due to the strong backflow caused by the flow separation from the submarine sail and hull after the yaw angle of 60°, and the pitching moment also decreased due to the same effect (Choi, 2023).

Fig. 4(b) shows the calculation results for the vertical static angle of attack motion. As shown in Fig. 4, the longitudinal force (in green), vertical force (in orange), and pitching moment (in blue) increase as the angle of attack increases. On the other hand, the vertical force decreased around the trim angle of 80°. The pitching moment reached its maximum around the angle attack of 20° before decreasing slightly between 20° and 50° and then increased again around 60° before decreasing. In addition, complex flow patterns were formed for a negative angle of attack as the flow passing through the hull encounters the sail, leading to different characteristics than the positive angle of attack and showing asymmetry in force and moment (Choi, 2023).

4. Discussion

Fig. 5 compares the reconstructed vertical force (Karasuno, black) using the hydrodynamic coefficients obtained from the procedure described in Table 2 and the vertical force obtained by Taylor third-order approximation ($Z = Z_{w}' \cdot w' + Z_{www}' \cdot w'^{3}$) with the CFD result (blue). In Fig. 5(a), the coefficients for constructing Taylor third-order approximation (Taylor, orange) were obtained from the CFD values in the range of negative angles (α = 0°–20°) and used to predict the large angle values. In Fig. 5(b), the coefficients were obtained from the CFD values in the range of the large angles (α = 0°–90°) and used to predict large angle values.

First, the reconstructed lateral force using the Karasuno model generally reproduced the CFD results well. On the other hand, the mathematical model using Taylor third-order approximation showed relatively good results up to an angle of attack of 50°, but it failed to reproduce the CFD values from an angle of attack of 60° and above. Moreover, although the mathematical model using Taylor third-order approximation generally reflects the trends of the CFD results, a significant difference was observed between the two in the entire range, as shown in Fig. 5(b). The order of the hydrodynamic coefficients in the approximation equation could be increased to more than a fifth-order term to reduce the error of the mathematical model using Taylor approximation. As mentioned in the introduction, introducing higher-order terms complicates the maneuvering equations of the submarine.

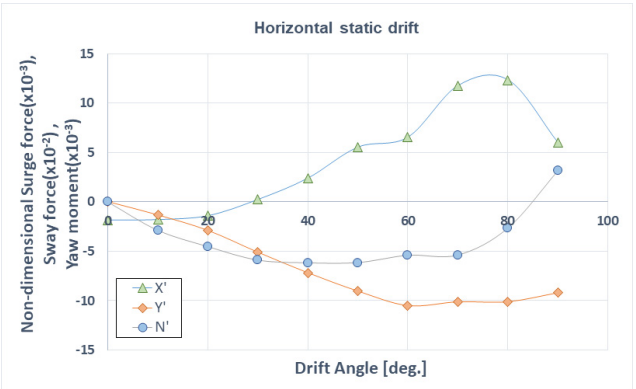

(a)

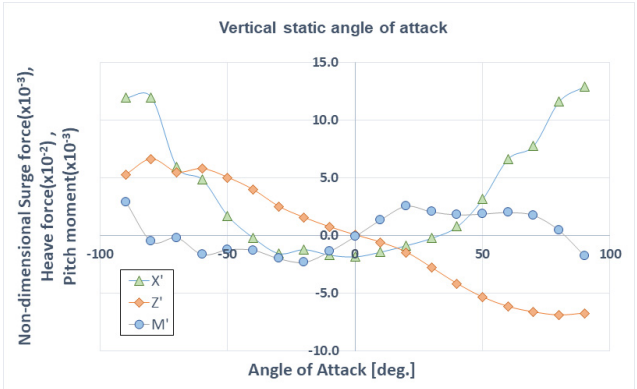

(b)

Fig. 4 Calculation results for the horizontal motion and the vertical motion: (a) Horizontal forces and moment depending on the static drift motion; (b) Vertical forces and moment depending on the static angle of attack motion

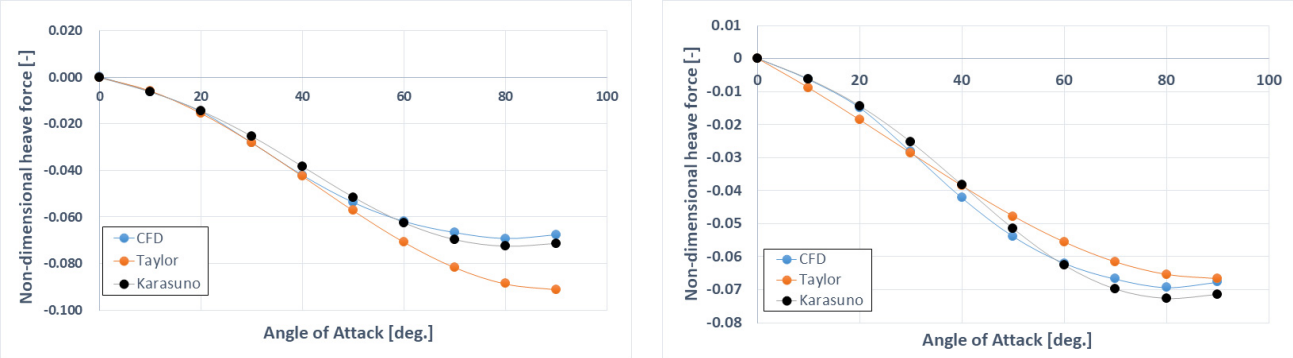

(a) (b)

Fig. 5 Comparison results between CFD and two mathematical models for the vertical force: (a) Curve fitting for Taylor-type mathematical model using the coefficients obtained between the vertical angle of attack from 0° to 20°; (b) Curve fitting for Taylor-type mathematical model using the coefficients obtained between the vertical angle of attack from 0° to 90°

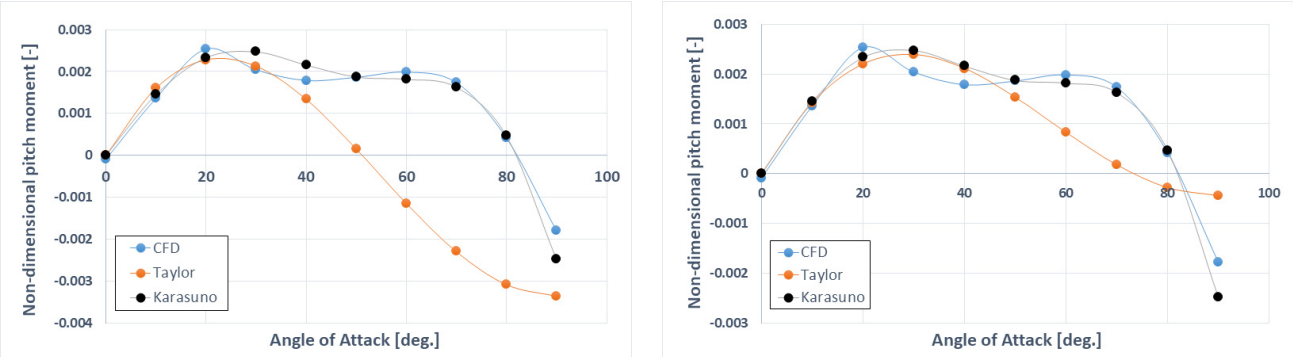

(a) (b)

Fig. 6 Comparison results between the CFD and two mathematical models for the pitch moment: (a) Curve fitting for Taylor-type mathematical model using the coefficients obtained between the vertical angle of attack from 0° to 20°; (b) Curve fitting for Taylor-type mathematical model using the coefficients obtained between the vertical angle of attack from 0° to 90°

Fig. 6 shows the comparison result between the reconstructed pitch moment (Karasuno, black) using the lift coefficients obtained from CFD calculations by the procedure described in Table 2 as mentioned above, and the pitch moment (Taylor, orange) obtained by Taylor third-order approximation ($M = M_w{}' \cdot w' + M_{www}{}' \cdot w'^3$), compared to the CFD results (blue). Among these results, Fig. 6(a) shows the reconstructed pitch moment over the range of angles of attack (hereafter AOA) (α = 0°–90°) using the lift coefficient obtained from the CFD values in the AOA range (α = 0°–20°) in the analysis of vertical force., and Fig. 6(b) shows the reconstructed pitch moment at the large AOA range (α = 0°–90°) using the lift coefficient obtained from the CFD values in the large AOA range (α = 0°–90°).

The Karasuno model relatively well reconstructed the CFD results over the entire range (Fig. 6), while the Taylor third-order approximation showed good results up to 30° AOA in Fig. 6(a), but showed significant differences from the CFD results at the large AOA (Fig. 6(b)), similar to the results in the vertical force. Similar results are obtained for the lateral force and yaw moment caused by the large drift motion (Choi, 2023), indicating the utility of the Karasuno model proposed in this study for the large drift/AOA motion.

5. Modified Karasuno Model

In this study, the applicability of the mathematical model proposed by Karasuno et al. was confirmed using CFD with a submarine as a target ship. In particular, it is proposed as expressed in Eqs. (11) and (12) below.

Horizontal motion

$$
\begin{aligned}
X' &= C_L^{hh\prime}u'v'^2 - C_{Di}^{hh\prime}u'^3v'^2 - \left(\Delta C_L^{hh\prime}u'v'^2 - C_{Di}^{hh\prime}u'^3v'^2\right) \\
&\quad - C_{LAS}^{hh'}v'^2 - C_F^{hh\prime}|u'|u' + C_L^{hv\prime}u'w'^2 - C_{Di}^{hv\prime}u'^3w'^2 \\
&\quad - \left(\Delta C_L^{hv\prime}u'w'^2 - C_{Di}^{hv\prime}u'^3w'^2\right) - C_{LAS}^{hv'}w'^2 - C_F^{hv\prime}|u'|u' \\
Y' &= C_L^{hh\prime}u'^2v' - C_{Di}^{hh\prime}u'^2v'^3 - C_{D90}^{hh}m_0{}'\left(1+\cos^2\beta\right)v'^3 \\
&\quad + C_L^{hv\prime}u'^2w' - C_{Di}^{hv\prime}u'^2w'^3 - C_{D90}^{hv}m_0{}'\left(1+\cos^2\alpha\right)w'^3 \\
N' &= \left(m_x{}' - m_y{}'\right)u'v' - C_L^{hh\prime}l_{v0}^{hh\prime}u'^2v' - C_{Di}^{hh\prime}l_{i0}^{hh\prime}u'^2v'^3 \\
&\quad - C_{D90}^{hh}m_1{}'\left(1+\cos^2\beta\right)v'^3 - C_L^{hv\prime}l_{v0}^{hv\prime}u'^2w' \\
&\quad - C_{Di}^{hv\prime}l_{i0}^{hv\prime}u'^2w'^3 - C_{D90}^{hv}m_1{}'\left(1+\cos^2\alpha\right)w'^3
\end{aligned}
\tag{11}
$$

Table 6 All hydrodynamic coefficient for Karasuno's model obtained from CFD calculations

Hydrodynamic coefficients	Values	Hydrodynamic coefficients	Values
$C_{D90}^{hh} \cdot m_0'$	-0.2021	$C_{D90}^{hh} \cdot m_1'$	-0.001
$C_{D90}^{vv} \cdot m_0'$	0.1124	$C_{D90}^{vv} \cdot m_1'$	0.0018
$C_L^{hh'}$	-0.1191	$C_L^{hh'} \cdot l_{vo}^{hh'}$	0.0119
$C_L^{vv'}$	0.0554	$C_L^{vv'} \cdot l_{vo}^{vv'}$	0.0091
$C_{Di}^{hh'}$	-0.1090	$C_{Di}^{hh'} \cdot l_{i0}^{hh'}$	0.0098
$C_{Di}^{vv'}$	0.0152	$C_{Di}^{vv'} \cdot l_{i0}^{vv'}$	0.0188
$C_F^{hh'}$	0.0019	$C_{LAS}^{hh'}$	-0.0060
$C_F^{vv'}$	0.0019	$C_{LAS}^{vv'}$	-0.0129
$\Delta C_L^{hh'}$	-0.1420	$\Delta C_{Di}^{hh'}$	-0.1444
$\Delta C_L^{vv'}$	0.0633	$\Delta C_{Di}^{vv'}$	0.0114

Vertical motion

$$
\begin{aligned}
X' &= C_L^{vv'}u'w'^2 - C_{Di}^{vv'}u'^3w'^2 - \left(\Delta C_L^{vv'}u'w'^2 - C_{Di}^{vv'}u'^3w'^2\right) \\
&\quad - C_{LAS}^{vv'}w'^2 - C_F^{vv'}|u'|u' + C_L^{vh'}u'v'^2 - C_{Di}^{vh'}u'^3v'^2 \\
&\quad - \left(\Delta C_L^{hh'}u'v'^2 - C_{Di}^{vh'}u'^3v'^2\right) - C_{LAS}^{vh'}v'^2 - C_F^{vh'}|u'|u' \\
Z' &= C_L^{v'}u'^2w' - C_{Di}^{v}{}'u'^2w'^3 - C_{D90}^{v}m_0'(1+\cos^2\alpha)w'^3 \\
&\quad + C_L^{vh'}u'^2v' - C_{Di}^{vh'}u'^2v'^3 - C_{D90}^{vh}m_0'(1+\cos^2\alpha)v'^3 \\
M' &= (m_x' - m_z')u'w' - C_L^{v'}l_{v0}^{v}{}'u'^2w' - C_{Di}^{v}{}'l_{i0}^{v}{}'u'^2w'^3 \\
&\quad - C_{D90}^{v}m_1'(1+\cos^2\alpha)w'^3 - C_L^{vh'}l_{v0}^{vh'}u'^2v' \\
&\quad - C_{Di}^{vh'}l_{i0}^{vh'}u'^2v'^3 - C_{D90}^{vh}m_1'(1+\cos^2\alpha)v'^3
\end{aligned}
\tag{12}
$$

The superscript, hh, vv, hv and vh in Eqs. (11) and (12) represent the direction of the forces acting on the submarine, which depend on the direction of motion. Therefore, the superscripts hh and vv denote "forces acting in the same direction as the motion". In contrast, the superscript vh denotes "forces acting in the vertical direction due to horizontal motionmotion," and hv denotes "forces acting in the horizontal direction due to vertical motion". From their meanings, they represent the coupling term. The coupling terms that have the superscripts and can be ignored in the normal maneuvering motion of a submarine, but these coupling terms cannot be ignored in the special maneuvering motion, such as emergency rising or low-speed operation. In the present study, these coupling terms were ignored because of the lack of proven evidence. Table 6 lists all hydrodynamic coefficients obtained from CFD calculation.

6. Conclusions

This study applied the mathematical model proposed by Karasuno et al. to the maneuvering motion of a submarine using CFD to confirm its applicability. In particular, the forces and moments acting on the submarine during significant drift and angle of attack motions were calculated and used to derive the hydrodynamic coefficients used in the Karasuno model. A mathematical model based on Taylor's third-order approximation was used to reconstruct the hydrodynamic force acting on the submarine during large drift and transverse motions. The results were compared with those obtained using Karasuno's physically-based mathematical model. The following results were obtained:

(1) It was confirmed that the Karasuno model could obtain more accurate results than the Taylor third-order approximation-based mathematical model in estimating the hydrodynamic forces acting on the submarine during large drift and angle of attack motions.

(2) To use the Taylor approximation-based mathematical model to estimate the hydrodynamic forces acting on the submarine hull during a large drift and angle of attack motions, it is necessary to extend the order of the approximation equation to higher-order terms.

Nevertheless, more research will be needed to introduce additional terms for the hydrodynamic forces acting in the vertical plane direction during horizontal motion and in the horizontal plane direction during vertical motion. Second, while this study focused only on large drift and angle of attack motions, further research on the rotational and turning motions of submarines will be necessary.

Conflict of Interest

The authors declare that they have no conflict of interest.

Funding

This study was supported by the Agency Defense Development by the Korean Government in 2021−2022 (UD210002DD).

References

Bohlmann, H. (1990). *Berechnung hydrodynamischer Koeffizienten von Ubooten zur Vorhersage des Bewegungsverhaltens.* Technische Universität Hamburg-Harburg.

Choi, J. H. (2023). *A study on the development of the mathematical model considering the large angle motion of submarine* [Master's thesis, Korea Maritime and Ocean University]. https://kmou.dcollection.net/public_resource/pdf/200000669584_20230615005033.pdf

Feldman, J.(1979). *Revised standard submarine equations of motion* (DTNSRDC/SPD-0393-09). David W. Taylor /naval Ship Research and Development Center.

Gertler, M., & Hagen, G. (1967). *Standard equations of motion for submarine simulation* (NSRDC Report 2510).

Hooft, J. (1994). The cross-flow drag on a manoeuvring ship. *Ocean Engineering, 21*(3), 329−342. https://doi.org/10.1016/0029-8018(94)90004-3

Karasuno, K., Matsuno, T. I., & Igarashi, K. (1991). The mathematical model of hydrodynamic forces acting on ship moving in an oblique direction with fluid-dynamic concepts (2nd report). *Journal of the Kansai Society of naval architectures, Japan, 216*, 175−183.

Karasuno, K., Matsuno, T. I., & Igarashi, K. (1992). A new mathematical model of hydrodynamic forces and moment acting on a hull during maneuvering motion that occurs under conditions of slow speed and large turns (2nd report). *Journal of the Kansai Society of naval architects, Japan, 217*, 125−135.

Kim, Y., Kim, D., Yun, K., Lee, Y., Jeong, S., & Lee, G. (2021). Prediction of maneuverability of submarine by captive model test. *Proceedings of the Annual Autumn Conference of the Society of Naval Architects of Korea*.

Park, J., Kim, N., & Shin, Y. (2017). Experimental study on hydrodynamic coefficients for high-incidence-angle maneuver of a submarine, International Journal of Naval Architecture and Ocean Engineering, 9,100−113.

Shin, Y., & Lee, S. (2005). A study on the modeling of hydrohynamic coefficient for the emergency maneuver simulation of underwater vehicle. *Journal of Society of Naval Architect of Korea, 42*(6), 601−607.

Sohn, K., Lee, S., & Ha, S., (2006). Mathematical model for dynamics of manta-type unmanned undersea vehicle with six degree of freedom and characteristics of manoeuvrability response. *Journal of Society of Naval Architect of Korea, 43*(4), 399−413.

Watt, G. D. (2007). *Modelling and simulating unsteady six degrees-of-freedom submarine rising maneuvers* (Technical Report DRDC Atlantic TR 2007-008). Defence R & D Canada − Atlantic.

Author ORCIDs

Author name	ORCID
Choi, Jae Hyuk	0000-0003-4090-6774
Lee, Sungwook	0000-0001-6089-303X
Ahn, Jinhyeong	0009-0003-1389-0831

KSOE

Journal of Ocean Engineering and Technology 37(3), 89-98, June, 2023
https://doi.org/10.26748/KSOE.2023.006

pISSN 1225-0767
eISSN 2287-6715

Original Research Article

Experimental and Numerical Study on the Characteristics of Free Surface Waves by the Movement of a Circular Cylinder-Shaped Submerged Body in a Single Fluid Layer

Jun-Beom Kim[1], Eun-Hong Min[1,2] and Weoncheol Koo[3]

[1]*Researcher, Department of Naval Architecture and Ocean Engineering, Inha University, Incheon, Korea*
[2]*Researcher, Department of Ocean Engineering, Texas A&M University, Texas, USA*
[3]*Professor, Department of Naval Architecture and Ocean Engineering, Inha University, Incheon, Korea*

KEYWORDS: Free surface, Two-dimensional mini-towing tank, Jet-like flow, Wave breaking, Submerged moving body, Numerical towing tank

ABSTRACT: *Analyzing the interactions of free surface waves caused by a submerged-body movement is important as a fundamental study of submerged-body motion. In this study, a two-dimensional mini-towing tank was used to tow an underwater body for analyzing the generation and propagation characteristics of free surface waves. The magnitude of the maximum wave height generated by the underwater body motion increased with the body velocity at shallow submerged depths but did not increase further when the generated wave steepness corresponded to a breaking wave condition. Long-period waves were generated in the forward direction as the body moved initially, and then short-period waves were measured when the body moved at a constant velocity. In numerical simulations based on potential flow, the fluid pressure changes caused by the submerged-body motion were implemented, and the maximum wave height was accurately predicted; however, the complex physical phenomena caused by fluid viscosity and wave breaking in the downstream direction were difficult to implement. This research provides a fundamental understanding of the changes in the free surface caused by a moving underwater body.*

1. Introduction

Free surface waves can be generated by water bodies (e.g., ships) or submerged bodies (e.g., submarines) that move at constant speeds (Journee and Massie, 2001). At infinite water depths, the flow around a submerged body causes various flow phenomena according to the geometry of the object and the flow velocity with no interaction with the free surface, and many relevant insights have been obtained from fluid dynamics. In contrast, the flow of a submerged body moving under the free surface forms free surface waves, causing complex physical phenomena according to the geometry, velocity, and submerged depth of the object. Therefore, many studies have been conducted to understand such phenomena. When a submerged body in the form of a cylinder, which is the most basic geometry, moves under the free surface, a jet-like flow occurs between the body and free surface, and free surface wave depression is generated behind the cylinder because of the rapid pressure change, as shown in Fig. 1

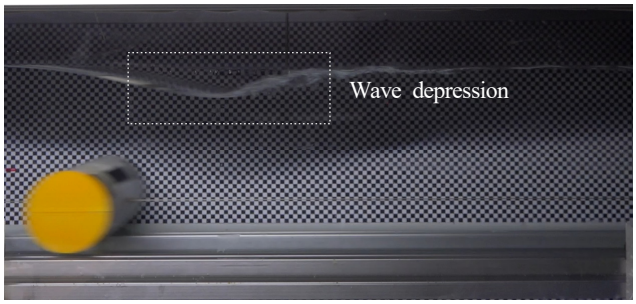

Fig. 1 Free surface wave depression caused by submerged cylinder motion

(Sheridan et al., 1997).

This depression phenomenon becomes more obvious as the submerged depth of the submerged body decreases and its velocity increases (Yi et al., 2013; Shin and Cho, 2021). In addition, a breaking wave occurs in the depression, affecting the formation of rear free surface waves (Hyun and Shin, 2000).

Received 12 April 2023, revised 12 May 2023, accepted 23 May 2023
Corresponding author Weoncheol Koo: +82-32-860-7348, wckoo@inha.ac.kr

Studies on the geometry of rear free surface waves generated by the motion of a cylindrical submerged body have long been conducted using analytical or numerical methods, and in most of them, the free surface displacement generated behind the submerged body was calculated by applying an incident wave or flow velocity to a fixed cylinder (Dean, 1948; Ursell, 1950; Scullen and Tuck, 1995). However, this fundamentally differs from the free surface displacement caused by the direct movement of the submerged body, and the aforementioned studies had limitations in identifying the phenomena of free surface waves caused by complex interactions between the submerged body and the free surface. This is because they focused on the hydrodynamic analysis of the phenomena of free surface waves generated behind the submerged body; the actual movement of the body was not modeled. As various free surface waves caused by the acceleration of the submerged body from the stationary state are mixed with those caused by the movement of the body at a constant velocity, it is necessary to accurately simulate the motion of the submerged body through towing experiments to analyze the complex interactions affected by the geometry, velocity, and submerged depth of the body.

In general, the generation and propagation of free surface waves are calculated with potential flow that assumes the incompressible, non-rotational, and non-viscous flow of fluid (Journee and Massie, 2001). Potential flow-based numerical analysis has been commonly applied to the motion analysis of ocean waves and floating bodies using the boundary element method. In particular, time- and frequency-domain analysis for floating body motion has been widely conducted via modeling under the same conditions as an experimental tank through the numerical wave tank (NWT) technique (Uzair and Koo, 2012; Min and Koo, 2017; Min and Koo, 2022). This numerical analysis technique was used to model the motion of a submerged body and calculate free surface waves according to the submerged depth and velocity of the submerged body (Holloway and Davis, 2002; Kim et al., 2019; Seong et al., 2022). In particular, Seong et al. (2022) reproduced the free surface waves caused by the motion of a submerged body with a National Advisory Committee for Aeronautics geometry (NACA0034) using the NWT technique and validated their method through a comparison with experimental results.

In addition, various studies on the flow characteristics under submerged-body motion have been conducted using computational fluid dynamics (CFD). Various studies have been reported, in which researchers implemented changes in the free surface waves caused by the underwater motion of a simple cylinder (Mnasri et al., 2014), analyzed the dynamic characteristics of a submerged body through the adjustment of the drift angle and the angle of attack (Jeon et al., 2021), analyzed the flow noise of a submarine-shaped underwater body using CFD and computational acoustics (Ren et al., 2023), and performed spectrum analysis for the free surface waves caused by the motion of submarine- and whale-shaped underwater bodies through experiments and CFD (Liu and Guo, 2013).

To understand the complex phenomena associated with wave generation and propagation caused by the flow change between a moving submerged body and a free surface, an accurate numerical analysis conducted under various experimental conditions is required, and the phenomena must be identified through a precise experiment in which the submerged body is towed directly. Experimental research in which complex flow phenomena were measured by directly towing a submerged body is rare, and basic research is needed to analyze complex flow phenomena by directly towing a submerged body in the presence of a free surface.

In this study, acceleration and constant-velocity regions were created by directly towing a cylindrical submerged body in water to precisely identify the interactions between the body and free surface, as well as the flow changes. In addition, the generation and propagation of free surface waves were measured, and their characteristics were analyzed. In contrast to streamlined objects, a cylinder easily causes flow separation and vortices on its surface owing to fluid viscosity, making it relatively easy to identify the complex physical phenomena that occur around the cylinder. Potential flow-based numerical analysis was conducted using a two-dimensional numerical towing tank that modeled the acceleration and constant velocity of the submerged body under the experimental conditions, and the results were compared with the experimental results. By comparing the experimental measurements that included fluid viscosity and the results of potential flow-based numerical analysis, the effects of the fluid viscosity on the geometry and propagation of the free surface waves caused by the submerged body motion were identified. The objective of this study was to clarify the generation and propagation characteristics of the free surface caused by the movement of a cylindrical submerged body and provide basic data. If these basic data are accumulated, they are expected to be used for applied studies, e.g., involving the detection of underwater bodies moving under free surfaces.

2. Submerged-Body Towing Experiment and Numerical Analysis

2.1 Two-dimensional Towing Tank

In this study, an experiment was performed using a towing tank that can directly tow a submerged body in a single fluid environment. The vertical displacement of the generated free surface waves was measured, and their propagation characteristics were analyzed according to the submerged depth of the submerged body and the towing velocity. Fig. 2 shows the cylindrical submerged body model connected to the rail support on the side wall of the two-dimensional towing tank with a wire. In the towing-tank experiment (Kim et al., 2022a), the two-dimensional submerged-body towing tank of Inha University was used. The specifications of the cylinder and towing tank are presented in Table 1. It was possible to clearly observe the displacement and propagation of the free surface because the walls of the tank are made of a transparent acrylic material, its frames are made of aluminum, and its bottom is made of polyvinyl chloride. The

Table 1 Dimensions of the two-dimensional towing tank and submerged body

Object	Parameter	Dimension (m)
Towing tank	Tank length (L)	5.8
	Tank width (B)	0.2
	Water depth (H)	0.77
	Rail length (L_r)	4
	Wave gauge location (L_g)	2.8
Submerged cylinder	Body diameter (D)	0.084
	Body width (W)	0.19
	Body position from tank bottom (h)	0.395

cylindrical submerged body was divided into upper and lower hemispheres to allow a wire to pass through, and the cylinder was formed by fastening four 3-mm-diameter bolts. The width of the submerged body was set equal to that of the two-dimensional towing tank to minimize the interference of the tank walls with the formation and propagation of free surface waves. Fig. 3 shows an overview of the towing-tank experiment. For the submerged-body towing system, the submerged body was connected to the wire installed underwater and was directly towed using the wire drum connected to the servomotor. The system did not directly interfere with the free surface, because it towed the submerged body with the wire. The system made it possible to observe the exact free surface displacement caused by the submerged-body motion, ensuring the reliability of the experimental results. Additionally, the submerged body could be accelerated from the stationary state and towed at a constant velocity.

The submerged-body towing system was used to tow the submerged body at a constant velocity. Fig. 4 shows the wire drum connected to the alternating-current (AC) servomotor installed in the towing tank. It towed the submerged body at a precise velocity along the rail installed on the tank wall by circulating the wire shown in Fig. 3. The wire connected to the submerged body passed through the centerline of the body. The tension of the wire acted on the center of gravity of the submerged body, causing translational motion. For the towing system, the towing velocity and towing distance were adjusted through the Programmable Multi Axis Controller (PMAC) software.

The free surface waves generated by the submerged body were accurately measured using a servo-type wave gauge (PCA-WH60S). This wave gauge can measure the vertical displacement of a free surface every 0.01 s (100 Hz) with a precision of up to 0.056 mm using water as a conductor. Proper tension must be maintained in the underwater wire for stable towing of the submerged body. In the experiment, the overall tension of the towing system was controlled by adjusting the pulley connected to the wire in the vertical direction.

Fig. 2 Submerged cylinder installed in a two-dimensional mini-towing tank

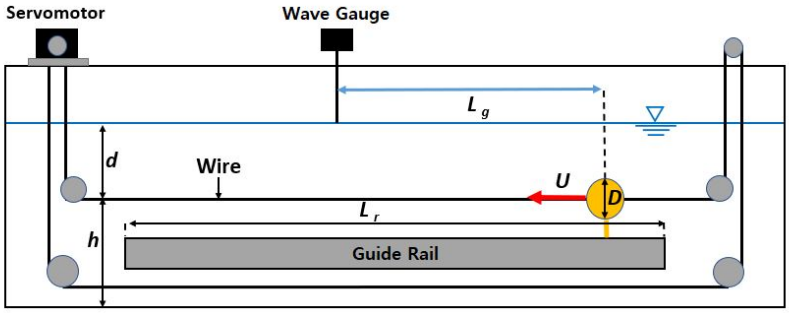

Fig. 3 Experimental setup for towing the submerged cylinder

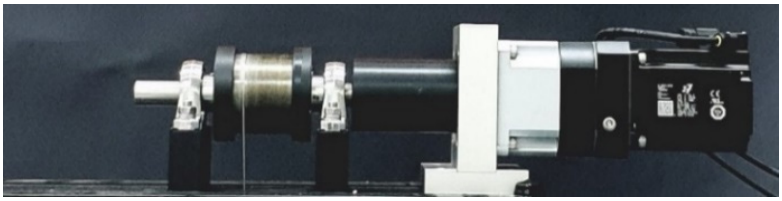

Fig. 4 AC servomotor and wire drum for towing the submerged body

2.2 Two-dimensional Numerical Towing Tank

To validate the experimental results, a numerical analysis was performed using a two-dimensional numerical towing tank modeled according to the experimental towing tank. Fig. 5 shows a schematic of the numerical towing tank, whose specifications are those presented in Table 1. However, the numerical towing tank did not need the underwater rail or wire, because it could move the submerged body precisely at the fixed velocity every hour. While the cylindrical submerged body was accelerated from the stationary state and subjected to the constant-velocity translational motion in the same manner as the experimental conditions, the displacement and propagation pattern of the free surface were calculated in the time domain. The two-dimensional numerical towing tank was detailed in previous works (Seong et al., 2022; Kim et al., 2022b). It was briefly described in this paper because the accuracy and reliability of the solution were verified.

2.2.1 Governing equations and boundary conditions

In the fluid field used for numerical analysis, the surface tension of the free surface was neglected, and non-viscous, incompressible, and non-rotational potential flow was assumed. Accordingly, the motion of the fluid particles in the fluid field can be described as velocity potential, and the continuity equation is satisfied. Therefore, the governing equation of the fluid field is Laplace's equation:

$$\nabla^2\phi = 0 \tag{1}$$

where ϕ represents the velocity potential. The above governing equation can be converted into a boundary integral equation using Green's second identity according to the boundary element method, as follows:

$$\alpha\phi_i = \iint_{\Omega}\left(G_{ij}\frac{\partial\phi_j}{\partial n} - \phi_j\frac{\partial G_{ij}}{\partial n}\right)ds \tag{2}$$

where α represents the solid angle, which has a value of 0.5 when the field point is located on the boundary. The two-dimensional Green's function is $G_{ij} = -(1/2\pi)\ln R_1$, where R_1 represents the distance between the source point and field point distributed on the boundary of the computational domain.

There were boundary conditions for each boundary of the numerical towing tank, and linear boundary conditions were used in this study. Eqs. (3) and (4) give the linear boundary conditions of the free surface, i.e., the dynamic and kinematic boundary conditions, respectively.

$$\frac{\partial\phi}{\partial t} + g\eta = 0 \quad \text{on} \quad z = 0 \tag{3}$$

$$\frac{\partial\eta}{\partial t} = \frac{\partial\phi}{\partial z} \quad \text{on} \quad z = 0 \tag{4}$$

Here, η represents the vertical displacement of the free surface and g represents the gravitational acceleration. No penetration boundary condition was applied to the walls on both sides of the tank or the bottom, as given by Eq. (5).

$$\frac{\partial\phi}{\partial n} = 0 \tag{5}$$

The boundary condition for the moving cylindrical submerged body is given by Eq. (6), where U represents the velocity of the body and n_x is the horizontal-direction (x-direction) component of the normal vector on the submerged-body surface. The submerged body slowly accelerates and reaches a certain velocity, in the same manner as the experimental conditions. At this instance, the acceleration is given by the ramp function as shown in Eq. (7). The ramp function is applied to the initial acceleration section and the last deceleration section immediately before the submerged body stops. The ramp section is expressed by RT in Eq. (7), and it was set as 0.22 s, which was identical to that in the experiment. Fig. 6 shows the ramp function with respect to time. After passing through the ramp section, the submerged body performs translational motion at a constant towing velocity (U) in the constant-velocity region.

$$\frac{\partial\phi}{\partial n} = ramp \cdot (U \cdot n_x) \ \ on\ body \tag{6}$$

$$ramp = \begin{cases} \dfrac{1-\cos\left(\dfrac{\pi t}{RT}\right)}{2}, & t \le RT \\ 1, & t > RT \end{cases} \tag{7}$$

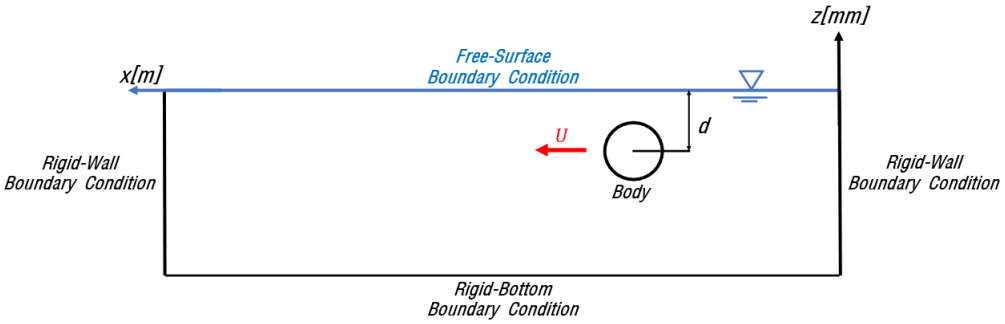

Fig. 5 Computational domain of the two-dimensional numerical towing tank

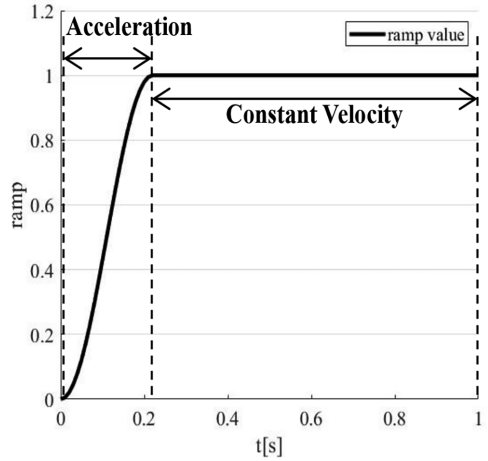

Fig. 6 Ramp function for towing velocity

3. Comparison and Analysis of Experimental Results

3.1 Analysis of Experimental Results

In the experiment of this study, the vertical displacement of free surface waves was analyzed, and its characteristics were identified according to the velocity and submerged depth of the submerged body. Table 2 presents the various submerged depth, velocity, and Froude number conditions examined. The waves generated in front of the submerged body by its motion were measured to identify their propagation characteristics, and the maximum wave height that occurred behind the body was measured and analyzed. Fig. 7 presents the vertical displacement of the free surface according to the body velocity in time series for submerged-body depths of $d = 1D$ and $d = 1.75D$. As shown, the displacement increased as the body velocity increased, and the maximum wave height occurred behind the body.

The number of free surface waves that propagated to the front of the submerged body increased as the body approached the measuring point (the position of the wave gauge) at a low velocity. However, when the submerged-body depth was large ($d = 1.75D$), the maximum wave height and the number of free surface waves that propagated to the front of the body decreased. In addition, when the submerged-body depth was small ($d = 1.0D$), the maximum free surface displacement occurred after the submerged body passed the wave gauge owing to the occurrence of the maximum wave depression with the rapid free surface increase, and the shape of the wave was mostly lost behind the body. In contrast, when the submerged-body depth was large, the overall free surface displacement decreased, as only the maximum wave depression occurred, without a rapid increase in surface displacement. This appears to be because the jet-like flow increased behind the submerged body, which led to an increase in the displacement of the free surface as the body velocity increased (increase in Froude number) or the submerged depth decreased at a constant velocity, as reported by Shin and Cho (2021). Therefore, it can be said that the jet flow, which depends on the submerged depth and velocity of the submerged body, affects the maximum wave height.

The cause of the loss of free surface waves behind the submerged body can be inferred from the work of Hyun and Shin (2000). It is judged that as the submerged-body depth decreases, the displacement of the free surface rapidly decreases owing to wave breaking that occurs behind the body. Conversely, if the submerged-body depth increases ($d = 1.75D$), the degree of wave breaking that occurs behind the body is weak owing to the sufficient distance between the body and free surface, and there is room for an increase in the displacement of the free surface.

Table 2 Experimental conditions

Parameter	Dimensions
Submerged-body depth (d)	$1D$, $1.5D$, $1.75D$ (m)
Body velocity (U)	0.3–0.7 (m/s)
Froude number ($F_r = \frac{U}{\sqrt{gD}}$)	0.330–0.771
Reynolds number ($Re = \frac{\rho UD}{\mu}$)	14,157–33,033
Towing distance (L_r)	4 (m)

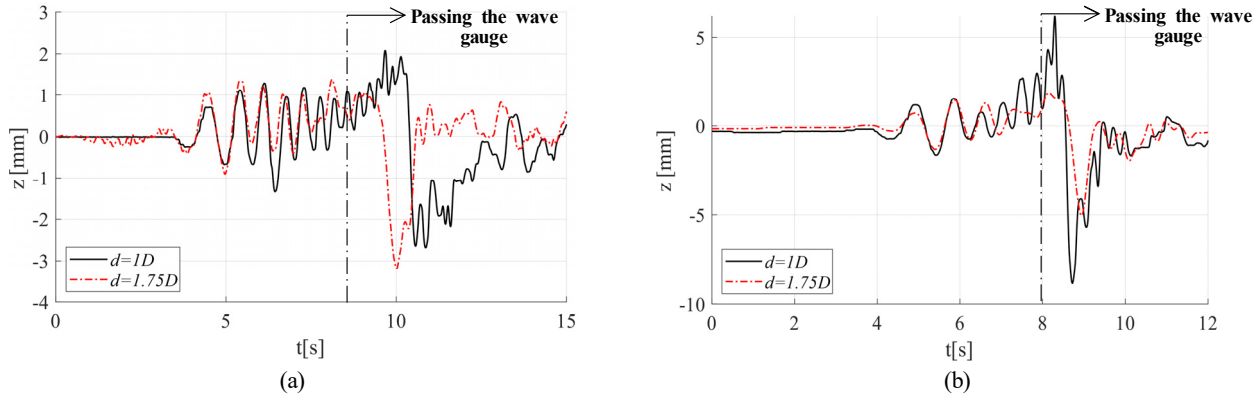

Fig. 7 Time series of surface elevations for different velocities: (a) U = 0.3 m/s; (b) U = 0.4 m/s; (c) U = 0.5 m/s; (d) U = 0.6 m/s; (e) U = 0.7 m/s

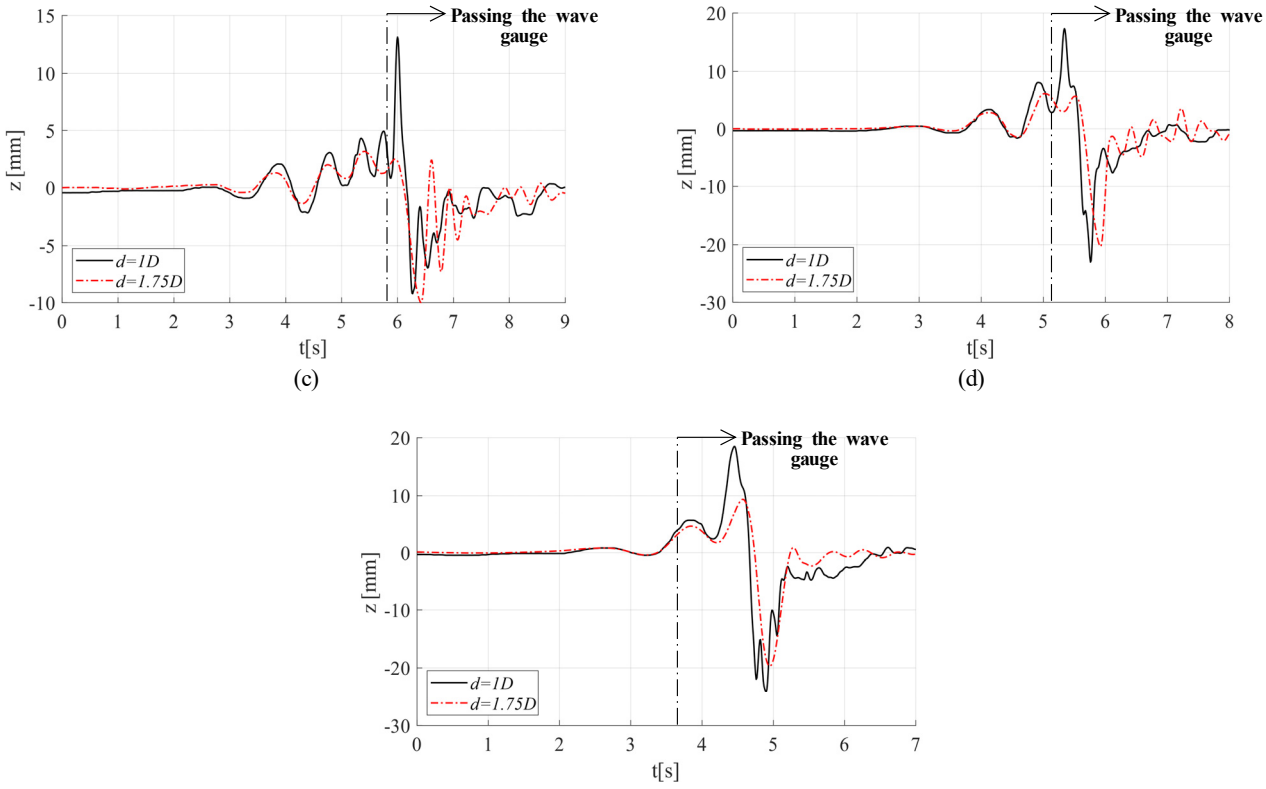

Fig. 7 Time series of surface elevations for different velocities: (a) U = 0.3 m/s; (b) U = 0.4 m/s; (c) U = 0.5 m/s; (d) U = 0.6 m/s; (e) U = 0.7 m/s (Continuation)

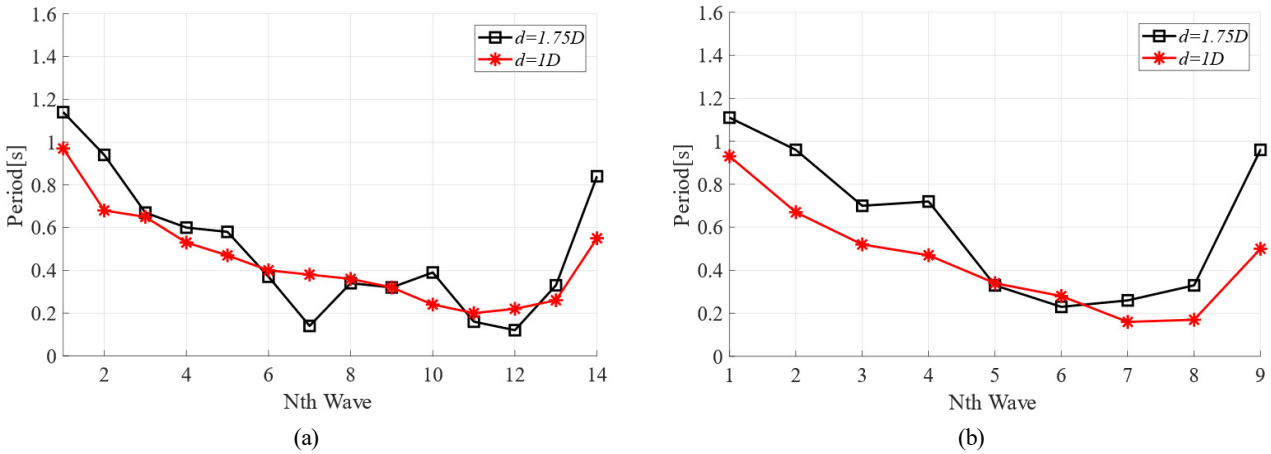

Fig. 8 Comparison of wave periods measured in order: (a) U = 0.3 m/s; (b) U = 0.4 m/s

Fig. 8 shows the results of measuring and comparing the wave periods observed in front of the submerged body in order. Here, Nth Wave = 1 represents the first period measured by the wave gauge as the wave generated at the time of the acceleration of the submerged body propagated forward. As indicated by Fig. 7, the number of waves measured in front of the submerged body increased as the submerged-body depth decreased. Therefore, the number of waves measured was small when the submerged depth was large (d = 1.75D). Long-period waves were generated at the beginning when the submerged body accelerated, and then the period of the waves decreased slightly. As the submerged body approached the measuring point (the position of the wave gauge), the measured wave period decreased, but the rate of reduction gradually decreased and tended to converge to a certain value. This is because various waves were generated at different velocities until the submerged body reached a certain velocity after acceleration, and fast long-period waves among them reached the measuring point first, followed by short-period waves. The value to which the wave period converged was similar to that given by a dispersion relation (Eq. 8) that corresponds to deep water conditions. In the comparison graph, the part where the period decreases and increases suddenly represents the wave period corresponding to the maximum wave height caused by the

submerged-body motion. The wave period was longer when the submerged-body depth was larger; i.e., long-period waves were generated at the maximum surface displacement that occurred behind the submerged body. In addition, the period measured in front of the submerged body was generally longer when the submerged-body depth was larger.

$$w^2 = gk \tag{8}$$

$$T = \frac{2\pi U}{g} \tag{9}$$

Here, T represents the wave period, w represents the wave frequency, and k represents the wavenumber.

Fig. 9 shows the maximum wave height according to the submerged depth and velocity of the submerged body. As in the previous analysis, the maximum wave height tended to increase as the body velocity increased. At 0.3 m/s, which was the lowest body velocity, there was no significant difference in wave height with respect to the submerged depth. However, as the velocity increased, the wave height rapidly increased at $d = 1.0D$, which was the smallest submerged depth, and then decreased at a maximum velocity of 0.7 m/s. This indicates that the wave height increases with the body velocity when the submerged depth is deep enough, but the maximum wave height decreases when the velocity increases further and wave breaking occurs behind the body. If the submerged-body depth is sufficiently large, the wave-height increase is small when the velocity is low; however, the wave height is likely to increase if the velocity increases. Under the experimental conditions of this study, even if the body velocity is higher than 0.7 m/s at a submerged depth of $d = 1.75D$, the maximum wave height will increase further because the effect of wave breaking that occurs behind the cylinder is expected to be insignificant. This phenomenon can be more accurately understood by comparing the wave steepness at the maximum wave height, as shown in Fig. 10. Wave steepness is expressed by an equation in which the wave height is divided by the wavelength ($\frac{H}{2\triangle x}$, $\triangle x = U\triangle t$). Theoretically, when

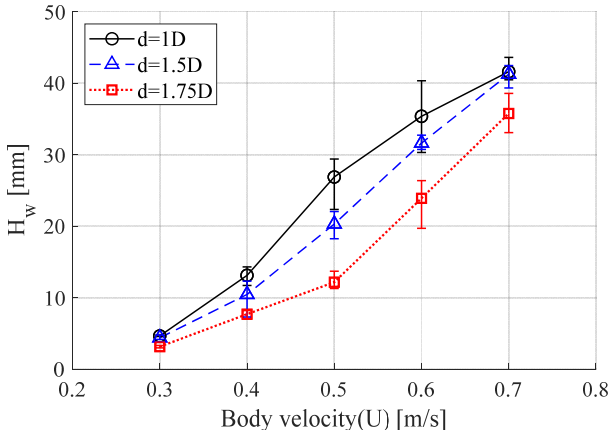

Fig. 9 Comparison of the maximum wave height for various body velocities

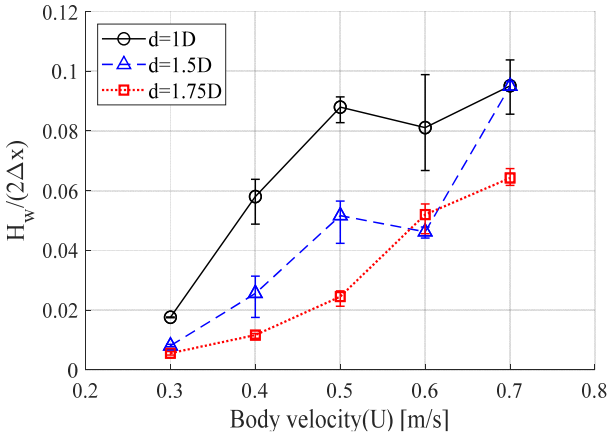

Fig. 10 Comparison of the wave steepness for various body velocities at the maximum wave height

the wave steepness is close to 0.1, wave breaking occurs. When the body velocity was 0.7 m/s, the wave steepness was close to 0.1 at submerged depths of $d = 1.0D$ and $d = 1.5D$. Under these conditions, the magnitude of the wave height no longer increases, because wave breaking occurs in free surface waves.

3.2 Comparison with Numerical Analysis Results

The results of the submerged-body towing experiment performed in the two-dimensional towing tank were compared with the calculation results obtained using the numerical towing tank. The benefit of the numerical technique is that the entire experimental tank can be modeled to perform calculations under the same conditions as the experiment by controlling the body velocity and reflected wave. Fig. 11 presents a comparison of the free surface displacement generated when the submerged body moved at the highest velocity ($U = 0.7$ m/s). As shown, the numerical analysis results generally agreed with the experimental results for the maximum wave depression of the free surface caused by the submerged-body motion. However, there was a significant difference in the free surface displacement generated behind the cylinder. This is because wave breaking occurred behind the body, and the shape of the wave was lost, as the wave steepness of the maximum wave height corresponded to the wave-breaking condition, as mentioned in the analysis of the experimental results. In contrast, in the potential flow-based numerical analysis, the waves generated by the submerged body-motion were maintained without breaking, because fluid viscosity and wave breaking were not considered. The maximum wave depression that occurs immediately after the passing of the submerged body and before the occurrence of wave breaking is the free surface displacement generated by the fluid pressure change caused by the cylinder motion. For the potential flow-based calculation, the fluid pressure change can be implemented, but it is difficult to implement the complex physical phenomena caused by fluid viscosity and wave breaking behind the submerged body. In addition, the free surface displacement that occurred in front of the submerged body was smaller than that in the experiment. This appeared to be because linear free surface boundary conditions were

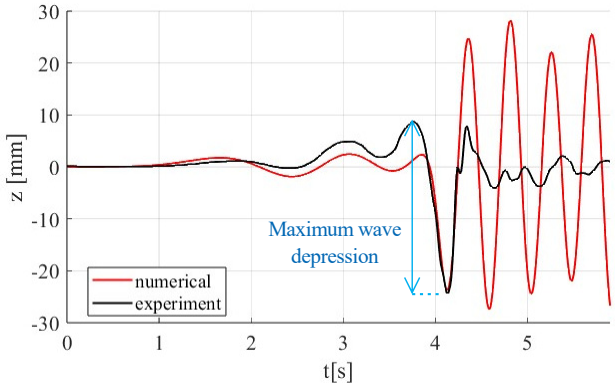

Fig. 11 Comparison of wave elevations for d = 1.75 D and U = 0.7 m/s

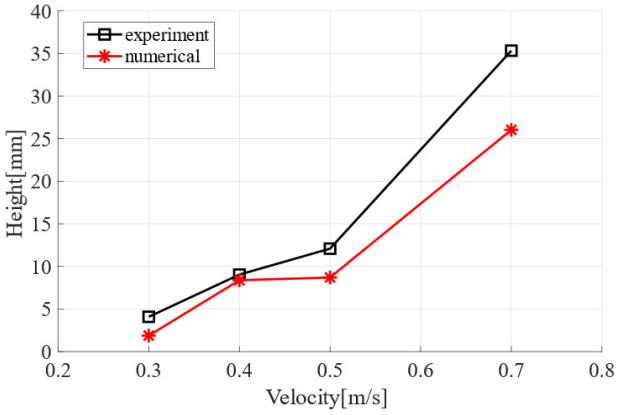

Fig. 12 Comparison of the maximum wave depression values for various body velocities

applied in the potential flow-based calculation; thus, the nonlinear geometry of the free surface was not reflected.

Fig. 12 presents a comparison of the magnitudes of the maximum wave depression of the free surface with respect to the velocity of the submerged body. The magnitude of the maximum wave depression corresponds to the length of the arrow in Fig. 11. The results of the experiment and numerical analysis were generally similar, and the magnitude of the maximum wave depression increased as the body velocity increased. This indicates that the formation of the maximum wave depression is affected more significantly by the kinematic factors of the submerged body and the resulting fluid pressure change than by the fluid viscosity. Therefore, the maximum wave height was accurately predicted in the potential flow-based numerical analysis, although the maximum wave height measured in the experiment slightly exceeded the numerical analysis result. This appears to be

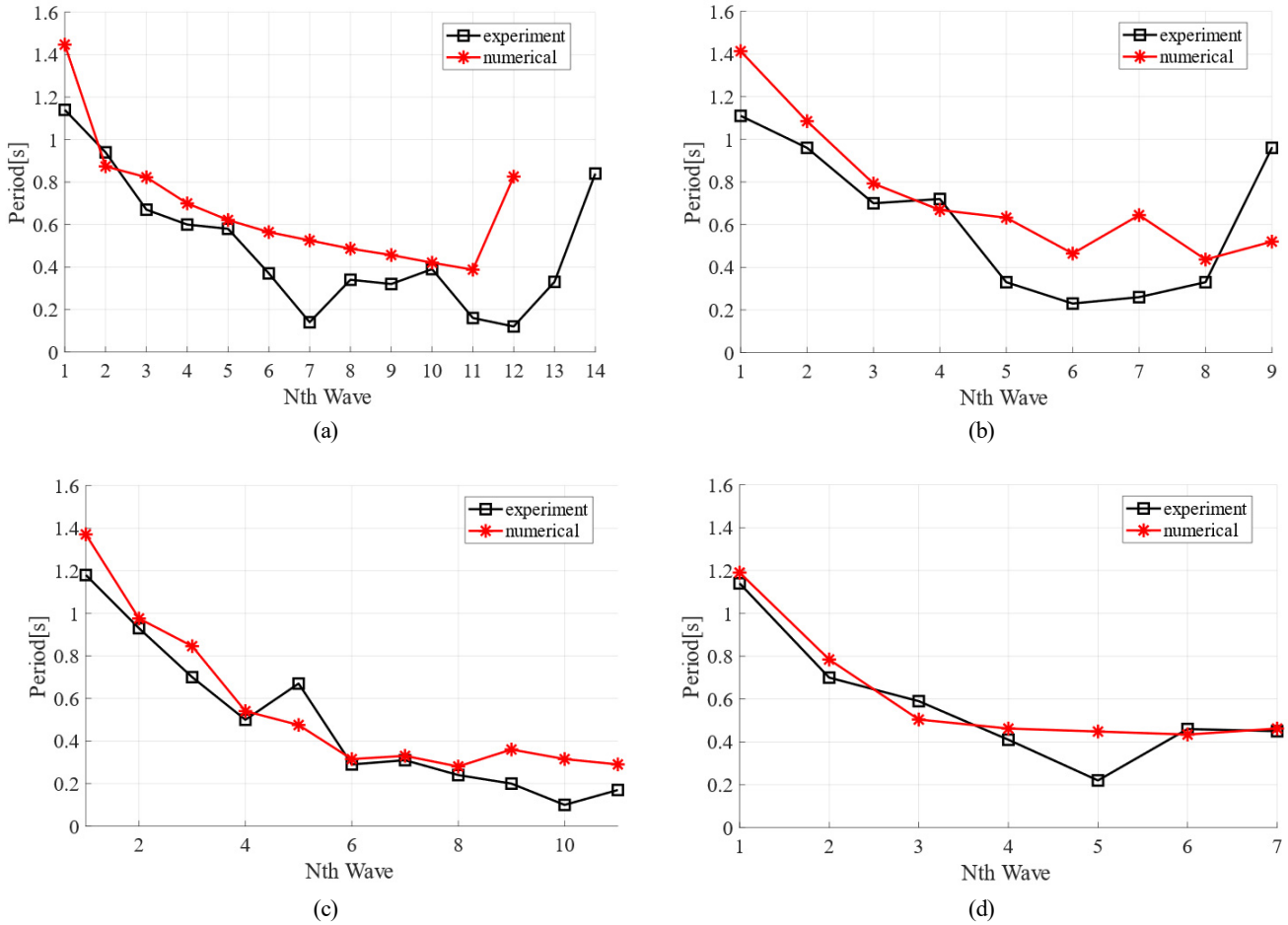

Fig. 13 Comparison of wave periods measured and calculated in order at d = 1.75D: (a) U = 0.3 m/s; (b) U = 0.4 m/s; (c) U = 0.5 m/s; (d) U = 0.7 m/s

because some of the effects of fluid viscosity that could not be considered in the potential flow-based calculations were included, and the nonlinear waveforms could not be properly implemented by applying linear free surface boundary conditions.

Fig. 12 presents a comparison of the measured and calculated periods of the free surface waves that propagated in front of the submerged body due to the body motion. As shown, the experimental and numerical analysis results had similar tendencies at all the body velocities. As the submerged body began translational motion and accelerated, waves with the longest period were generated and propagated first, followed by waves with gradually decreasing periods. The period of the waves generated by the submerged body at a constant velocity ultimately converged to the value given by Eq. (9), and it was confirmed that the convergence of the measurement and calculation results improved as the body velocity increased. Under all the velocity conditions, long-period waves were generated when the maximum wave depression occurred. Additionally, the rate of the wave-period increase decreased as the body velocity increased. This indicated that less long-period waves were generated as the body velocity increased, because the body quickly exited the acceleration region and entered the constant-velocity region owing to the submerged-body acceleration time being fixed at 0.22 s. Therefore, the agreement between the numerical analysis results and experimental results improved. However, the wave-period increase point differed between the experimental and numerical results, as shown in Fig. 13(a), because the numerical results and the measured data were different (Fig. 7(a)).

4. Conclusions

The complex flow phenomena around a submerged body moving under a free surface were measured using a two-dimensional submerged-body towing tank. Acceleration and constant-velocity regions were created by directly towing the cylindrical submerged body underwater. The displacement and propagation of the generated free surface waves were analyzed, and their characteristics were identified. The experimental results were compared with potential flow-based numerical analysis results to examine the effect of the fluid viscosity on the generation of free surface waves. The following conclusions are drawn.

(1) As the velocity of the submerged body increased and its submerged depth decreased, the maximum wave height of the free surface increased. However, the maximum wave height stopped increasing when the wave steepness reached the wave-breaking condition.

(2) When wave breaking occurred owing to the increase in body velocity, rapid wave loss occurred behind the body.

(3) Long-period waves were generated in the forward direction as the submerged body moved, and short-period waves were gradually generated as it moved at a constant velocity. This is because various waves were generated at different velocities until the submerged body reached a certain velocity after acceleration, and the fastest long-period waves among them reached the measuring point first, followed by short-period waves.

(4) In the potential flow-based numerical analysis results, the maximum wave depression was generally accurately predicted because it was possible to implement the fluid pressure change caused by the submerged-body motion, but it was difficult to implement the complex physical phenomena caused by fluid viscosity and wave breaking behind the submerged body.

To more precisely analyze the generation and propagation characteristics of free surface waves caused by submerged-body motion, it is necessary to investigate the changes in free surface waves due to changes in the submerged-body geometry and acceleration region, as well as high-speed motion, in the future. This will make it possible to obtain basic data that can be applied to the detection of submerged bodies that move near free surfaces.

Conflict of Interest

Weoncheol Koo serves as a editorial board member of the Journal of Ocean Engineering and Technology, but he had no role in the decision to publish this article. No potential conflict of interest relevant to this article was reported.

Funding

This research was supported by the Basic Research Project of Science and Engineering, National Research Foundation of Korea (NRF-2018R1D1A1B07040677).

References

Dean, W.R. (1948). On the reflection of surface waves by a submerged circular cylinder. *Mathematical Proceedings of the Cambridge Philosophical Society*, *44*(4), 483−491. https://doi.org/10.1017/S0305004100024506

Holloway, D. S., & Davis, M. R. (2002). Green function solutions for the transient motion of water sections. *Journal of Ship Research*, *46*(2), 99−120. https://doi.org/10.5957/jsr.2002.46.2.99

Hyun, B. S., & Shin, Y. H. (2000). On the viscous flow around breaking waves generated by a submerged cylinder (Part 2: Aspects of viscous flow). *Journal of the Society of Naval Architects of Korea*, *37*(1), 91−98.

Jeon, M. J., Mai, T. L., Yoon, H. K., Ryu, J. W., Lee, W. H., & Ku, P. M. (2021). Evaluation of dynamic characteristics for a submerged body with large angle of attack motion via CFD analysis. *Journal of Ocean Engineering and Technology*, *35*(5), 313−326. https://doi.org/10.26748/KSOE.2021.063

Journee, J. M. J., & Massie, W. W. (2001). Offshore hydromechanics (1st ed). *Delft University of Technology*.

Kim, D. E., Min, E. H., Koo, W. C., & Kim, Y. G. (2019). Numerical analysis of free surface by motion of a submerged body in fluids.

Proceedings of KOASTS 2019, 90−93.

Kim, J. B., Koo, W. C., & Min, E. H. (2022a). An experimental study of towing a circular submerged body in a single-layer fluid. *Proceedings of KOASTS 2022*, 264−265.

Kim, J. B., Koo, W. C., & Min, E. H. (2022b). Comparison of numerical simulation and experiment of a towed submerged cylinder in a single fluid. *Proceeding of the Annual Autumn Conference 2022*, SNAK, 418−422.

Liu, T. L., & Guo, Z. M. (2013). Analysis of wave spectrum for submerged bodies moving near the free surface. *Ocean Engineering*, *58*, 239−251. https://doi.org/10.1016/j.oceaneng.2012.10.003

Min, E. H., & Koo, W. C. (2017). Hydrodynamic characteristics of internal waves induced by a heaving body in a two-layer fluid. *Ocean Engineering*, *145*(15), 290−303. https://doi.org/10.1016/j.oceaneng.2017.09.017

Min, E. H., & Koo, W. C. (2022). Comparison of wave diffraction forces on a surface-piercing body for various free-surface grid update schemes. *Ocean Engineering*, *259*(1), 111912. https://doi.org/10.1016/j.oceaneng.2022.111912

Mnasri, C., Hafsia, Z., Omri, M., & Maalel, K. (2014). A moving grid model for Simulation of free surface behavior induced by horizontal cylinders exit and entry. *Engineering Applications of Computational Fluid Mechanics*, *4*(2), 260−275. https://doi.org/10.1080/19942060.2010.11015315

Ren, Y., Qin, Y., Pang, F., Wang, H., Su, Y., & Li, H. (2023). Investigation on the flow-induced structure noise of a submerged cone-cylinder-hemisphere combined shell. *Ocean Engineering*, *270*, 113657. https://doi.org/10.1016/j.oceaneng.2023.113657

Scullen, D., & Tuck, E. O. (1995). Nonlinear free-surface flow computations for submerged cylinders. *Journal of Ship Research*, *39*(3), 185−193. http://pascal-francis.inist.fr/vibad/index.php?action=getRecordDetail&idt=3668054

Seong, W. J., Koo, W. C., & Min, E. H. (2022). Numerical and experimental study on free-surface wave generation by a submerged moving body in a towing tank. *Ocean Engineering*, *252*(15), 1−12. https://doi.org/10.1016/j.oceaneng.2022.111200

Sheridan, J., Lin, J. C., & Rockwell, D. (1997). Flow past a cylinder close to a free surface. *Journal of Fluid Mechanics*, *330*(10), 1−30. https://doi.org/10.1017/S002211209600328X

Shin, D. M., & Cho, Y. (2021). Concurrent vortex-shedding and surface-wave phenomena around a horizontal circular cylinder close to a free surface. *Proceeding of KSME Conference*, 33−35.

Ursell, F. (1950). Surface waves on deep water in the presence of a submerged circular cylinder. I. *Mathematical Proceedings of the Cambridge Philosophical Society*, *46*(1), 141−152. https://doi.org/10.1017/S0305004100025561.

Uzair, A. S., & Koo, W. C. (2012). Hydrodynamics analysis of a floating body with an open chamber using a 2D fully nonlinear numerical wave tank. *International Journal of Naval Architecture and Ocean Engineering*, *4*(3), 281−290. https://doi.org/10.2478/IJNAOE-2013-0096.

Yi, H. J., Shin, H. K., & Yoon, B. S. (2013). Study on flow around circular cylinder advancing beneath free surface. *Journal of Ocean Engineering and Technology*, *27*(5), 16−21. http://dx.doi.org/10.5574/KSOE.2013.27.5.016.

Author ORCIDs

Author name	ORCID
Kim, Jun-Beom	0009-0005-9604-8598
Min, Eun-Hong	0000-0003-1045-9475
Koo, Weoncheol	0000-0002-4384-0996

KSOE

Journal of Ocean Engineering and Technology 37(3), 99-110, June, 2023
https://doi.org/10.26748/KSOE.2023.002

pISSN 1225-0767
eISSN 2287-6715

Original Research Article

Fire Resistance Characteristics of Firewall Structure Associated with Impact Damage Induced by Explosion

Hye Rim Cho[1], Jeong Hwa Yoo[2] and Jung Kwan Seo[3]

[1]*Ph.D. Course Student, Department of Naval Architecture and Ocean Engineering, Pusan National University, Busan, Korea*
[2]*Master Course Student, Department of Naval Architecture and Ocean Engineering, Pusan National University, Busan, Korea*
[3]*Professor, Department of Naval Architecture and Ocean Engineering and The Korea Ship and Offshore Research Institute, Pusan National University, Busan, Korea*

KEYWORDS: Fire resistance, Firewall structure, Explosion damage, Fragment, Thermal-structural interactions

ABSTRACT: *When a fire accident accompanied by an explosion occurs, the surrounding firewalls are affected by impact and thermal loads. Damaged firewalls due to accidental loads may not fully perform their essential function. Therefore, this paper proposes an advanced methodology for evaluating the fire resistance performance of firewalls damaged by explosions. The fragments were assumed to be scattered, and fire occurred as a vehicle exploded in a large compartment of a roll-on/roll-off (RO-RO) vessel. The impact velocity of the fragments was calculated based on the TNT equivalent mass corresponding to the explosion pressure. Damage and thermal-structural response analyses of the firewall were performed using Ansys LS-DYNA code. The fire resistance reduction was analyzed in terms of the temperature difference between fire-exposed and unexposed surfaces, temperature increase rate, and reference temperature arrival time. The degree of damage and the fire resistance performance of the firewalls varied significantly depending on impact loads. When naval ships and RO-RO vessels that carry various explosive substances are designed, it is reasonable to predict that the fire resistance performance will be degraded according to the explosion characteristics of the cargo.*

1. Introduction

Fire and explosion are high-risk accidents that can cause financial and environmental damage by causing severe damage to surrounding structures and casualties. Fig.1 summarizes fire/explosion accidents and casualties/injuries on ships based on statistics published by the Transportation Safety Board of Canada (2021). Of 2,599 ship accidents over the past 11 years, 15.47 percent were fire/explosion accidents, with an average of 37 fires/explosions occurring annually. Fire/explosion accidents occur continuously, and complete control is impossible, despite various studies to protect casualties, property, and the environment. Therefore, a damage reduction method based on risk is required and applied to protect the hull from fire accidents. Passive fire protection (PFP), such as fire alarms, sprinkling equipment, and firewalls, has been used to reduce damage from fire accidents. The firewall, one of the representative PFPs, delays and prevents the spread of fire. The characteristics of fires, such as liquid, gas, and electrical fires, that are expected to occur in certain places should be considered when installing firewalls. They should also be designed to maintain fire resistance for a time required by the standard fire curves.

Among the varying fire resistance evaluation methods for firewalls, the U.S. Navy stipulates the fire resistance evaluation method of

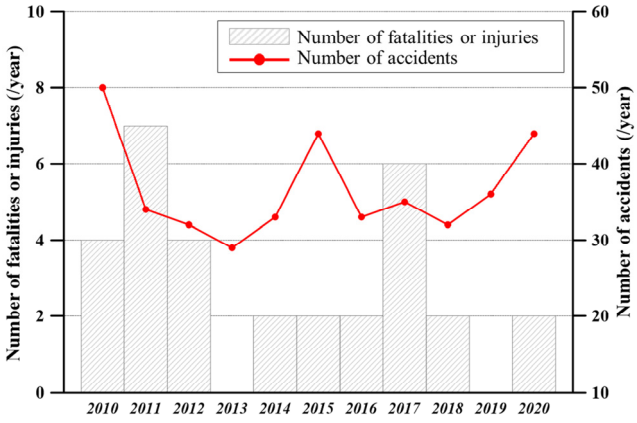

Fig. 1 Shipping fire/explosion accidents

Received 6 February 2023, revised 10 June 2023, accepted 22 June 2023
Corresponding author Jung Kwan Seo: +82-51-510-2415, seojk@pusan.ac.kr

firewalls installed on warships. According to this evaluation methods, a reference impact load acts on the firewall to cause damage. The thermal load is applied to the damaged firewall to evaluate the fire resistance performance (U.S. Department of Defense, 2007). The Safety of Life at Sea (SOLAS) (IMO, 2002) provides evaluation criteria and methods to ensure that intact firewalls meet the appropriate fire resistance during the reference time. Fire and explosion are highly relevant accidents. Hence, the explosive effect should be considered in the design of firewalls in the large compartment expected to the high-risk accident. Nevertheless, the existing SOLAS regulations provide criteria considering fire only.

Choung et al. (2011) analyzed the structural deformation characteristics of the firewall at high temperatures using a numerical analysis method. Kim et al. (2014) and Seo et al. (2017) conducted a thermal analysis of the firewall equipped with PFP under fire accidents. D'Amore et al. (2020) presented a finite element analysis method evaluating the fire resistance performance of fire doors according to the procedure supplied by IMO. Park et al. (2021) experimentally investigated the PFP material characteristics and analyzed the thermal characteristics of firewalls, including the PFP material. Park and Song (2019, 2021) evaluated the fire resistance design by conducting the fire test and heat transfer analysis on A-60 grade fire resistance equipment. Despite the attempts to evaluate the fire resistance performance of fireproof structures, studies on the safety evaluation of firewalls considering the effects of explosions are insufficient. Therefore, this study proposes a methodology to evaluate the fire resistance performance of firewalls considering the impact of explosions when designing firewalls installed in areas with a high explosion risk. The degree of damage and thermal response characteristics of the firewall panels were analyzed quantitatively using the proposed method.

2. Fire Resistance Analysis Procedure of Firewall Considering Explosive Effect

Explosions often lead to fires, depending on the characteristics of combustible materials. But existing firewall design and evaluation methods have limitations in securing sufficient safety against fire and impact damage induced by explosions. This study proposes an advanced methodology that evaluates the fire resistance performance after the impact of explosions acting on firewalls, as shown in Fig. 2.

The existing method is described as follows. After selecting a target firewall structure, the likelihood of a fire accident was evaluated qualitatively to discern the hazards. A fire accident scenario is derived based on the fire hazard identified in the “Fire hazard identification” stage, and thermal-structure response characteristics were analyzed by numerical analysis and experiment. The fire resistance of a firewall was evaluated by comparing the capacity design strength (C_d) of the structure determined through the previous process with the demand

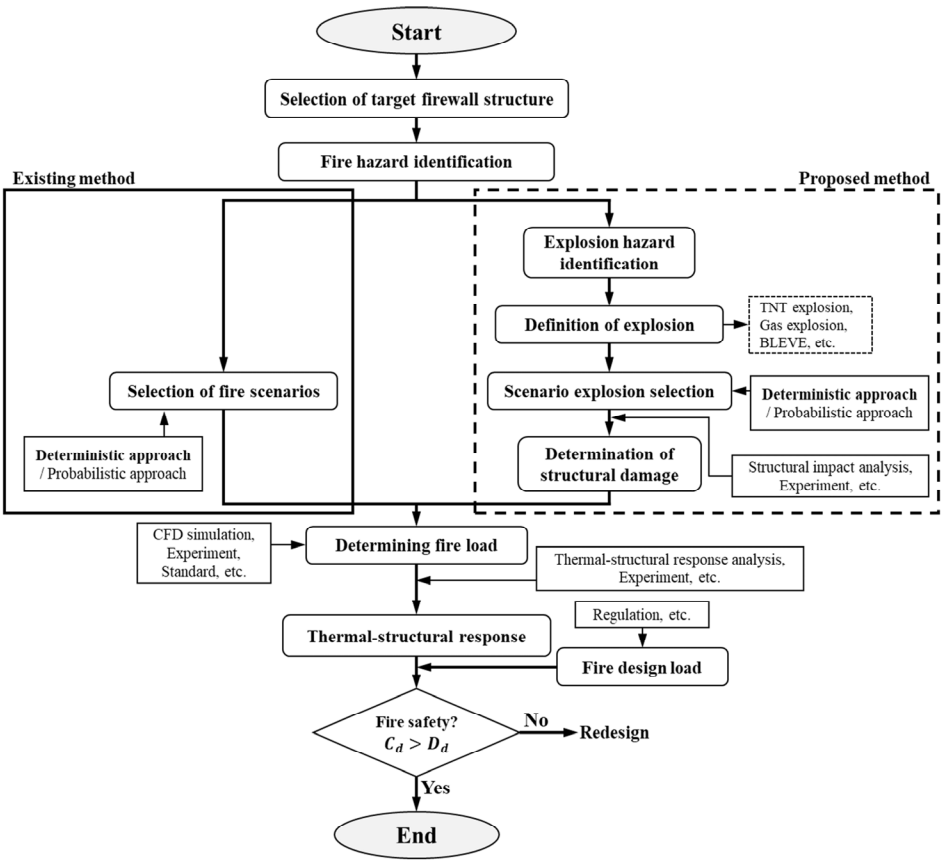

Fig. 2 Methodology of fire resistance characteristics analysis

design load (D_d). The proposed method also proceeds similarly to the existing method, as shown in Fig. 2. This study evaluated the fire resistance performance of firewalls considering the consequences of explosion by supplementing the existing method.

The "Explosion hazard identification" step identified the potential for an explosion by considering the fire resistance materials, explosion conditions, and consequences of an explosion. The "Definition of explosion" is the stage for selecting the form and influential factors of the explosion. The type of explosion among various explosions, such as boiling liquid expansion steam explosion (BLEVE), solid explosion, gas explosion, and dust explosion, and the influential factors of the explosion affecting the structure are defined. The explosion scenario is selected in the "Scenario explosion selection" stage using an existing deterministic or probabilistic approach based on the explosion characteristics defined in the previous stages. In the "Determination of the structural damage" stage, structural impact analysis and experimental methods are used to predict the degree of damage to the firewall. The degree of damage is applied to the firewall. The thermal-structural response characteristics are identified in the "Thermal-structural response" stage through numerical analysis and experimental methods using the damaged firewall defined in the previous stage as the target structure.

3. Example of Application

Recently, battery fires/explosions of electric vehicles are a major risk factor. Accordingly, the vehicle hangar area of the pure car carrier carrying electric vehicles was selected as the location of the accident. Therefore, this study assumed the fire and explosion scenarios that a secondary fire was caused by a hydrocarbon-based combustible substance after the fragment was scattered by the explosive pressure of a small vehicle (fuel tank and battery). The target firewall will be damaged by impact and thermal loads of fragments induced explosion and fire.

The scatter of fragments caused by explosions was assumed, and the shape and initial velocity of the fragments were considered the influential factor. The solid explosive pressure of a compact car is converted to the TNT (trinitrotoluene) mass using the TNT equivalent method. Fig. 3 shows a schematic diagram of the application of the proposed method. Structural damage and thermal-structural response characteristics of firewall structures were analyzed consecutively using commercial finite element analysis code (Livermore Software Technology Corporation, 2018) through impact analysis and thermal response analysis.

3.1 Target Structure

A typical firewall panel that can be installed in a large compartment of ship and connected by a channel was selected as the target structure, as shown in Fig. 4. The firewall panel is a structure with mineral wool, one of the PFP materials, built between frames made of steel. Fig. 4 presents the main dimensions of the target structure, and each element was modeled in a hexahedron sharing eight nodes. As shown in Fig. 5, convergence studies were conducted to select the optimal mesh size. Convergence was reviewed in terms of the maximum Von Mises stress and maximum equivalent strain for each of various element sizes (20 mm × 20 mm, 10 mm × 10 mm, 6 mm × 6 mm, 5 mm × 5 mm, and 3 mm × 3 mm), and it was selected as an element size of 5mm×5mm according to the result. The range expected to be affected by the impact load was applied fine element, and another range applied a coarse mesh; Table 1 provides information on model elements.

3.2 Scenarios Selection

The explosion fragments were selected in the shape of a sphere and a cube, and the degree of damage according to the velocity of various shapes was compared by assuming that the mass of each fragment was the same as 10 kg of steel. Considering the shape characteristics of the fragments, a total of three impact positions, including points, lines, and surfaces, were considered, as shown in Fig. 6.

The explosion pressure must be defined to calculate the initial scattering velocity of fragments. Consequently, the TNT equivalent mass method was used to estimate the explosion pressure according to the separation distance between the firewall panel (target structure) and the center of the explosion. According to Federal Emergency Management Agency (2006), the TNT equivalent mass of a small vehicle is 227 kg, and the maximum pressure by the distance between fragments from the explosion could be calculated using Eq. (1) (Newmark and Hansen, 1961).

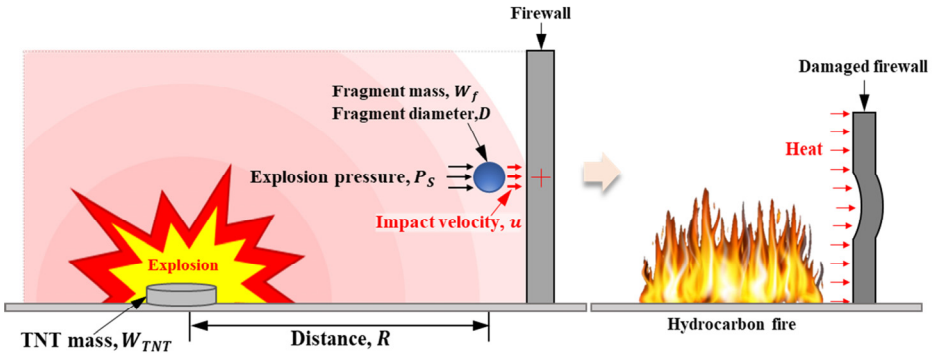

Fig. 3 Target location and fire resistance characteristics analysis scenario of the firewall

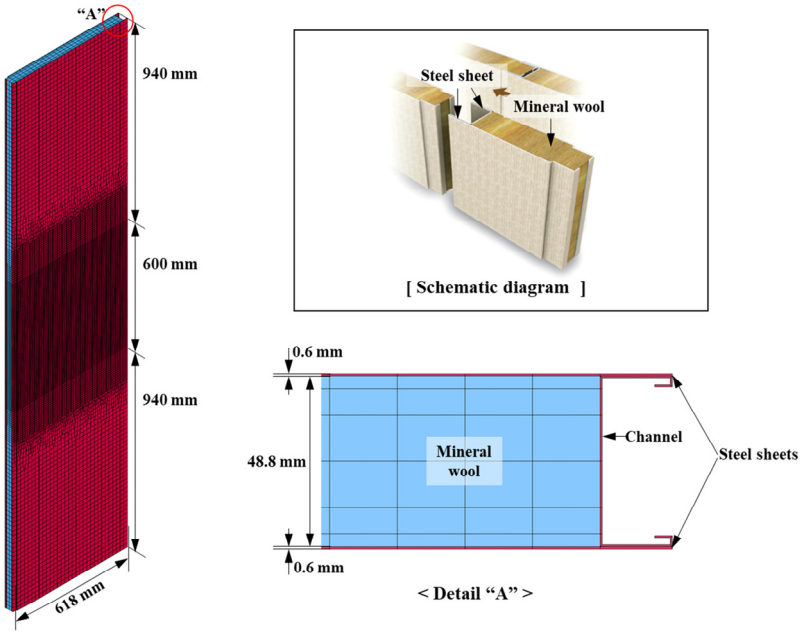

Fig. 4 Schematic diagram and FE (Finite element) model of the typical firewall panel

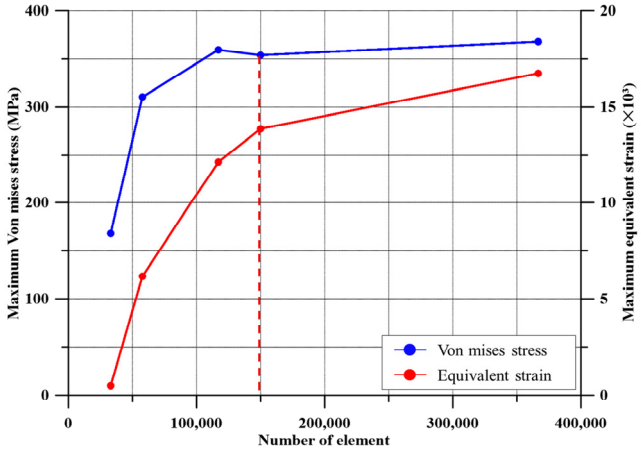

Fig. 5 Result of the convergence study to determine the optimal element size

Table 1 Description of elements in the FE model of the firewall

Feature	Steel sheets & channel		Mineral wool	
	Coarse mesh	Fine mesh	Coarse mesh	Fine mesh
Element type	Solid		Solid	
Element size	20 mm × 20 mm × 0.6 mm	5 mm × 5 mm × 0.6 mm	20 mm × 20 mm × (4–12) mm	5 mm × 5 mm × (4–7) mm
The number of elements	9,524	32,640	22,324	85,440
The number of all elements	149,928			

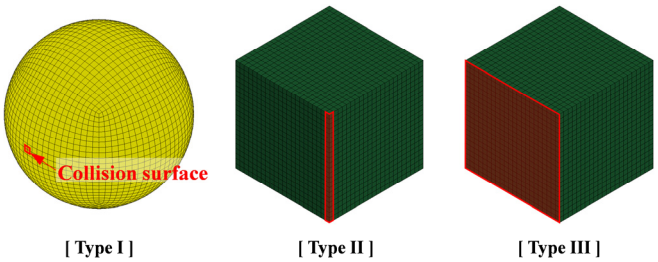

Fig. 6 Fragment FE model and initial contact surface in each case

$$P_S = 678.4\frac{W_{TNT}}{1000R^3} + 9.3\left(\frac{W_{TNT}}{1000R^3}\right)^{1/2} \quad (1)$$

where P_S is the maximum pressure; W_{TNT} is the TNT equivalent mass; R is the separation distance of the firewall from the explosion. The initial scattering velocity of the fragment could be calculated by substituting the maximum pressure for each distance defined by Eq. (1) into Eq. (2) (CCPS, 1999).

$$u = 2.05\sqrt{\frac{P_S D^3}{W_f}} \quad (2)$$

where u is the initial scattering velocity of the fragment; D is the diameter of the fragment area under explosive pressure; W_f is the mass of the fragment. The fragment area subjected to explosion pressure different according to the shape and initial collision surface of the fragment. Thus, the initial scattering velocity was different for each fragment shape. On the other hand, the initial scattering velocity of the "Type I" fragment model was applied equally to the entire scenario to compare the degree of damage and fire resistance by each fragment shape under the same velocity condition. The impact velocity at which the fragment collides with the firewall panel has been assumed to be the initial scattering velocity in this study.

Fig. 7 presents the initial scattering velocity, i.e., impact velocity, based on the separation distance between the center of the explosion and the firewall derived through the process. The maximum pressure and initial scattering velocity at 0.1 m were 154.14 GPa and 7666.75 m/s, respectively. Case analysis was performed repeatedly to estimate the appropriate impact velocity range. The fragment fully penetrated the firewall at the impact velocity condition of approximately 12 m/s. There was little difference in fire resistance performance depending on the degree of damage under an impact velocity condition of less than approximately 8 m/s. Therefore, the initial scattering velocity range was determined from 8 to 12 m/s. Nine scenarios were selected in terms of the shape, collision surface, and initial scattering velocity of the fragment, as shown in Table 2.

Table 2 Study scenarios with different impact conditions

Scenario no.	Initial velocity of fragment (m/s)	Fragment type
1		I
2	8	II
3		III
4		I
5	10	II
6		III
7		I
8	12	II
9		III

3.3 Impact Analysis by Explosive Fragment

3.3.1 Mechanical material property

Steel sheets and channels were modeled with mild steel material, and the material properties for each firewall model were obtained through the tensile test results (Paik et al., 2017; Park et al., 2021). Table 3 lists the material properties of mineral wool and mild steel, and Table 4 summarizes the thermal properties of mineral wool at varying temperatures. The fracture behavior of the structure was simulated by applying a dynamic fracture strain and eliminating the elements exceeding the set fracture strain. The dynamic fracture strain of steel materials by various impact velocities was calculated using Eq. (3) to define the dynamic fracture characteristics of the model (Paik et al., 2017; Cowper and Symonds, 1957). Table 5 lists the dynamic fracture strain of carbon steel computed by various impact velocities. The dynamic fracture strain of mineral wool was assumed to be 0.35, which was estimated through parametric studies based on the damaged volume due to a lack of data.

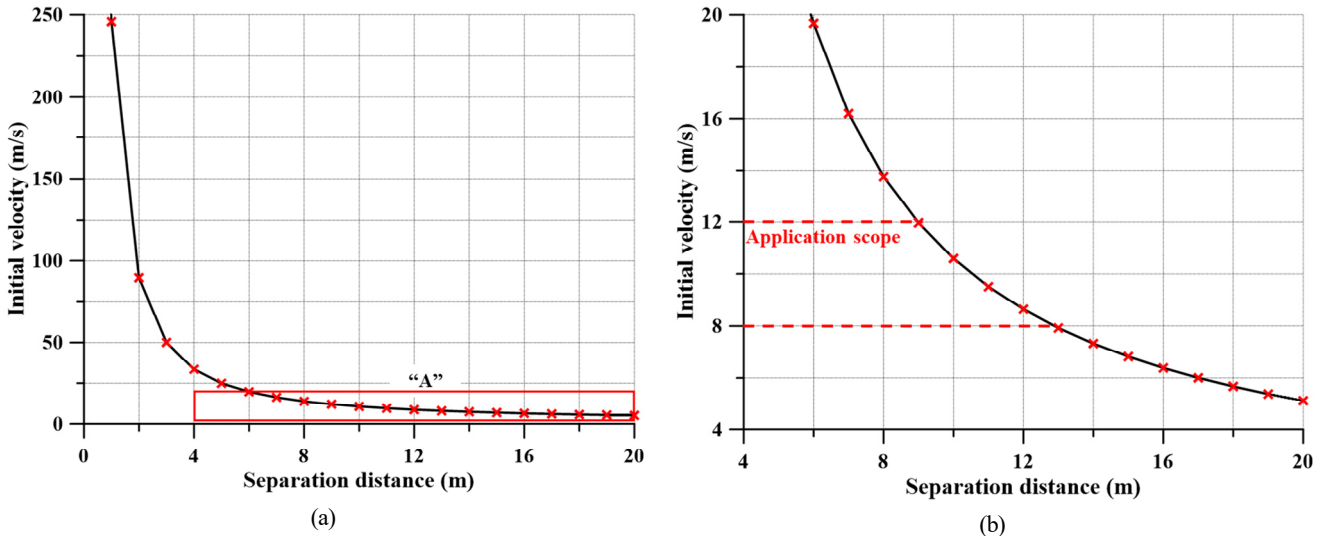

Fig. 7 Initial velocity of fragment by the separation distance: (a) Initial velocity; (b) Zoom in "A"

$$\epsilon_{fd} = \left[1 + \left(\frac{\dot{\epsilon}}{C}\right)^{\frac{1}{q}}\right]^{-1} \epsilon_{fc} \quad (3)$$

where ϵ_{fd}, $\dot{\epsilon}$, and ϵ_{fc}, represent dynamic fracture strain, strain rate, and critical fracture strain, respectively, and C and q are Cowper-Symonds coefficients.

Table 3 Mechanical material properties of the firewall panel (Paik et al., 2017; Park et al., 2021)

Type		Firewall	
		Mild steel	Mineral wool
Density (kg/m^3)		7,850	200
Young's modulus (MPa)		210,000	45.25
Poisson's ratio		0.3	0.26
Yield stress (MPa)		281.6	0.257
Static fracture strain		0.429	0.0297
Couper-Symons coefficients	C (s^{-1})	3,200	
	q	40	

Table 4 Thermal properties of mineral wool (Park et al., 2021)

Temperature (℃)	Young's modulus (kPa)	Yield stress (kPa)
Room temperature	45.25	256.59
100	43.10	287.56
200	43.17	431.33
300	22.21	300.93
400	9.46	44.28

Table 5 Dynamic fracture strain of mild steel used for the FEM analysis

Impact velocity (m/s)	Strain rate (s^{-1})	Dynamic fracture strain
8	23.074	0.087
10	29.014	0.085
12	34.954	0.078

3.3.2 Load condition

The upper and lower parts of firewall panel were assumed to be fixed to the wall, and the left and right parts are connected through channels. Hence, the upper and lower parts and the left and right ends were applied to the fixed and simple support conditions, respectively, as shown in Fig. 8(a). The impact point of the fragment was selected as the center of the firewall panel, which is expected to be the weakest.

3.3.3 Result

Fig. 9 shows the deformed shape of the firewall panel at maximum penetration of the various fragment shape. In the case of "Type I", the damaged reduction ratio was up to 94.46% at an impact velocity of 10 m/s. In contrast, the firewall panel was slightly damaged in the case of "Type III". This result suggests that most of the kinetic energy was used to cause the global deformation of the structure, as the collision (contact) surface of the "Type III" fragment is larger than that of the other cases.

3.4 Thermal-Structural Response Analysis

3.4.1 Thermal mechanical property of the material

The thermal properties of steel material were modeled by applying the reduction factor provided by Eurocode 3 (European Committee Standardization, 2005), as shown in Fig. 10. The material properties of mineral wool by various temperatures were applied to the data summarized in Table 4.

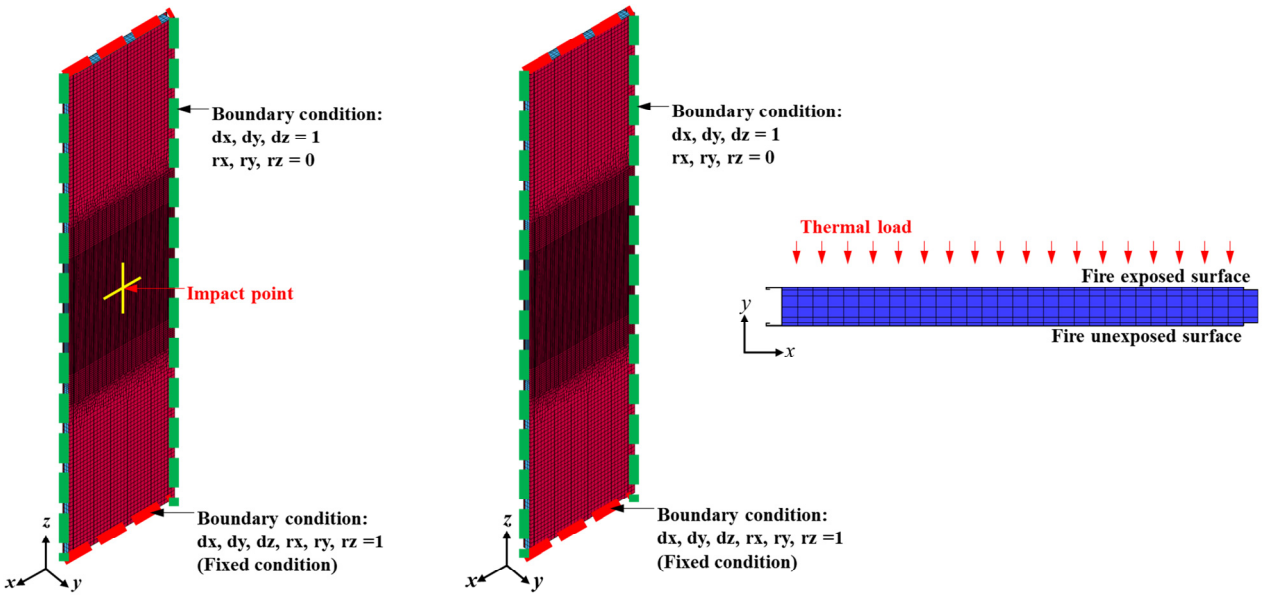

Fig. 8 Boundary conditions and loading direction applied: (a) Impact analysis; (b) Thermal-structural response analysis

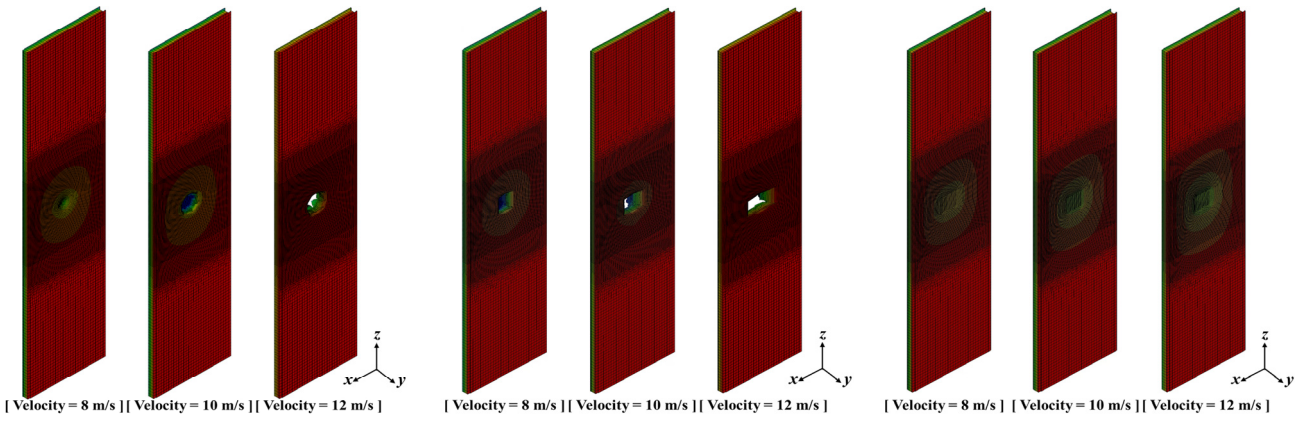

(a) (b) (c)

Fig. 9 Damaged firewall due to the impact of the fragment: (a) Fragment type I; (b) Fragment type II; (c) Fragment type III

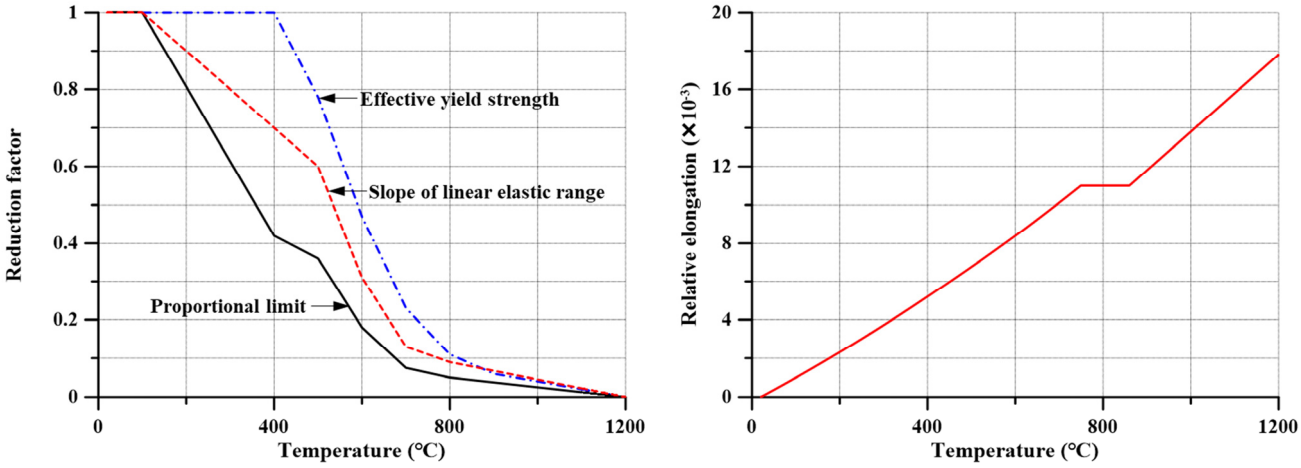

(a) (b)

Fig. 10 Mechanical properties of carbon steel varying with temperatures (European Committee Standardization, 2005): (a) Reduction factor; (b) Thermal elongation

3.4.2 Thermal property

The thermal behavior characteristics of steel materials were modeled, as shown in Fig. 11, by applying the data provided in Eurocode 3 (European Committee Standardization, 2005). The thermal behavior characteristics of mineral wool were obtained from the fire test results. The thermal conductivity and specific heat are 0.37 W/mK and 836.80 J/kgK, respectively (Park et al., 2021).

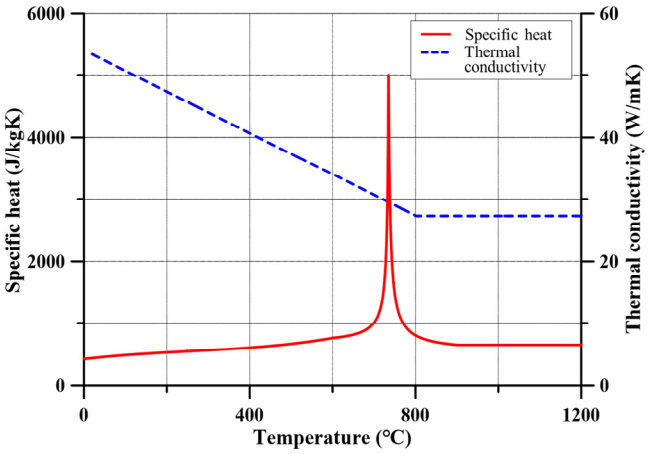

Fig. 11 Thermal properties with varying temperatures (European Committee Standardization, 2005)

3.4.3 Load condition

The same boundary conditions were assumed as the impact analysis, and the load condition was considered so that the thermal loading acted throughout the same surface as the impact point of the fragment, as shown in Fig. 8(b). The thermal loading represented by the hydrocarbon fire curve presented in Eurocode 1 (European Committee Standardization, 2002) acted on the firewall fire exposure surface for 3600 seconds, as shown in Fig. 12.

3.5 Result

3.5.1 Comparison by the degree of damage

The degree of damage was calculated by measuring the reduced volume in the central section of the firewall panel, and the fire resistance performance was analyzed by comparing the temperature between the fire-exposed and unexposed surfaces of the firewall panel. Fig. 13 shows the temperature distribution after exposure to thermal

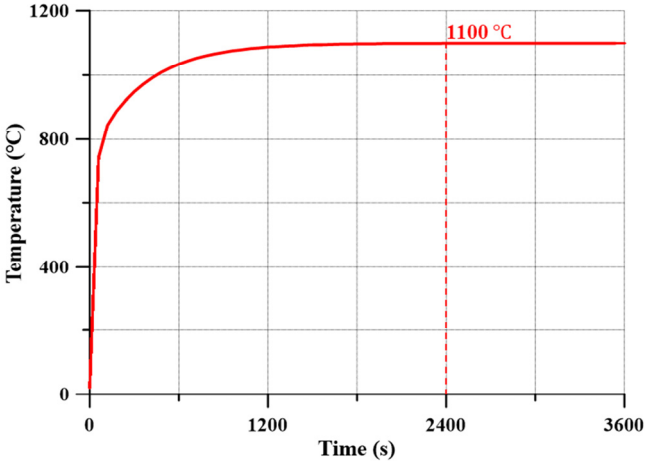

Fig. 12 Hydrocarbon fire curve (European Committee Standardization, 2002)

load for one hour, and Fig. 14 presents the maximum temperature at each location. The asymmetric deformation of firewalls was caused by the geometric difference between the left and right ends to which the boundary condition was applied, as shown in Fig. 13.

In the case of firewall panels damaged by "Type I" and "Type II" fragments at an impact velocity of 8 m/s, there was a temperature difference of 0.14–41.48% from the intact firewall, but there was little difference in the case of the "Type III" fragment. Global deformation occurred at the structure and there was little volume change because the collision surface of the "Type III" fragment is wide and flat, as described in the impact analysis results in Section 3.4.

The "Type III" fragment at an impact velocity of 10 m/s showed a temperature and damaged volume difference of 0.16–4.53% and 0.01% compared to the intact firewall panel, respectively, as shown in Fig. 14(b). In the case of the "Type I" fragment, the temperature was increased by 43.36%, while the volume decreased by 94.46 %.

In the case of "Type I" and "Type II" at an impact velocity of 12 m/s, Fig. 14(c) shows the temperature distribution for the remaining points, except for the "PT0" point, which was immeasurable because of the penetration of the fragment. The temperature of the "PT-1" and "PT1", which had the most differences in fire unexposed surface, was measured at 41.29%, 45.16% ("Type I"), 42.14%, and 46.81% ("Type II") higher than the intact firewall panel, respectively.

At the position indicated in Fig. 15, the temperature difference and temperature ratio of the non-exposed surface to the fire-exposed surface depending on the degree of the volume damage were compared (Fig. 16). The temperature difference and ratio decreased and increased linearly depending on the volume reduction ratio, respectively. Compared to the intact condition, the temperature difference between both surfaces of the firewall panel was decreased by a maximum of 99.97%, and the temperature ratio between both surfaces was increased by up to 57.15%. The temperature

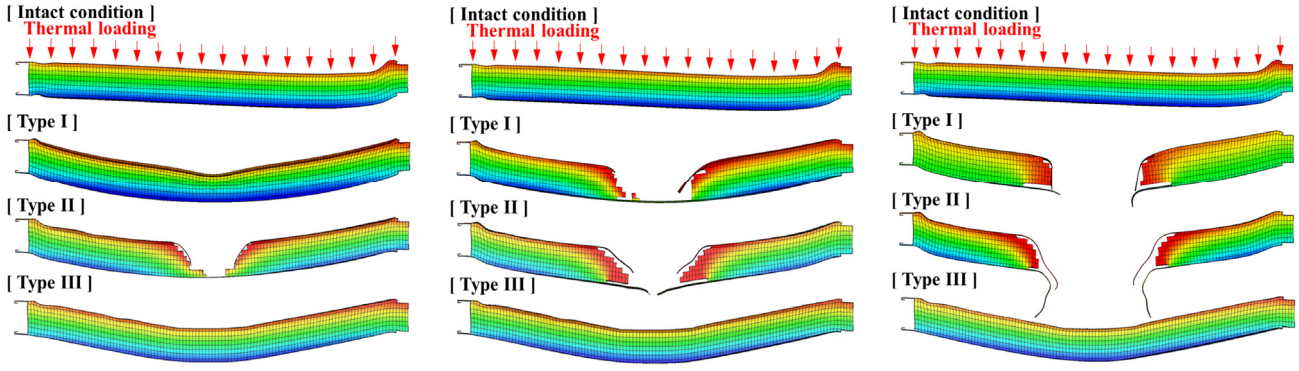

Fig. 13 Temperature contour of the firewall panel center under thermal load at various impact velocities: (a) 8 m/s, (b) 10 m/s, and (c) 12 m/s

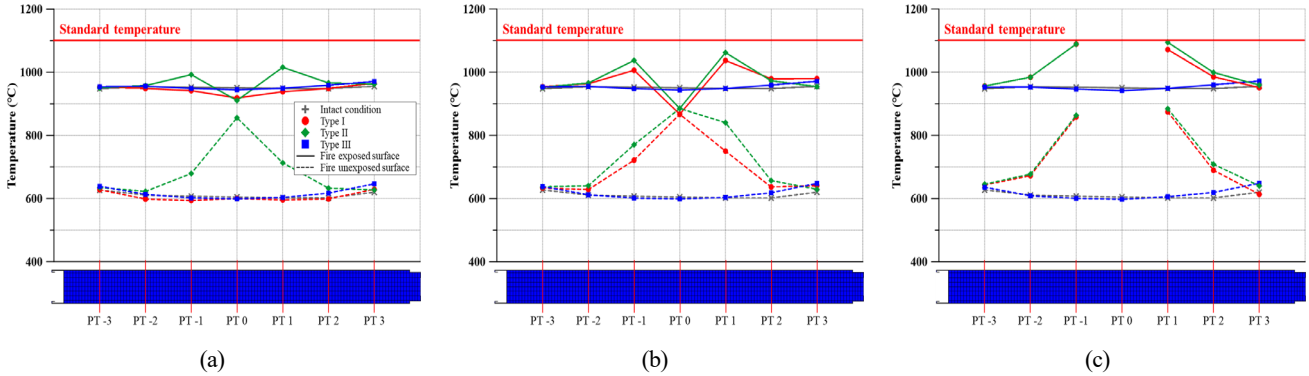

Fig. 14 Maximum temperature comparison at each point with varying impact velocities: (a) 8 m/s, (b) 10 m/s, and (c) 12 m/s

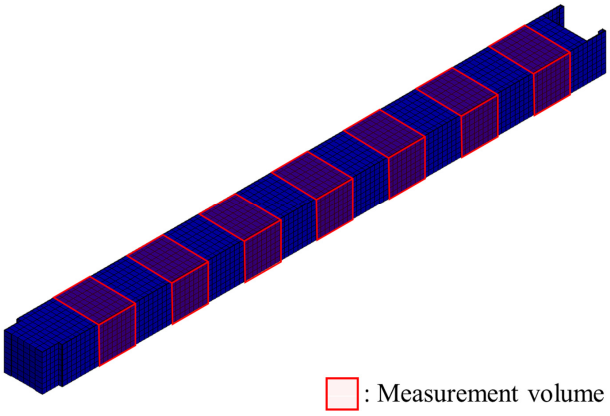

Fig. 15 Measurement point of damaged volume

characteristics differed according to the degree of damage. Therefore, the temperature characteristics showed a clear difference depending on the degree of damage, which was deemed necessary to evaluate the fire resistance performance of the firewall in consideration of the impact of the explosion, as proposed in this paper.

3.5.2 Comparison by fire exposure time

The fire resistance performance was compared in terms of temperature increase rate and time to reach reference temperature based on analysis results of the firewall panel damaged by "Type II" fragment when a thermal load was applied. Figs. 17−19 show the curve of fire exposure time-measurement temperature at the "PT-1", "PT0", and "PT1" points on the fire-exposed and unexposed surfaces of the central section of the firewall panel.

The temperature increase rate was compared in the range of 100 to 200°C, where the temperature increased rapidly, to quantitative analyze the change in fire resistance caused by damage, as shown in Fig. 20. Furthermore, the time to reach the reference temperature was derived according to the degree of damage, and 607.37°C was the maximum temperature of the fire unexposed surface at the intact firewall and used as the reference temperature.

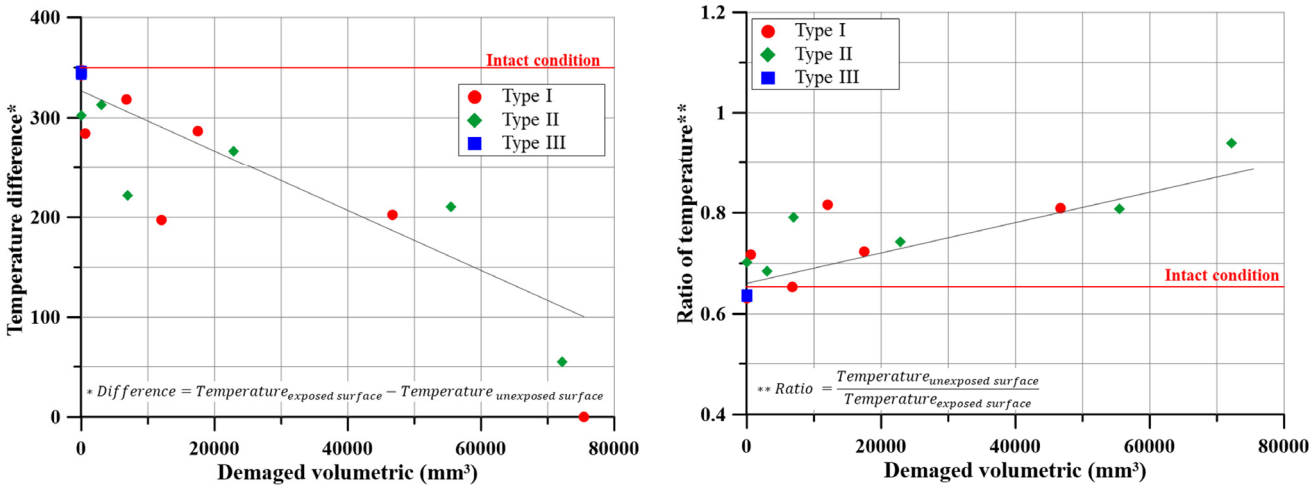

Fig. 16 Comparison of the temperature characteristics at different damaged volumes: (a) Temperature difference; (b) Temperature ratio

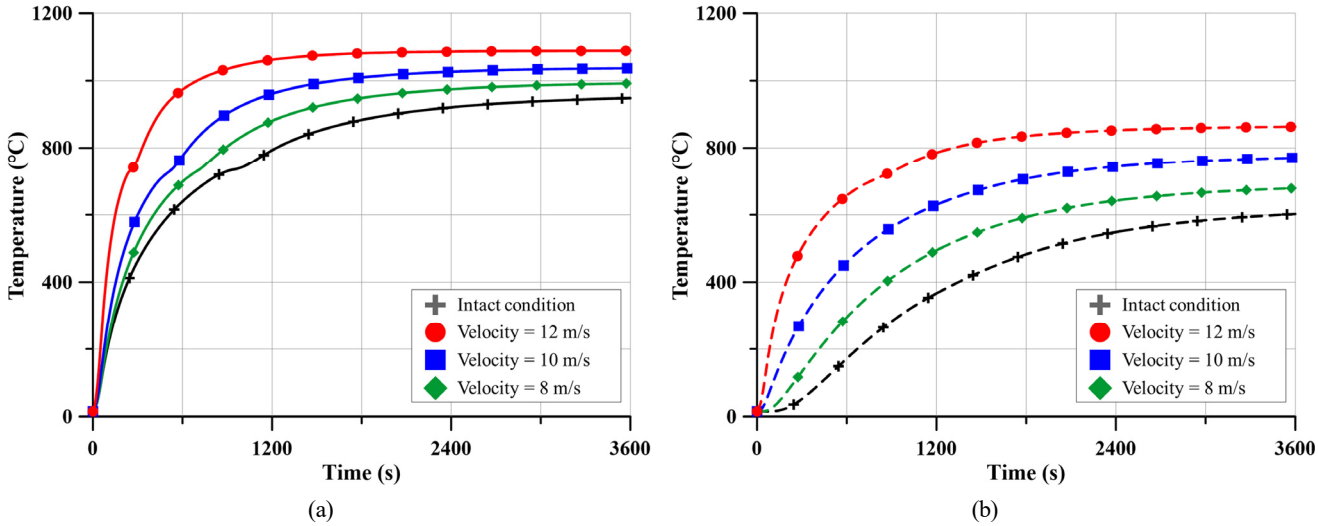

Fig. 17 Temperature comparison at "PT -1" with the varying impact velocities: (a) Fire-exposed surface; (b) Fire unexposed surface

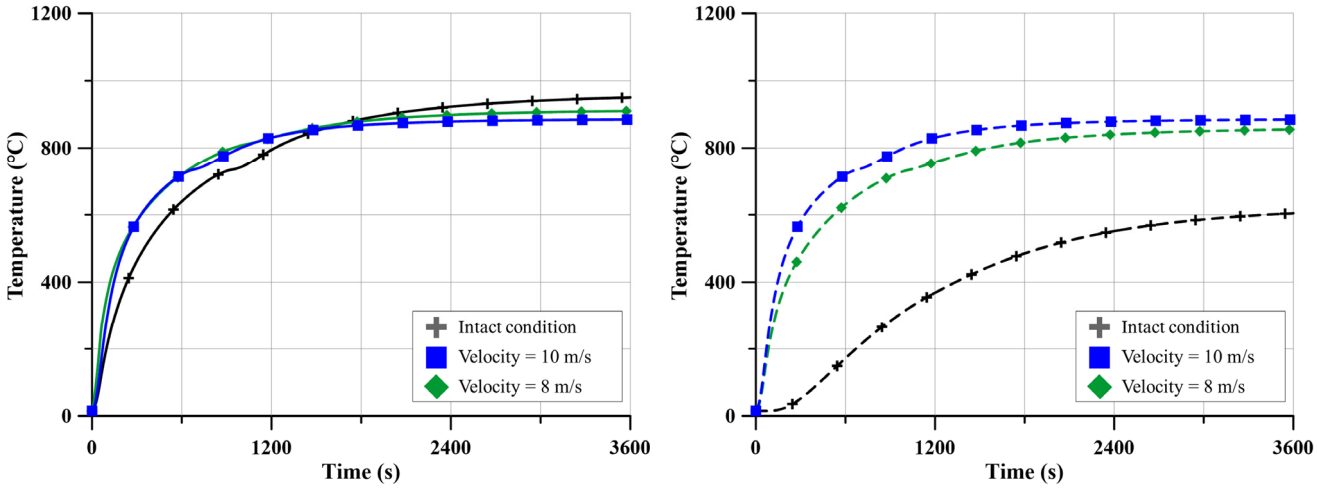

Fig. 18 Temperature comparison at "PT 0" with the varying impact velocities: (a) Fire-exposed surface; (b) Fire unexposed surface

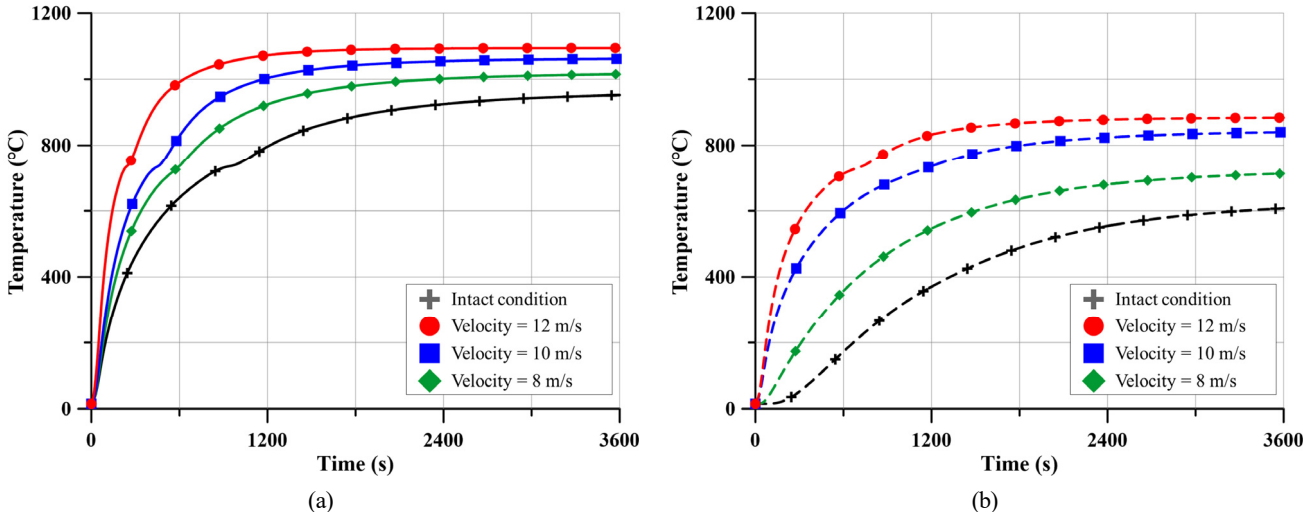

Fig. 19 Temperature comparison at "PT 1" with the varying impact velocities: (a) Fire-exposed surface; (b) Fire unexposed surface

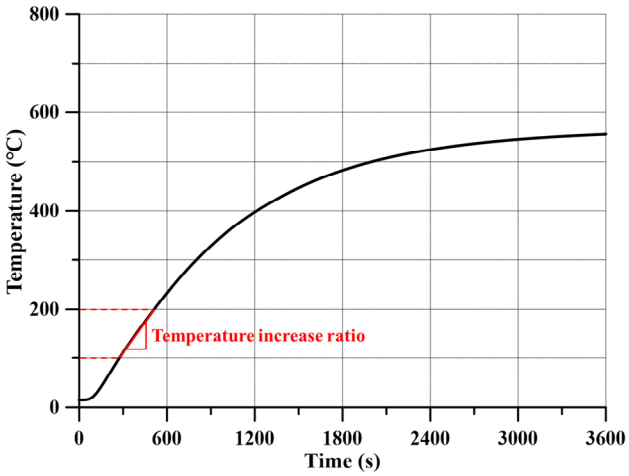

Fig. 20 Computational method of temperature increase ratio

Based on the results of Figs. 17–19, the maximum temperature, temperature increase rate, and time to reach reference temperature of fire-exposed and unexposed surfaces were organized in Table 6 by each measurement point. The temperature between 100–200°C tended to increase at an inclination of 0.59–3.70 depending on the degree of damage. Thermal-structural response analysis showed that the time to reach the reference temperature of the firewall panel collided with the corner of a cube scattered at a velocity of 10 m/s was a minimum of 5.63 minutes. Thus, firewall damage is expected to affect the evacuation time and structural aspects.

4. Conclusions

This study presented an advanced firewall design evaluation method for assessing the fire resistance performance associated with impact damage induced by explosions. Nine scenarios were selected to assess the variables for the shape and impact velocity of the fragments during a solid explosion. According to the evaluation method mentioned, the impact analysis was performed to determine the degree of damage owing to the explosion effect. Furthermore, the thermal-structural response analysis of the firewall panel applied with the degree of

Table 6 Comparison of the fire resistance performance.

No.	Impact velocity (m/s)	Measurement point no.	Maximum temperature (℃)		Temperature increase ratio	Time to reach temperature of 607.37℃ (min)
			Exposed surface	Unexposed surface		
1	- (Intact condition)	PT -1	952.31	607.37	0.41	60
2		PT 0	950.39	604.71	0.41	-
3		PT 1	948.47	602.27	0.41	-
4	8	PT -1	992.18	679.14	0.59	32.20
5		PT 0	910.28	855.55	2.93	8.95
6		PT 1	1015.47	712.94	0.71	25.95
7	10	PT -1	1037.15	770.30	1.06	18.09
8		PT 0	885.15	885.07	3.70	5.63
9		PT 1	712.94	840.10	2.36	10.28
10	12	PT -1	1088.95	863.32	2.92	7.91
11		PT 0	-	-	-	-
12		PT 1	1094.67	884.19	3.53	5.88

damage was performed, and the results were analyzed. The following conclusions were derived:

(1) In the present study, the existing fire resistance evaluation method was supplemented, and advanced fire resistance evaluation methods and thermal-structural response analysis modeling techniques were presented.

(2) A firewall panel with mineral wool, one of the materials of PFP, was selected as a target structure, and the impact analysis and the thermal-structural response analysis were performed to analyze thermal-structural characteristics by explosion damage.

(3) A comparison of the fire-exposed and the non-exposed surface of the firewall panel showed that as the temperature difference decreased, the temperature ratio tended to increase as the volume reduction rate of the structure. Scenario analysis showed that when the volume decreased by up to 94.46%, the temperature difference decreased by up to 99.97%, and the temperature ratio increased by up to 57.15%.

(4) A temperature increase rate of 0.41 was observed in the case of intact firewalls, but the temperature increased sharply to 0.59–3.70 in the case of damaged firewalls. Furthermore, the time to reach the reference temperature, 607.37℃ in this paper, was reduced by 90.62% compared to the intact firewall with a minimum of 5.63 minutes, depending on the degree of damage.

(5) Mineral wool is an insulating material and does not guarantee the resistance of the structure to damage, and research on dynamic material properties is insufficient. In this study, the dynamic fracture strain of mineral wool was estimated by parametric studies. Therefore, it is s necessary to derive the dynamic material properties through experiments on the target load, when a close investigation of the damage behavior characteristics of firewalls, including insulation materials, such as mineral wool materials.

(6) The fire resistance performance was analyzed in terms of the temperature difference and ratio, temperature increase rate, and the time to reach reference temperature between both surfaces of the firewall panel. As a result, there was a clear difference in performance depending on the degree of damage. This method is anticipated to be a variable when calculating the design load considering the explosion impact.

The advanced method can reduce the damage to human life and property caused by fires and explosions. The fire resistance performance evaluation considering fire/explosion accidents will be effectively realized if appropriate standards are in place for the proposed evaluation method.

Conflict of Interest

Jung Kwan Seo serves a journal publication committee member of the Journal of Ocean Engineering and Technology, but he had no role in the decision to publish this article. No potential conflict of interest relevant to this article was reported.

Funding

The authors would like to acknowledge the financial support provided by the Defense Rapid Acquisition Technology Research Institute (DRATRI) of Korea (Project code 912849501).

Acknowledgments

Some part of this study was presented in the 2022 Ocean Engineering CAE competition of the Korean Society of Ocean Engineers (KSOE).

References

European Committee Standardization. (2002). *Eurocode 1: Actions on structures – Part 1-2: General actions – Actions on structures exposed to fire* (BS EN 1991-1-2).

European Committee Standardization. (2005). *Eurocode 3: Design of steel structures −Part 1-2: General rules −Structural fire design* (BS EN 1993-1-2).

Center for Chemical Process Safety (CCPS). (1999). *Guidelines for chemical process quantitative risk analysis* (2nd ed.). Wiely.

Choung, J. M., Im, S. W., & Park, R. S. (2011). Plasticity and fracture behaviors of marine structural steel, part IV: Experimental study on mechanical properties at elevated temperatures. *Journal of Ocean Engineering and Technology, 25*(3), 66−72. https://doi.org/10.5574/KSOE.2011.25.3.066

Cowper, G. R., & Symonds, P. S. (1957). *Strain-hardening and strain-rate effects in the impact loading of cantilever beams* (Technical Report No. 28). Division of Applied Mathematics, Brown University.

D'Amore, G. K. O., Marino, A., & Kaspar, J. (2020). Numerical modeling of fire resistance test as a tool to design lightweight marine fire doors: A preliminary study. *Journal of Marine Science and Engineering, 8*(7), 520. https://doi.org/10.3390/jmse8070520

Federal Emergency Management Agency (FEMA). (2006). *Risk management series: design guidance for shelters and safe rooms* (FEMA 453). FEMA.

International Maritime Organization (IMO). (2002). *Chapter II-2 of SOLAS: construction −fire protection, fire detection and fire extinction*.

Kim, J. H., Lee, D. H., Ha, Y. C., Kim, B. J., Seo, J. K., & Paik, J. K. (2014). Methods for nonlinear structural response analysis of offshore structures with passive fire protection under fires. *Journal of Ocean Engineering and Technology, 28*(4), 294−305. https://doi.org/10.5574/KSOE.2014.28.4.294

Livermore Software Technology Corporation (LSTC). (2018). *User's manual for LS-DYNA*. LSTC.

Newmark N. M., & Hansen R. J. (1961). *Shock and vibration handbook, Vol. 3: design of blast resistant structures*. McGraw-Hill.

Paik, J. K., Kim, K. J., Lee, J. H., Jung, B. G., & Kim, S. J. (2017). Test database of the mechanical properties of mild, high-tensile and stainless steel and aluminium alloy associated with cold temperatures and strain rates. *Ships and Offshore Structures, 12*(sub1), s230−s256. https://doi.org/10.1080/17445302.2016.1262729

Park, D. K., Kim, J. H., Park, J. S., Ha, Y.C., & Seo, J. K. (2021). Effect of the structural strength of fire protection insulation systems in offshore installations. *International Journal of Naval Architecture and Ocean Engineering, 13,* 493−510. https://doi.org/10.1016/j.ijnaoe.2021.06.001

Park, W. C., & Song, C. Y. (2019). Heat transfer characteristics of bulkhead penetration piece for A60 class compartment II: Fire resistance test for piece material and insulation types. *Journal of Ocean Engineering and Technology, 33*(4), 340−349. https://doi.org/10.26748/KSOE.2019.027

Park, W. C., & Song, C. Y. (2021). Evaluation on sensitivity and approximate modeling of fire-resistance performance for A60 class deck penetration piece using heat-transfer analysis and fire test. *Journal of Ocean Engineering and Technology, 35*(2), 141−149. https://doi.org/10.26748/KSOE.2021.012

Seo, J.K., Lee, S.E., Park, J.S. (2017). A method for determining fire accidental loads and its application to thermal response analysis for optimal design of offshore thin-walled structures. *Fire Safety Journal*, 92,107-121. http://dx.doi.org/10.1016/j.firesaf.2017.05.022

Transportation Safety Board of Canada (TSB). (2021). *Statistical summary: marine transportation occurrences in 2020*. Gatineau, Canada: TSB.

U.S. Department of defense. (2007). *Department of defense standard practice: fire resistance of U.S. naval surface ships* (MIL-STD-3020).

Author ORCIDs

Author name	ORCID
Cho, Hyerim	0000-0002-3758-747X
Yoo, Jeonghwa	0000-0002-1159-4938
Seo, Jungkwan	0000-0002-3721-2432

KSOE

Journal of Ocean Engineering and Technology 37(3), 111-121, June, 2023
https://doi.org/10.26748/KSOE.2023.004

pISSN 1225-0767
eISSN 2287-6715

Original Research Article

Collision Simulation of a Floating Offshore Wind Turbine Considering Ductile Fracture and Hydrodynamics Using Hydrodynamic Plug-in HydroQus

Dong Ho Yoon[1] and Joonmo Choung[2]

[1]*Graduate Student, Department of Naval Architecture and Ocean Engineering, Inha University, Incheon, Korea*
[2]*Professor, Department of Naval Architecture and Ocean Engineering, Inha University, Incheon, Korea*

KEYWORDS: Floating offshore wind turbine, Collision, Ductile fracture, Hydrodynamics, Fluid-structure interaction

ABSTRACT: *This paper intends to introduce the applicability of HydroQus to a problem of a tanker collision against a semi-submersible type floating offshore wind turbine (FOWT). HydroQus is a plug-in based on potential flow theory that generates interactive hydroforces in a commercial Finite element analysis (FEA) code Abaqus/Explicit. Frequency response analyses were conducted for a 10MW capacity FOWT to obtain hydrostatic and hydrodynamic constants. The tanker was modeled with rigid elements, while elastic-plastic elements were used for the FOWT. Mooring chains were modeled to implement station keeping ability of the FOWT. Two types of fracture models were considered: constant failure strain model and combined failure strain model HC-LN model composed of Hosford-Coulomb (HC) model & localized necking (LN) model. The damage extents were evaluated by hydroforces and failure strain models. The largest equivalent plastic strain observed in the cases where both restoring force and radiation force were considered. Stress triaxiality and damage indicator analysis showed that the application of HC-LN model was suitable. It could be stated that applications of suitable failure strain model and hydrodynamics into the collision simulations were of importance.*

1. Introduction

Along with the continuous upsizing of offshore wind turbine (OWT) units to reduce the cost of power generation, commercial farms are also becoming larger. As commercial farms become larger, ships must be allowed to pass through them, increasing the likelihood of collisions with OWTs. A cargo ship collided with an OWT at a 330 MW commercial wind farm in Germany (Jasmina, 2023). Furthermore, collisions can lead to significant damage to floating OWTs (FOWTs), such as structural damage and loss of stability due to flooding, while ships can cause economic and environmental losses such as cargo loss and oil spills, as well as loss of life. To prepare for this, the Det Norske Veritas (DNV) offshore standard (DNV, 2013) provides design guidance for accidental ship collisions.

Dai et al. (2013) studied the collision of a fixed wind turbine with a monopile substructure and a 230-ton vessel and provided suggestions for collision risk reduction. Moulas et al. (2017) studied the collision of an OWT with a 4,000-ton ship on monopile and jacket substructures. They considered different ship speeds and collision angles, but environmental loads such as wind and wave loads were not considered. Bela et al. (2017) performed a collision analysis between a 5,000-ton vessel and an OWT with a monopile substructure. The effects of ship speed, wind load, and soil stiffness on the collision were analyzed, but hydrodynamic forces acting on the ship were not considered.

Echeverry et al. (2019) performed a collision analysis of a spar-type FOWT and Márquez et al. (2022) studied the collision of a reinforced concrete barge-type FOWT with a 3,000-ton ship. Both studies used MCOL to consider hydrodynamic forces, but did not consider wave and wind loads. Zhang and Hu (2022) studied the collision of a spar-type FOWT with a 4,000-ton ship. User subroutines were used in LS-DYNA (LSTC, 2023) to implement aerodynamics and hydrodynamics. The drag force on the rotor area was calculated and the wind thrust load was applied as a point load to the center of the rotor. Since it was difficult to accurately model the initial mooring layout, instead of directly modeling the mooring lines, the linearized restoring matrix proposed by Jonkman (2007) was applied.

This study aims to address the collision of a 10 MW semi-submersible FOWT with a 5,000 ton ship using Abaqus/Explicit (Simulia, 2021). In order to generate fluid forces in Abaqus, either

Received 27 March 2023, revised 5 June 2023, accepted 6 June 2023
Corresponding author Joonmo Choung: +82-32-860-7346, heroeswise2@gmail.com

arbitrary Lagrangina Eulerian (ALE) or coupled Eulerian Lagrangian (CEL) must be utilized. However, the adoption of ALE or CEL requires too long computational time, so in this study, HydroQus developed by Han (2022) and Yoon et al. (2023) is used to perform the collision analysis of ship and FOWT. HydroQus is a plug-in of the commercial finite element analysis (FEA) code Abaqus that generates real-time hydrodynamic forces. HydroQus calculates hydrodynamic forces such as radiation force, wave excitation force, as well as restoring force acting on the FOWT in real time. Yoon et al. (2023) verified the accuracy of HydroQus and performed a collision analysis between a ship and an iceberg. The mooring of the FOWT was modeled using beam elements and joint elements. The HC-LN model, a synthesis of the Hosford-Coulomb (HC) model and the localized necking (LN) model, was used to accurately predict the structural damage caused by the collision. A user subroutine developed by Cerik et al. (2019) was applied to implement the HC-LN model in Abaqus.

2. Theoretical Background

2.1 Governing Equations for HydroQus

According to Newton's second law, the governing equation of motion for a floating body can be expressed as Eq. (1). M_{ij} is the mass of a floating body, and $\ddot{u}_j$ is the acceleration of a floating body. The subscript i and j represent 6 degrees of freedom, 1 = surge, 2 = sway, 3 = heave, 4 = roll, 5 = pitch, and 6 = yaw. The restoring force F_i^{res} is calculated from the hydrostatic stiffness C_{ij} and the displacement of a floating body u_j as shown in Eq. (2). According to Cummin's equation, the radiation force F_i^{rad} is expressed as Eq. (3). It is important that t_1 should be long enough for the impulse response function K_{ij} to converge stably to zero. The wave damping coefficient $B_{ij}(\omega)$ obtained through frequency response analysis is used to calculate the impulse response function as shown in Eq. (5). The added mass $m_{ij}(\infty)$ can be calculated by Eq. (4). The wave excitation force F_i^{wv} for the regular wave is defined as Eq. (6). F_i is the response amplitude operator (RAO) of the wave excitation force obtained by frequency response analysis, H is the wave height and ϕ is the wave phase. The mooring force F_i^{mr} due to the mooring line and the impact force F_i^{col} due to the collision of the FOWT with the tanker are calculated in Abaqus.

$$M_{ij}\ddot{u}_j(t) = F_i^{res}(t) + F_i^{rad}(t) + F_i^{wv}(t) + F_i^{mr}(t) + F_i^{col}(t) \tag{1}$$

$$F_i^{res}(t) = C_{ij}u_j(t) \tag{2}$$

$$F_i^{rad}(t) = m_{ij}(\infty)\ddot{u}_j(t) + \int_0^{t1} K_{ij}(t-\tau)\dot{u}_j(t)d\tau \tag{3}$$

$$m_{ij}(\infty) = m_{ij}(\omega) + \int_0^{\infty} K_{ij}(\tau)\frac{\sin(\omega\tau)}{\omega}d\tau \tag{4}$$

$$K_{ij}(t) = \frac{2}{\pi}\int_0^{\infty} B_{ij}(\omega)\cos(\omega t)d\omega \tag{5}$$

$$F_i^{wv}(t) = \frac{H}{2}F_i(\omega)\cos(-\omega t + \phi) \tag{6}$$

For modeling the mooring lines, the catenary equations presented in the studies of Masciola et al. (2013) and Jonkman (2007) were used, and are given by Eqs. (7)–(14). l and h denote the vertical and horizontal positions of the fairlead, respectively. H and V are the horizontal and vertical forces at the fairlead. EA, W, and L are the properties of the mooring line: axial stiffness, weight per unit length, and unstretched length. C_B is the friction coefficient between seabed and mooring line and L_B is the laid length on seabed. By calculating Eq. (10) and Eq. (11), the location along the line segment s is derived, which are used to model mooring lines.

$$l = L_B + \frac{H}{W}\sinh^{-1}\left(\frac{V}{H}\right) + \frac{HL}{EA} + \frac{C_B W}{2EA}\left[\mu\left(L - \frac{V}{W} - \frac{H}{C_b W}\right) - \left(L - \frac{V}{W}\right)^2\right] \tag{7}$$

$$h = \frac{H}{W}\left[\sqrt{1+\left(\frac{V}{H}\right)^2} - 1\right] + \frac{V^2}{2EAW} \tag{8}$$

$$\mu = \begin{cases} L - \dfrac{V}{W} - \dfrac{H}{C_B W} & for\left(L - \dfrac{V}{W} - \dfrac{H}{C_B W}\right) > 0 \\ 0 & otherwise \end{cases} \tag{9}$$

$$x(s) = \begin{cases} s & for\ 0 \le s \le \gamma \\ s + \dfrac{C_B W}{2EA}\left[s^2 - 2s\gamma + \gamma\right] & for\ \gamma \le s \le L_B \\ L_B + H_W \sinh^{-1}\left[\dfrac{W(s-L_B)}{H}\right] + \dfrac{HS}{EA} + \dfrac{C_B W}{2EA}\left[\lambda\gamma - L_B^2\right] & for\ L_B \le s \le L \end{cases} \tag{10}$$

$$z(s) = \begin{cases} 0 & for\ 0 \le s \le L_B \\ \dfrac{H}{W}\left[\sqrt{1+\left(\dfrac{W(s-L_B)}{H}\right)^2} - 1\right] + \dfrac{W(s-L_B)^2}{2EA} & for\ L_B \le s \le L \end{cases} \tag{11}$$

$$\gamma = L_B - \frac{H}{C_B W} \tag{12}$$

$$\lambda = \begin{cases} \gamma & for\ \gamma > 0 \\ 0 & otherwise \end{cases} \tag{13}$$

$$L_B = L - \frac{V}{W} \tag{14}$$

2.2 Process of Fluid-structure Interaction

Abaqus is a commercial FEA code that includes a variety of material constitutive equations and a robust contact algorithm. However, Abaqus is not capable of generating hydrodynamic forces based on potential flow theory on its own. To solve this problem, the authors of

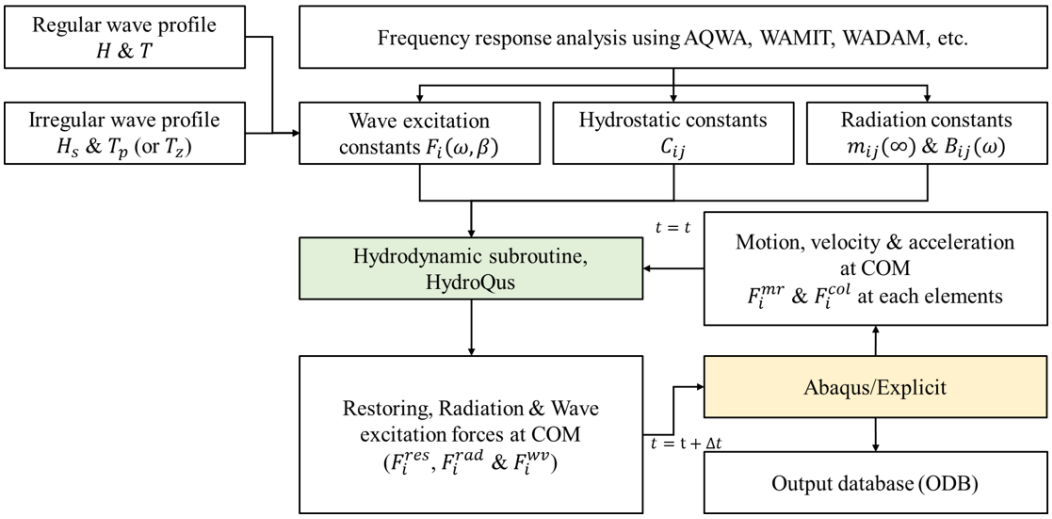

Fig. 1 Flow chart of fluid-structure interaction scheme using HydroQus

this paper developed HydroQus, a hydrodynamic plug-in compatible with Abaqus/Explicit. HydroQus can generate linear or nonlinear restoring forces, radiation forces, and 1st and 2nd order wave excitation forces. The hydrodynamic coefficients used in the calculations must be obtained in advance from a frequency response analysis. For the wave excitation force calculation, the wave height H (or significant wave height H_s) and wave period T (or peak period T_p) must be defined. HydroQus calculates the hydrodynamic forces using the displacement, velocity, and acceleration at the center of mass (CoM) of the FOWT at $t = t_1$ (current time) in Abaqus and gives them to Abaqus/Explicit. Abaqus solves the equations of motion for the FOWT and the ship, respectively, using the hydrodynamic forces. During this process, Abaqus is responsible for generating the drag-based mooring tension forces and collision forces. The displacements, velocities, and accelerations at the CoM obtained by solving the equations of motion are fed back to HydroQus and used to generate the hydrodynamic forces at $t = t_2$ (next time). This procedure is summarized in Fig. 1.

2.3 Flow Stress and Fracture Model

To accurately represent the hardening behavior after onset of necking, the combined Swift-Voce hardening model proposed by Sung et al. (2010) is applied in this study. The Swift-Voce hardening law is given by Eq. (15), where α is the weighting factor between Swift law and Voce law. The Swift law and Voce law are given by Eq. (16) and Eq. (17), respectively. Cerik and Choung (2020) derived A, ε_0, n, k_0, Q, and β through tensile tests and numerical analyses.

$$k[\bar{\varepsilon}_p] = \alpha k_s[\bar{\varepsilon}_p] + (1-\alpha)k_v[\bar{\varepsilon}_p] \tag{15}$$

$$k_s[\bar{\varepsilon}_p] = A(\varepsilon_0 + \bar{\varepsilon}_p)^n \tag{16}$$

$$k_v[\bar{\varepsilon}_p] = k_0 + Q(1-\exp[-\beta\bar{\varepsilon}_p]) \tag{17}$$

The fracture strain in the HC model proposed by Mohr and Marcadet (2015) is given by Eq. (18). Where η is the stress triaxiality and $\bar{\theta}$ is the Lode angle. From Eq. (18) and Eq. (19), a is the load angle sensitivity, b is the fracture strain modulus, c is the stress triaxiality sensitivity, and n_f is the transformation exponent. The load angle parameter functions f_1, f_2 and f_3 are calculated through Eqs. (20)–(22). To consider the stress path effect, the damage indicator D in Eq. (23) is introduced. It is assumed that fracture initiates when the damage indicator reaches 1.0.

$$\bar{\varepsilon}^{pr}_{HC}[\eta,\bar{\theta}] = b(1+c)^{\frac{1}{n_f}} g[\eta,\bar{\theta}] \tag{18}$$

$$g[\eta,\bar{\theta}] = \left(\left\{\frac{1}{2}((f_1-f_2)^a + (f_1-f_3)^a + (f_2-f_3)^a)\right\}^{\frac{1}{a}} + c(2\eta + f_1 + f_3)\right)^{\frac{1}{n_f}} \tag{19}$$

$$f_1[\bar{\theta}] = \frac{2}{3}\cos\left[\frac{\pi}{6}(1-\bar{\theta})\right] \tag{20}$$

$$f_2[\bar{\theta}] = \frac{2}{3}\cos\left[\frac{\pi}{6}(3+\bar{\theta})\right] \tag{21}$$

$$f_3[\bar{\theta}] = -\frac{2}{3}\cos\left[\frac{\pi}{6}(1+\bar{\theta})\right] \tag{22}$$

$$dD = \frac{d\bar{\varepsilon}_p}{\bar{\varepsilon}^{pr}_{HC}[\eta,\bar{\theta}]} \tag{23}$$

The LN fracture strain model proposed by Pack and Mohr (2017) is given by Eq. (24). Where d is the Hosford exponent and p_f is the transformation exponent. Stress triaxiality functions g_1 and g_2 are calculated using Eq. (25) and Eq. (26). A necking indicator N is introduced to consider the stress path effect (see Eq. (27)). Fracture is considered to occur when N reaches 1.0.

$$\bar{\varepsilon}^{pr}_{LN}[\eta] = b\left(\left\{\frac{1}{2}((g_1-g_2)^d + g_1^d + g_2^d)\right\}^{\frac{1}{d}}\right)^{-\frac{1}{p_f}} \tag{24}$$

$$g_1[\eta] = \frac{3}{2}\eta - \sqrt{\frac{1}{3} - \frac{3}{4}\eta^2} \tag{25}$$

$$g_2[\eta] = \frac{3}{2}\eta - \sqrt{\frac{1}{3} - \frac{3}{4}\eta^2} \tag{26}$$

$$dN = \frac{d\bar{\varepsilon}_p}{\bar{\varepsilon}^{pr}_{LN}[\eta]} \quad for \ \frac{1}{3} < \eta < \frac{2}{3} \tag{27}$$

3. Setup of FOWT-tanker Collision Simulation

3.1 Frequency Response Analysis

Fig. 2 is the model of FOWT used for the frequency response analysis. The frequency response analysis model consisted of approximately 5,500 diffraction elements and 4,500 non-diffraction elements. Tower and RNA were not included in the model, but were included in the mass information. Table 1 shows the mass information of the FOWT.

Frequency response analysis was performed using Aqwa (Ansys, 2022). The results of frequency response analysis in head sea condition are shown in Fig. 3 which includes the heave and pitch motion response amplitude operators (RAOs). The corresponding radiation coefficients for surge, sway, heave, roll, pitch and yaw motions are shown in Figs. 3(b)-3(g). It can be seen that the added masses nearly converged to a certain value as the frequency increased. The wave damping coefficients also nearly converged to zero as the frequency increased. Fig. 3(h) shows the 1st order wave excitation force RAOs in the heave and pitch directions.

Table 1 Principal dimensions and mass information of the FOWT

Item	Value
Draft (m)	15.5
Displacement (t)	10728.0
Vertical center of mass from waterline (m)	4.58
2nd moment of inertia for roll (t-mm^2)	1.96E13
2nd moment of inertia for pitch (t-mm^2)	1.96E13
2nd moment of inertia for yaw (t-mm^2)	1.30E13

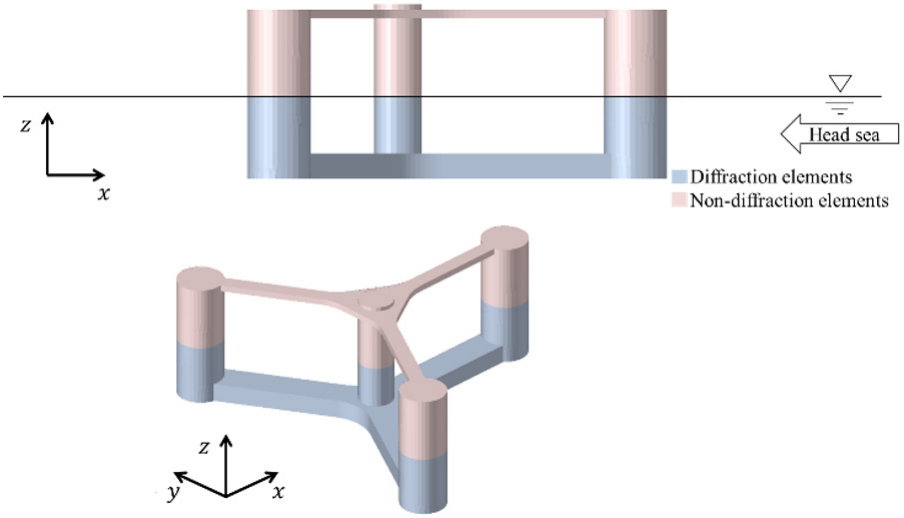

Fig. 2 Frequency response analysis model

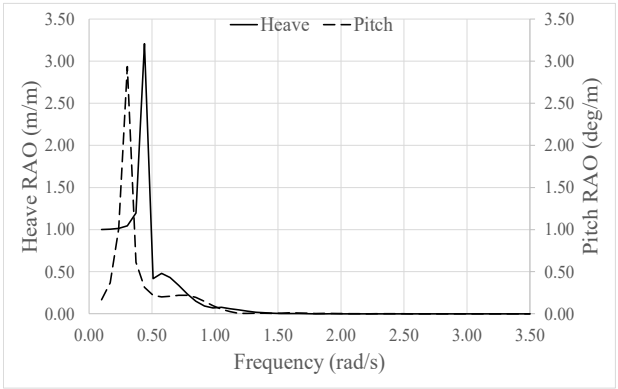

(a)

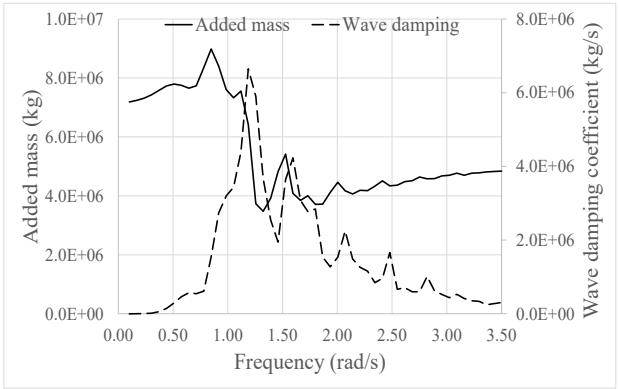

(b)

Fig. 3 Frequency response analysis results: (a) Motion RAOs; (b) Radiation coefficients in surge direction; (c) Radiation coefficients in sway direction; (d) Radiation coefficients in heave direction; (e) Radiation coefficients in roll direction; (f) Radiation coefficients in pitch direction; (g) Radiation coefficients in yaw direction; (h) Wave excitation forces

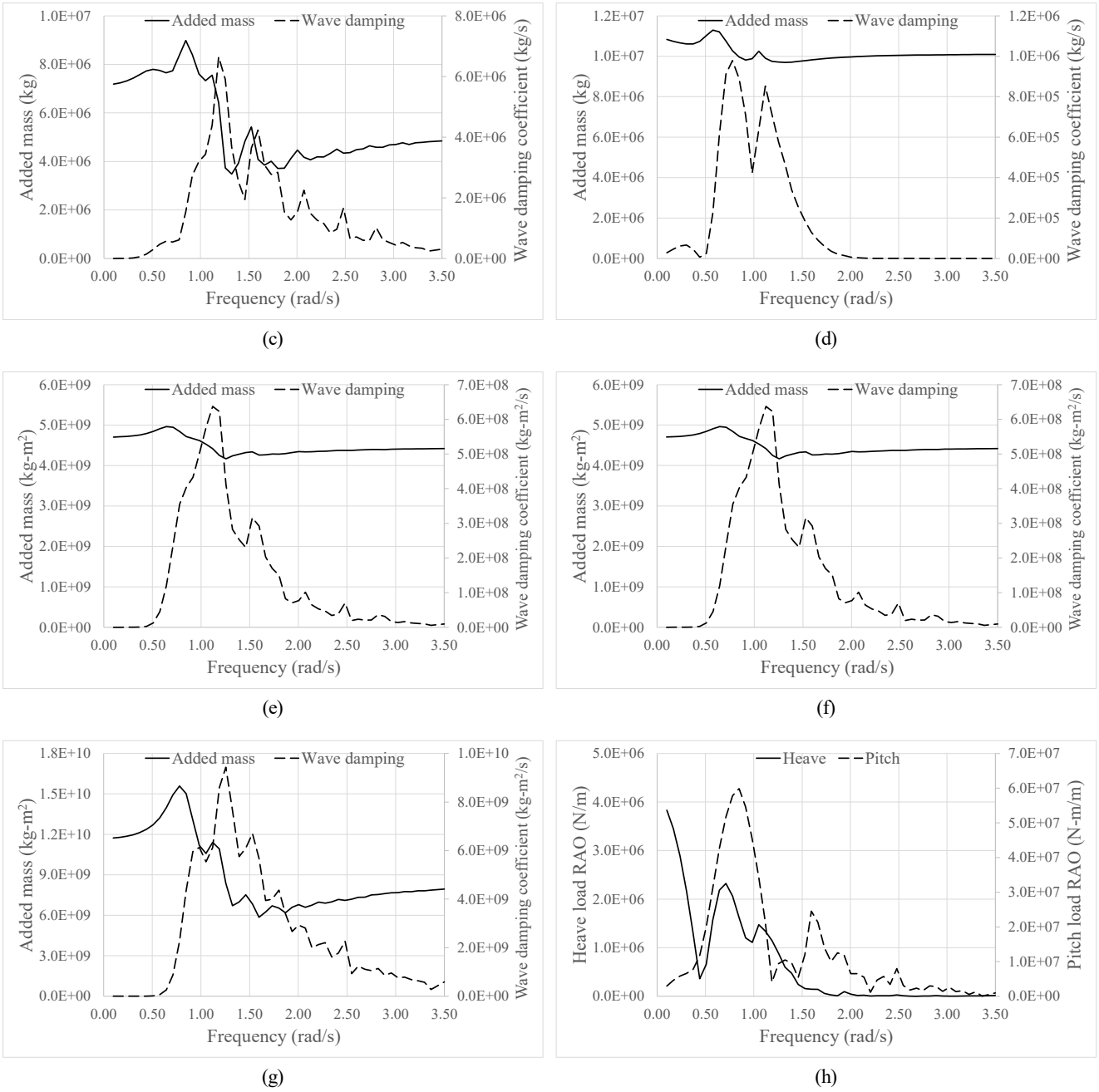

Fig. 3 Frequency response analysis results: (a) Motion RAOs; (b) Radiation coefficients in surge direction; (c) Radiation coefficients in sway direction; (d) Radiation coefficients in heave direction; (e) Radiation coefficients in roll direction; (f) Radiation coefficients in pitch direction; (g) Radiation coefficients in yaw direction; (h) Wave excitation forces (continuation)

3.2 Finite Element Models for Collision Simulation

The tanker used in the collision simulations is shown in Fig. 4. In this study, the tanker was assumed to be a rigid body of R3D3 and R3D4 shell elements, while a MASS element, and a ROTARYI element were used to represent the mass. The main dimensions and masses of the ship are shown in Table 2.

The FOWT was modeled with shell elements S3R and S4R. The element size was the longitudinal stiffener spacing, but the element size was reduced to 1/8 of the longitudinal stiffener spacing in the area where collisions were expected. The FEA model of the FOWT is summarized in Fig. 5 and Table 3.

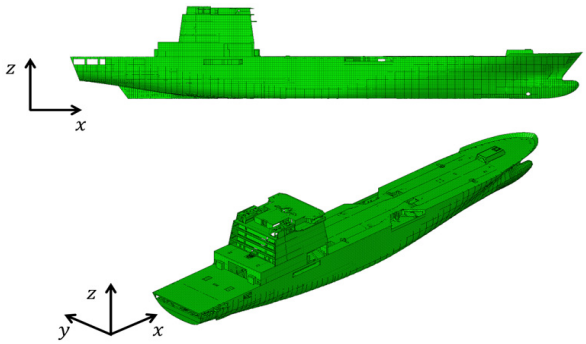

Fig. 4 Finite element model of tanker

Table 2 Modeling information of tanker

Item	Value
Length overall (m)	114.94
Molded breadth (m)	15.05
Molded depth (m)	10.01
Draft (m)	4.9
Displacement (t)	5000
Vertical center of mass from baseline (m)	5.48
2nd moment of inertia for roll (t-mm^2)	1.22E11
2nd moment of inertia for pitch (t-mm^2)	3.02E12
2nd moment of inertia for yaw (t-mm^2)	3.08E12
Element type	R3D3 R3D4
Number of elements	47,734

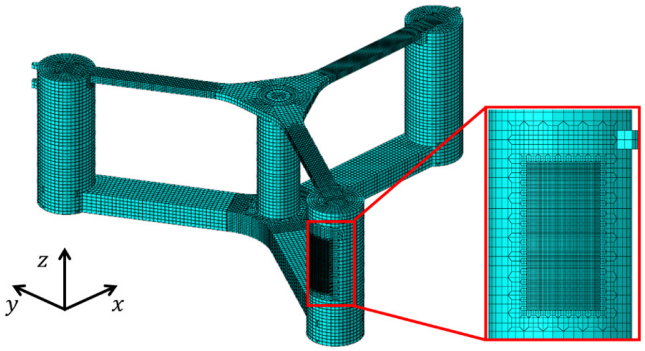

Fig. 5 Finite element model of floater

Table 3 Modeling information of floater

Item	Value
Column span (m)	45.00
Column height (m)	33.00
Outer column diameter (m)	12.00
Tower column diameter (m)	9.00
Steel mass (t)	3400
2nd moment of inertia for roll (t-mm^2)	8.57E12
2nd moment of inertia for pitch (t-mm^2)	8.57E12
2nd moment of inertia for yaw (t-mm^2)	1.29E13
Element type	S3R S4R
Number of elements	31,483

The initial layout of the mooring lines was determined using the catenary equation. The mooring lines were modeled using beam element (B31) and joint element (UJOINT) connecting the beam elements to allow rotation. The seabed was modeled as a rigid element. The modeled seabed and mooring lines layout is shown in Fig. 6. Table 4 presents the modeling information of seabed and mooring line.

The DTU 10 MW wind turbine (Borg et al., 2015) released by the LIFES50+ project was used to model the tower and RNA (see Table 5).

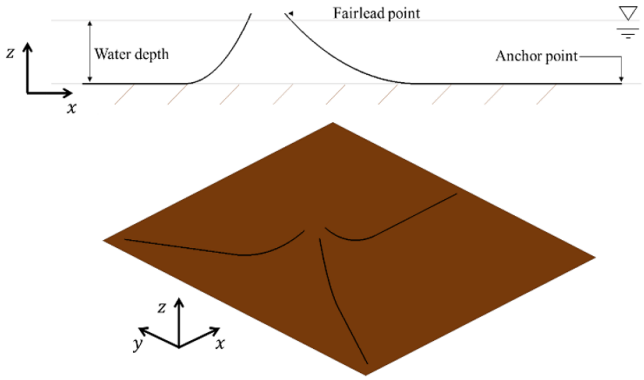

Fig. 6 Layout of mooring lines

Table 4 Modeling information for mooring system

Item	Value
Line diameter (m)	0.147
Axial stiffness (N)	1.845E9
Mass per unit length (kg/m)	430.0
Unstretched length (m)	850.0
Water depth (m)	150.0
Anchor to fairlead (m)	800.0
Fairlead from water line (m)	13.01
Friction coefficient	0.5
Element type of line	B31 UJOINT
Seabed stiffness	Rigid

Table 5 Modeling information of tower and RNA

Item	Value
Rotor diameter (m)	178.3
Hub diameter (m)	5.6
Hub height (m)	119.0
Number of blades	3
Rotor mass (t)	227.96
Nacelle mass (t)	446.04
Tower mass (t)	628.44
Element type	S3R S4R

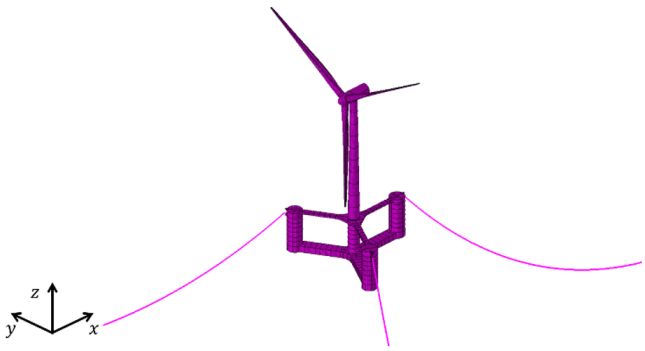

Fig. 7 Overall system layout of FOWT

Fig. 7 shows the FEA model of the complete FOWT including mooring lines, floating body, tower, and RNA.

3.3 Material Properties for Finite Element Model

In this study, the floating body of the FOWT is made of AH36 steel for ship structures. In this study, the combined Swift-Voce hardening law was used to define the flow stress of this steel. The material constants of the combined Swift-Voce hardening law were determined based on the tensile test results by Park et al. (2020) (see Fig. 8). They also conducted a series of fracture tests. Their results were used in this study to obtain the fracture strain locus as shown in Fig. 9.

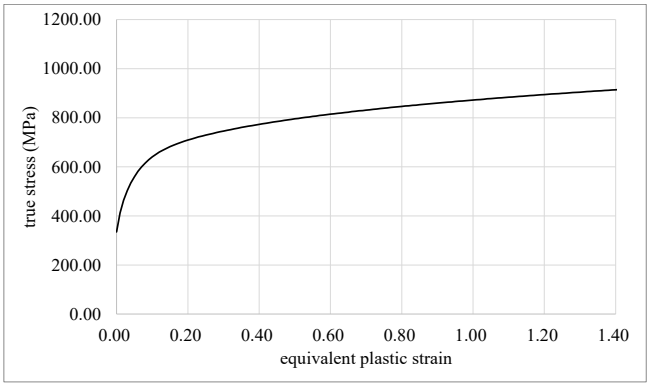

Fig. 8 Flow stress curve for AH36

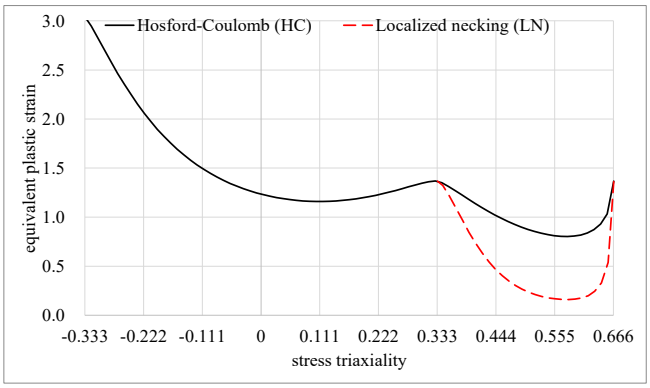

Fig. 9 Fracture strain curve for AH36

3.4 Collision Analysis Cases

The objective of this study is unfolded into two. The first objective is to determine the impact of hydrodynamic forces on structural damage in a FOWT-tanker collision. Therefore, the cases were divided into those before and after considering hydrostatic restoring force and radiation force in the collision simulations. The second objective is to determine the impact of the fracture model on the structural damage assessment. For this purpose, the cases were divided into those with the HC-LN fracture model applied and those defined by a constant failure strain ε_f. In this case, ε_f was assumed to be 0.2, which has been the most widely used failure strain. Six cases were generated, which are summarized in Table 6. In all cases, the initial forward velocity of the tanker was assumed to be 5 knots (9.26 km/h). The collision analysis model is shown in Fig. 10.

Table 6 Collision cases

Case	Hydrodynamic force	Fracture model	Tanker velocity
Case1-1	n/a	ε_f = 0.2	5 knot (9.26 km/h)
Case1-2	n/a	HC-LN	
Case2-1	Buoyancy	ε_f = 0.2	
Case2-2	Buoyancy	HC-LN	
Case3-1	Buoyancy + Radiation	ε_f = 0.2	
Case3-2	Buoyancy + Radiation	HC-LN	

4. FOWT-tanker Collision Simulation Results

4.1 Equivalent Plastic Strain

The equivalent plastic strain is an important measure for determining the extent of damage. The equivalent plastic strain distribution just after the collision process is finished are shown in Fig. 11. Comparing the corresponding cases before and after considering hydrostatic force and hydrodynamic force (for example, comparing Case1-1, Case2-1 and Case3-1, or Case1-2, Case2-2, and Case3-2), there are no significant differences in the equivalent plastic strain

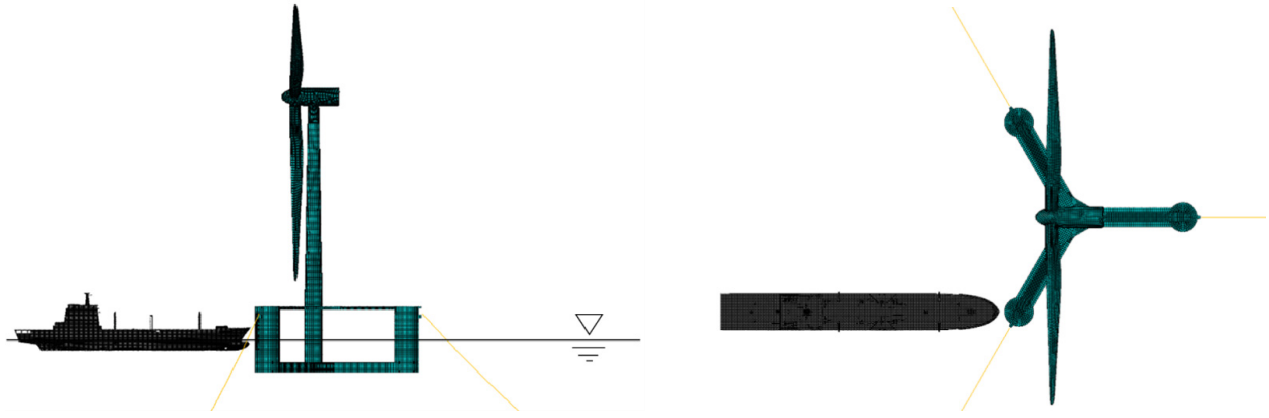

(a) (b)

Fig. 10 Relative position between FOWT and tanker: (a) Side-view; (b) Top-view

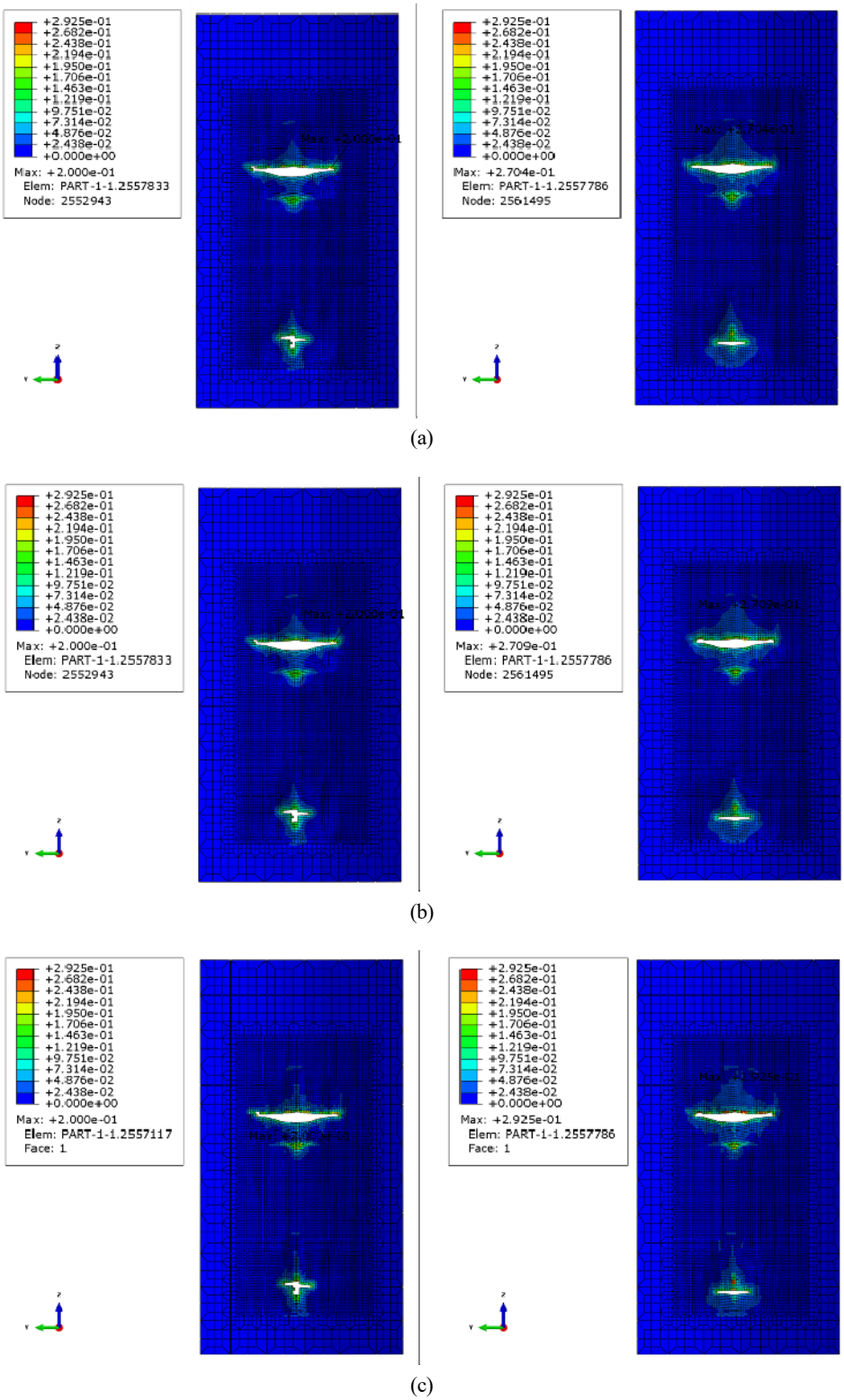

Fig. 11 Equivalent plastic strain distribution: (a) Case1-1 & Case1-2; (b) Case2-1 & Case2-2; (c) Case3-1 & Case3-2

distributions and maximum equivalent plastic strains. When comparing the constant failure strain model with the HC = LN model (e.g., Case1-1 and Case1-2), constant failure strain model shows similar damage extents as the HC-LN model, although the maximum equivalent plastic strains were developed up to 0.2 with the constant failure strain model.

4.2 Damage Extent

In this study, the damage extent is defined as the failed area of the side shell. The ratio of the damage extent with constant failure strain model divided by that with HC-LN model is shown in Fig. 12. In all cases, this ratio exceeds 1.0, which means that the constant failure strain model predicts larger damage extents than the HC-LN model.

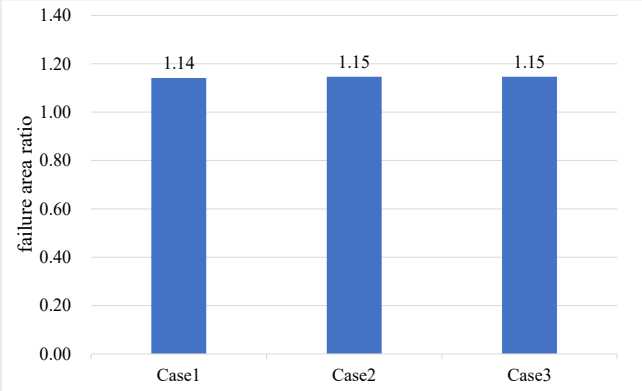

Fig. 12 Failure area ratio

4.3 Triaxiality and Damage Indicator

The stress triaxiality and damage indicators of Case3-2 were analyzed as an example. The stress triaxiality immediately after the collision occurred is shown in Fig. 13(a). It can be seen from Fig. 13(a) that the stress triaxiality in the collision area corresponds to the biaxial tension. A stress path at a fracture initiation location was formed with this stress triaxiality and the necking damage was accumulated. After the collision was completely terminated, the necking indicator and ductile fracture damage indicator are shown in Fig. 13(b)–(c), respectively. As expected, we can see that the LN necking damage indicator was developed much larger than the HC damage indicator.

5. Conclusions

The authors of this study developed HydroQus, a hydrodynamic plug-in that can calculate hydroforces such as hydrostatic restoring force and hydrodynamic radiation/wave excitation forces. Using HydroQus to implement the hydrodynamic forces acting on the FOWT, a FOWT-tanker collision analysis was performed. Two different fracture models (constant failure strain model and HC-LC model) were applied to the collision simulations with and without the

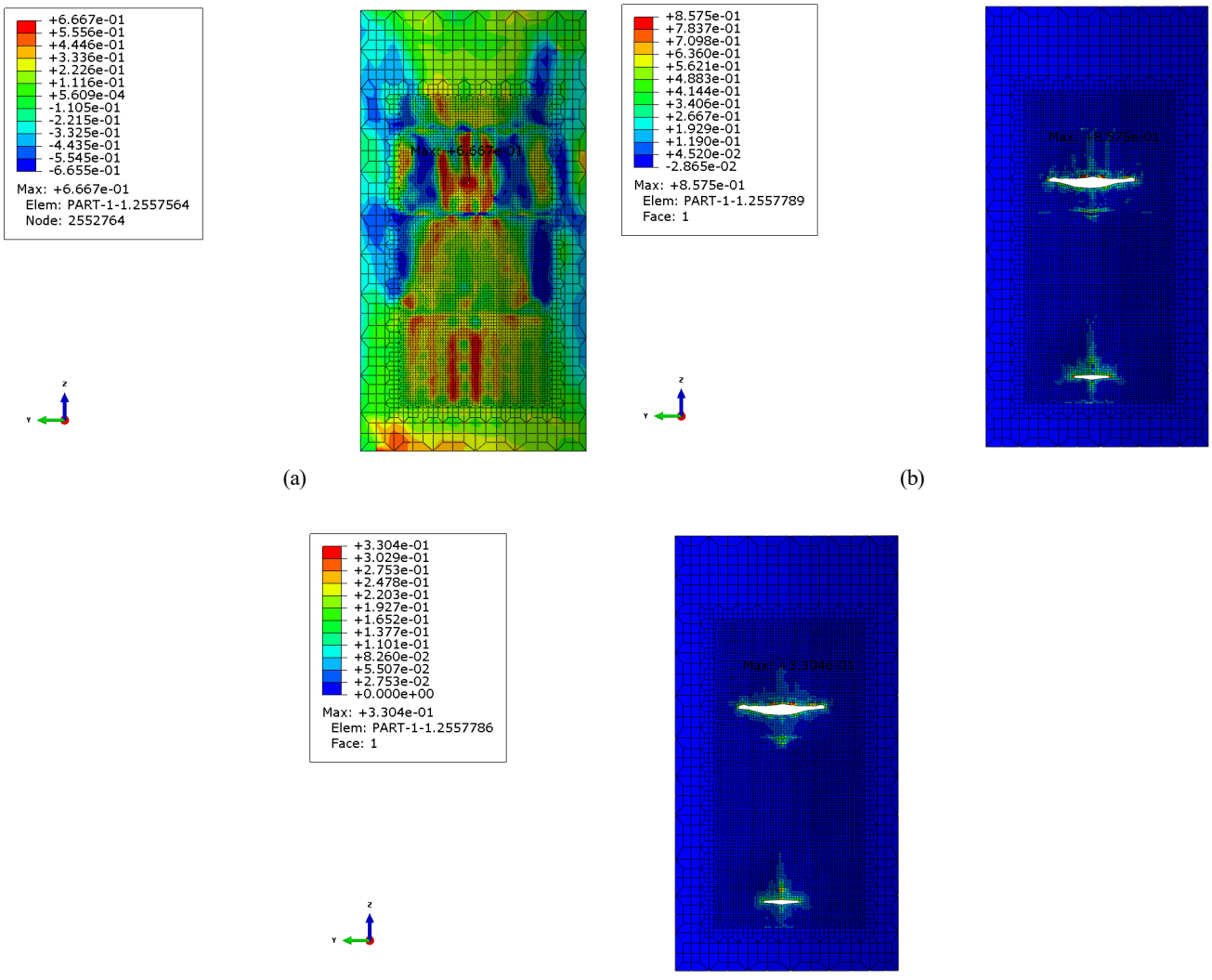

Fig. 13 Stress triaxiality, LN necking indicator and HC damage indicator of Case3-2; (a) Stress triaxiality; (b) LN necking indicator; (c) HC damage indicator

application of hydroforces to reasonably determine the damage extents.

The effect of hydroforces on the damage extents from the collision was relatively limited. This was presumed to be due to the fact that the collision occurs in a very short instant. A comparison of the failure areas caused by the collision showed that the constant failure strain model predicted larger fractures by about 15% compared to the HC-LC model. Since the size of the failure determines the speed and amount of flooding, a more scientific and reasonable failure model was required for the FOWT's impact analysis. The analysis of stress triaxiality and damage indicators confirmed that the use of the HC-LN model was justified.

The pitch motion of the ship generated by the waves changes the direction and magnitude of the impact force and should be considered in the future. The impact of ship hydrodynamics on collision simulations needs to be considered in the future. The ability of moorings to constrain the FOWT needs to be evaluated, as modeling moorings requires special effort.

Conflict of Interest

Joonmo Choung serves as an editor in chief of the Journal of Ocean Engineering and Technology, but he had no role in the decision to publish this article. No potential conflict of interest relevant to this article was reported.

Funding

This research was supported by the Korea Energy Technology Evaluation and Planning funded by the Ministry of Trade, Industry and Energy of Korea (No. 20213000000030) and Korea Environmental Industry & Technology Institute funded by Korea Ministry of Environment (No. 146836).

References

Ansys. (2022). *Ansys User Manual*. Ansys.

Bela, A., Le Sourne, H., Buldgen, L., & Rigo, P. (2017). Ship collision analysis on offshore wind turbine monopile foundations. *Marine Structures*, *51*, 220–241. https://doi.org/10.1016/j.marstruc.2016.10.009

Borg, M., Mirzaei, M., & Brendmose, H. (2015). D1.2 Wind turbine models for the design. *DTU, Public LIFES50 D, 1.*

Cerik, B. C., & Choung, J. (2020). Ductile fracture behavior of mild and high-ytnsile strength shipbuilding steels. *Applied Sciences*, *10*(20), 7034. https://doi.org/10.3390/app10207034

Cerik, B. C., Ringsberg, J. W., & Choung, J. (2019). Revisiting MARSTRUCT benchmark study on side-shell collision with a combined localized necking and stress-state dependent ductile fracture model. *Ocean Engineering*, *187*, 106173. https://doi.org/10.1016/j.oceaneng.2019.106173

Dai, L., Ehlers, S., Rausand, M., & Utne, I. B. (2013). Risk of collision between service vessels and offshore wind turbines. *Reliability Engineering & System Safety*, *109*, 18–31. https://doi.org/10.1016/j.ress.2012.07.008

Det Norske Veritas (DNV). (2013), *Design of offshore wind turbine structures* (DNV-OS-J101).

Echeverry, S., Márquez, L., Rigo, Ph., & Sourne, H. L. (2019). Numerical crashworthiness analysis of a spar floating offshore wind turbine impacted by a ship. In C. Guedes Soares (Ed.), *Developments in the collision and grounding of ships and offshore structures* (1st ed.), 85–95. CRC Press. https://doi.org/10.1201/9781003002420-11

Han, D. H. (2022). *Development of a fluid-structure interaction technique for marine structures using non-viscous hydro-forces and explicit finite element method* [Doctoral dissertation, Inha University]. https://inha.dcollection.net/public_resource/pdf/200000598213_20230605182419.pdf

Jasmina,O. M. (2023, April 27). *Cargo ship strikes turbine at Orsted's Gode Wind 1 offshore wind farm, suffers massive damage.* Offshore Energy. https://www.offshore-energy.biz/cargo-ship-strikes-orsteds-gode-wind-1-offshore-wind-farm-suffers-massive-damage/

Jonkman, J. M. (2007). *Dynamics modeling and loads analysis of an offshore floating wind turbine* (NREL/TP-500-41958, 921803). https://doi.org/10.2172/921803

LSTC. (2023). *LSDYNA Manuals*. https://lsdyna.ansys.com/manuals/

Márquez, L., Le Sourne, H., & Rigo, P. (2022). Mechanical model for the analysis of ship collisions against reinforced concrete floaters of offshore wind turbines. *Ocean Engineering*, *261*, 111987. https://doi.org/10.1016/j.oceaneng.2022.111987

Masciola, M., Jonkman, J., & Robertson, A. (2013). *Implementation of a multisegmented, quasi-static cable model* (ISOPE-I-13-127).

Mohr, D., & Marcadet, S. J. (2015). Micromechanically-motivated phenomenological Hosford–Coulomb model for predicting ductile fracture initiation at low stress triaxialities. *International Journal of Solids and Structures*, *67–68*, 40–55. https://doi.org/10.1016/j.ijsolstr.2015.02.024

Moulas, D., Shafiee, M., & Mehmanparast, A. (2017). Damage analysis of ship collisions with offshore wind turbine foundations. *Ocean Engineering*, *143*, 149–162. https://doi.org/10.1016/j.oceaneng.2017.04.050

Pack, K., & Mohr, D. (2017). Combined necking & fracture model to predict ductile failure with shell finite elements. *Engineering Fracture Mechanics*, *182*, 32–51. https://doi.org/10.1016/j.engfracmech.2017.06.025

Park, S.-J., Cerik, B. C., & Choung, J. (2020). Comparative study on ductile fracture prediction of high-tensile strength marine structural steels. *Ships and Offshore Structures*, *15*(sup1), S208–S219. https://doi.org/10.1080/17445302.2020.1743552

Simulia. (2021). *Abaqus user manual*. Dassault Systemes Simulia Corp.

Sung, J. H., Kim, J. H., & Wagoner, R. H. (2010). A plastic constitutive equation incorporating strain, strain-rate, and temperature.

International Journal of Plasticity, *26*(12), 1746−1771. https://doi.org/10.1016/j.ijplas.2010.02.005

Yoon, D. H., Jeong, S. -Y., & Choung, J. (2023). Collision simulations between an icebreaker and an iceberg considering ship hydrodynamics. *Ocean Engineering*, *279*, 114333. https://doi.org/10.1016/j.oceaneng.2023.114333

Zhang, Y., & Hu, Z. (2022). An aero-hydro coupled method for investigating ship collision against a floating offshore wind turbine. *Marine Structures*, *83*, 103177. https://doi.org/10.1016/j.marstruc.2022.103177

Author ORCIDs

Author name	ORCID
Yoon, Dong Ho	0000-0003-0602-4006
Choung, Joonmo	0000-0003-1407-9031

KSOE

Journal of Ocean Engineering and Technology 37(3), 122-128, June, 2023
https://doi.org/10.26748/KSOE.2023.013

pISSN 1225-0767
eISSN 2287-6715

Original Research Article

Trajectory Optimization for Autonomous Berthing of a Twin-Propeller Twin-Rudder Ship

Changyu Lee[1] and Jinwhan Kim[2]

[1]*Graduate Student, Department of Mechanical Engineering, KAIST, Daejeon, Korea*
[2]*Professor, Department of Mechanical Engineering, KAIST, Daejeon, Korea*

KEYWORDS: Two-point boundary value problem, Trajectory planning, Autonomous berthing, Twin-propeller twin-rudder ship, Model predictive control

ABSTRACT: *Autonomous berthing is a crucial technology for autonomous ships, requiring optimal trajectory planning to prevent collisions and minimize time and control efforts. This paper presents a two-phase, two-point boundary value problem (TPBVP) strategy for creating an optimal berthing trajectory for a twin-propeller, twin-rudder ship with autonomous berthing capabilities. The process is divided into two phases: the approach and the terminal. Tunnel thruster use is limited during the approach but fully employed during the terminal phase. This strategy permits concurrent optimization of the total trajectory duration, individual phase trajectories, and phase transition time. The efficacy of the proposed method is validated through two simulations. The first explores a scenario with phase transition, and the second generates a trajectory relying solely on the approach phase. The results affirm our algorithm's effectiveness in deciding transition necessity, identifying optimal transition timing, and optimizing the trajectory accordingly. The proposed two-phase TPBVP approach holds significant implications for advancements in autonomous ship navigation, enhancing safety and efficiency in berthing operations.*

1. Introduction

Recently, as interest in autonomous ships grows, autonomous berthing has garnered attention as a crucial technology for enabling fully autonomous ship navigation. Conventionally, larger ships depend on tugboat assistance for berthing instead of conducting the process independently (Quan et al., 2019). However, in pursuit of the ultimate goal of achieving full autonomy in ship navigation, automation of the berthing process is essential.

Effective berthing requires plotting a path that moves the ship from its current position to the intended berthing point. This procedure calls for trajectory planning over simple path planning, to ensure smoother movement, increased efficiency, and adept handling of constraints. Previous research proposed berthing algorithms for ships equipped with azimuth thrusters using optimal control (Martinsen et al., 2019, 2022), as well as path optimization methods for single-rudder, single-propeller ships with two side thrusters while considering real port spatial constraints (Miyauchi et al., 2022). To tackle the universal challenge of finding a globally optimal solution in optimization-based methods, graph search (Ødven et al., 2022) and warm-started semi-online trajectory planners (Rachman et al., 2022) have been utilized. Most recently, experimental verification of the miiliampere ship's docking algorithm - an urban ferry with two azimuth thrusters - was conducted using MPC-based trajectory optimization and trajectory tracking controllers (Bitar et al., 2020; Bitar et al., 2021; Martinsen et al., 2020).

In this study, we propose a berthing trajectory generation algorithm for twin-propeller, twin-rudder ships with self-berthing capabilities. It is challenging to anticipate effective force when a pair of propellers and rudders are rotated in reverse (Lindegaard and Fossen, 2003; Skjetne et al., 2004). Additionally, tunnel thrusters only show effectiveness at low speeds (Fossen, 2011). Addressing these motion characteristics, we adopt a two-phase, two-point boundary value problem approach, segmenting the process into an approaching phase—where the ship maneuvers close to the target berthing position—and a terminal phase, continuing until the ship aligns with its final position. In the approaching phase, the use of the tunnel thruster is limited, whereas in the terminal phase, it is actively deployed. We conducted numerical simulations to validate the proposed trajectory generation algorithm's efficacy, highlighting its successful application in

Received 16 May 2023, revised 12 June 2023, accepted 14 June 2023
Corresponding author Jinwhan Kim: +82-42-350-1519, jinwhan@kaist.ac.kr

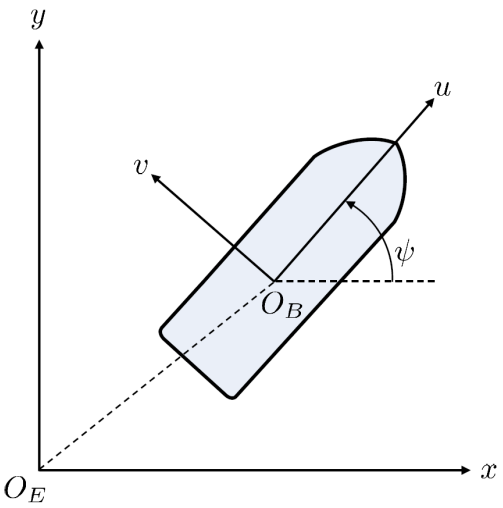

Fig. 1 The coordinate system of a ship

autonomous berthing scenarios.

The structure of this paper is as follows: Section 2 introduces the necessary preliminaries, providing the groundwork for understanding the subsequent methodologies. The formulation of our proposed trajectory optimization scheme is presented in detail in Section 3. In Section 4, we provide a comprehensive review of the simulation results, demonstrating the efficacy of our approach. Finally, we draw conclusions from our findings in Section 5, encapsulating the key points of the study and their implications for autonomous ship berthing.

2. Preliminary

2.1 Ship Dynamic Model

The equations of motion of a ship are composed of both kinematic and kinetic equations, represented in the earth-fixed and body-fixed coordinate systems, as illustrated in Fig. 1. The kinematic equations, which deal with the geometric properties of motion, are defined within the context of the earth-fixed frame. Conversely, the kinetic equations are modeled within the body-fixed coordinate system. The relationship between these two coordinate systems is articulated through the ship's heading ψ as follows:

$$\dot{\eta} = J(\psi)\nu,$$

$$J(\psi) = \begin{bmatrix} \cos\psi & -\sin\psi & 0 \\ \sin\psi & \cos\psi & 0 \\ 0 & 0 & 1 \end{bmatrix} \tag{1}$$

where $\eta = [x, y, \psi]^\top$ and $\nu = [u, v, r]^\top$ are the position and velocity vectors, respectively, and $J(\psi)$ is the rotation matrix that transforms the velocities from the body-fixed coordinate to the earth-fixed coordinate.

The kinetic equations represent the relationship between the forces acting on the vehicle and its motion within the body-fixed frame. These equations can be articulated using Newton's second law, as follows:

$$M\dot{\nu} + C(\nu)\nu + D(\nu)\nu = \tau \tag{2}$$

In this equation, M represents the inertia matrix, $C(\nu)$ stands for the Coriolis and centripetal matrix, $D(\nu)$ signifies the damping matrix, and τ is the vector of control force. The matrices M and $C(\nu)$ can be depicted as the sum of the rigid body and added mass components, as outlined below:

$$M = M_{RB+}M_A$$

$$M_{RB} = \begin{bmatrix} m & 0 & 0 \\ 0 & m & mx_g \\ 0 & mx_g & I_z \end{bmatrix}$$

$$M_A = \begin{bmatrix} -X_{\dot{u}} & 0 & 0 \\ 0 & -Y_{\dot{v}} & -Y_{\dot{r}} \\ 0 & -N_{\dot{v}} & -N_{\dot{r}} \end{bmatrix} \tag{3}$$

$$C(\nu) = C_{RB}(\nu) + C_A(\nu),$$

$$C_{RB}(\nu) = \begin{bmatrix} 0 & 0 & -m(x_g r + v) \\ 0 & 0 & mu \\ m(x_g r + v) & -mu & 0 \end{bmatrix}$$

$$C_A(\nu) = \begin{bmatrix} 0 & 0 & Y_{\dot{v}}\nu + Y_{\dot{r}} r \\ 0 & 0 & -X_{\dot{u}} u \\ -Y_{\dot{v}}\nu - Y_{\dot{r}} r & X_{\dot{u}} u & 0 \end{bmatrix}$$

Additionally, $D(\nu)$ can be depicted by a combination of the nonlinear and linear damping matrices, as follows:

$$D(\nu) = D_l(\nu) + D_n(\nu),$$

$$D_l(\nu) = -\begin{bmatrix} X_u & 0 & 0 \\ 0 & Y_v & Y_r \\ 0 & N_v & N_r \end{bmatrix} \tag{4}$$

$$D_n(\nu) = -\begin{bmatrix} X_{|u|u}|u| & 0 & 0 \\ 0 & Y_{|v|v}|v| + Y_{|r|v}|r| & Y_{|v|r}|v| + Y_{|r|r}|r| \\ 0 & N_{|v|v}|v| + N_{|r|v}|r| & N_{|v|r}|v| + N_{|r|r}|r| \end{bmatrix}$$

2.2 Actuator Model

In this study, as illustrated in Fig. 2, we develop an algorithm for a ship equipped with twin propellers and twin rudders at the stern, in addition to a bow tunnel thruster. The forces generated are as follows: T_1 represents the force produced by the port stern propeller, T_2 corresponds to the force originating from the stern starboard propeller, while T_3 designates the bow tunnel propeller forces. Additionally, the rudder angles at the port and starboard sides are denoted by δ_1 and δ_2, respectively. Given these, the control force can be formulated with the

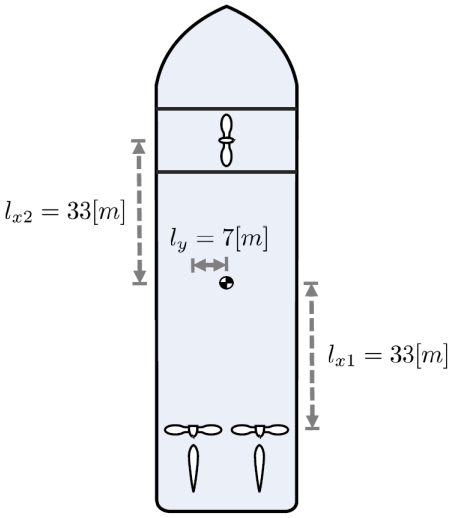

Fig. 2 The control configuration of a ship

control input $[T_1, T_2, \delta_1, \delta_2, T_3]^\top$, as detailed below:

$$\tau_c = g(u) = \begin{bmatrix} T_1 + T_2 - D_1 - D_2 \\ L_1 + L_2 + T_3 \\ (D_1 - T_1 - D_2 + T_2)l_y - (L_1 + L_2)l_{x1} + T_3 l_{x2} \end{bmatrix} \tag{5}$$

In this formulation, D_1 and D_2 represent the drag forces, while L_1 and L_2 represent the lift forces for the port and starboard rudder, respectively. The terms l_{x_1}, l_{x_2} and l_y refer to the distances from the center of gravity to each propeller. The force generated by the propeller can be defined by the rotational speed n_i, and the thruster coefficient K_T with advance ratio J_i, as follows:

$$T_i = K_T(J_i)\rho |n_i| n_i D^4, \quad i = 1,2 \tag{6}$$

where ρ denotes the density of water and D stands for the propeller's diameter. The tunnel thruster is also modeled using the rotational speed n_3, the propeller's diameter D_3, and the thruster coefficient K_{T_3}. However, it is important to note that the tunnel thruster can only generate sufficient force when the ship moves at low speeds. Consequently, we employ the tunnel thruster at lower speeds and model it with a constant thruster coefficient, independent of the advance ratio, as follows:

$$T_3 = K_{T_3}\rho |n_3| n_3 D_3^4 \tag{7}$$

The force exerted by a ship's rudder at low speed is notably influenced by the direction of the propeller's rotation. When the propeller rotates forward, ample lift is generated through propeller force and rudder angle interplay. However, generating effective lift is challenging when the propeller rotates in reverse. Consequently, the lift and drag forces produced by a pair of propellers and rudders can be formulated as follows, according to (Lindegaard, 2003):

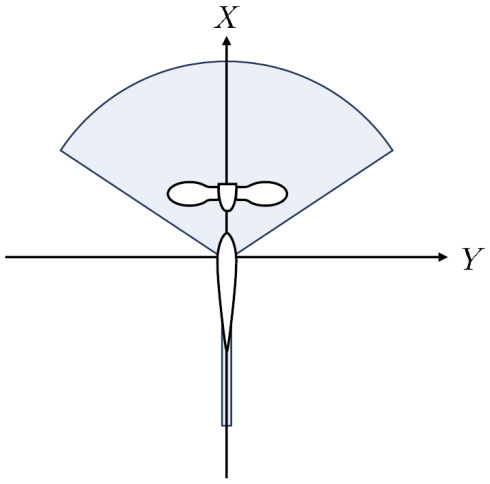

Fig. 3 The feasible force domain of single-propeller, single-rudder

$$L_i = \begin{cases} T_i k_{L\delta} \delta_i, & T_i \geq 0 \\ 0, & T_i < 0 \end{cases}, \; i = 1,2,$$

$$D_i = \begin{cases} T_i (k_{D\delta_1} |\delta_i| + k_{D\delta_2} \delta_i^2), & T_i \geq 0 \\ 0, & T_i < 0 \end{cases}, \; i = 1,2. \tag{8}$$

Fig. 3 visually illustrates the force generated by a pair of propellers and rudders. Given that the ship's propellers and rudders can operate independently, the ship is viewed as a fully-actuated system capable of controlling motion across three degrees of freedom. Nevertheless, when considering the propulsion properties of the propellers and rudders, as demonstrated in Eq. (8), the system exhibits specific characteristics of being partially under-actuated.

3. Berthing Trajectory Optimization

Given the initial and target berthing states, a trajectory optimization algorithm can be devised to minimize both the berthing duration and control effort, while taking into account the motion and control characteristics represented by Eqs. (1)-(8). However, the nonlinear nature and complexity of the optimization problem present a challenge in assuring optimal solutions. To tackle this issue, we propose an optimization approach that separates the trajectory into two distinct phases, thereby effectively reducing the complexity of the problem.

3.1 Two-phase Approach

The berthing process can be strategically segmented into two phases. The first, referred to as the "approaching phase," guides the ship towards a region proximate to the final berthing position. The second, termed the "terminal phase," involves the precise maneuvering of the ship to reach the final position. During the approaching phase, the ship retains sufficient speed, thus hindering the bow tunnel propeller from generating effective force. As a result, in this phase, only the stern propellers and rudders are employed as control inputs, as described below:

$$u_a = [T_1, T_2, \delta_1, \delta_2, 0]^\top \tag{9}$$

Conversely, the terminal phase occurs at relatively lower speeds, thus allowing the use of the tunnel thruster. In this phase, the ship's movements and rotations are slower, diminishing the effects of the Coriolis and nonlinear damping matrices. This reduction permits a simplified model approximation similar to those used in dynamic positioning (Skjetne et al., 2004). Accordingly, the dynamic model and control input vectors are formulated as follows:

$$M\dot{\nu} + D_l(\nu)\nu = \tau_c,$$

$$u_t = [T_1, T_2, \delta_1, \delta_2, T_3]^\top \tag{10}$$

3.2 Two-point Boundary Value Problem

Employing models for each phase allows for the formulation of the two-point boundary value problem with the state vector $x = [x, y, \psi, u, v, r]^\top$, as detailed below:

$$\min_{x(\cdot),u(\cdot)} J_T + \int_0^{T_{f1}} J_a(t)dt + J_a^{T_{f1}} + \int_{T_{f1}}^{T_{f2}} J_t(t)dt \tag{11}$$

Here T_{f1} and $(T_{f2} - T_{f1})$ represent the time durations for each phase, respectively. Additionally, J_T denotes the time penalty cost function, which is defined as follows:

$$J_T(t) = \rho_t(T_{f1} + T_{f2}) \tag{12}$$

Here ρ_t is the weighting scalar. $J_a(t)$, $J_a^{T_{f1}}$ represent the cost functions for the approaching, which are defined as follows:

$$J_a(t) = \nu(t)^\top Q_a \nu(t) + u_a(t)^\top P_a u_a(t) + \dot{u}_a(t)^\top R_a \dot{u}_a(t)$$

$$J_a^{T_{f1}} = (\eta(T_{f1}) - \eta_f)^\top Q_a^{T_{f1}} (\eta(T_{f1}) - \eta_f) \tag{13}$$

In these equations, the matrices Q_a, P_a, and R_a denote the weight matrices that penalize the velocity, control input, and rate of change of control input, respectively. $Q_a^{T_{f1}}$ represents the weight matrix that penalizes the terminal position of the approaching phase, while η_f is the final position vector. Additionally, $J_t(t)$ denotes the cost function for the terminal phase, given as follows:

$$J_t(t) = \nu(t)^\top Q_t \nu(t) + u_t(t)^\top P_t u_t(t) + \dot{u}_t(t)^\top R_t \dot{u}_t(t) \tag{14}$$

In this context, the matrices Q_t, P_t, and R_t represent the weight matrices that penalize the velocity, control input, and rate of change of control input, respectively. The optimization problem formulated above also encompasses several constraints, which are as follows:

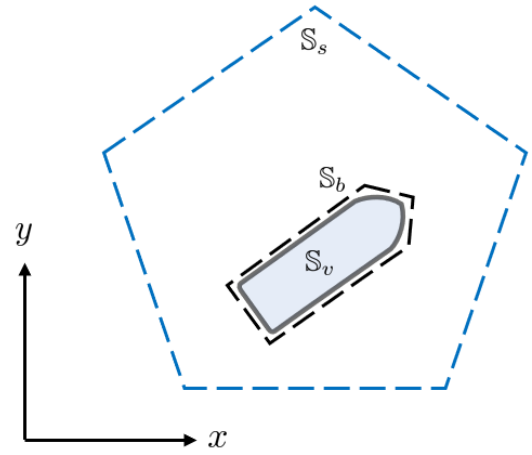

Fig. 4 The illustration of collision avoidance constraints. (Ship $\mathbb{S}_v$ with a safety boundary $\mathbb{S}_b$, as well as state constraints $\mathbb{S}_s$)

$$\dot{x}(t) = f_a(x(t), u_a(t)), \forall t \in [0, T_{f1}]$$

$$\dot{x}(t) = f_t(x(t), u_t(t)), \forall t \in [T_{f1}, T_{f2}]$$

$$x(0) = x_0$$

$$x(T_{f2}) = x_f \tag{15}$$

$$|u(t)| \leq \overline{u(t)}, \forall t \in [0, T_{f2}]$$

$$\mathbb{S}_b \subseteq \mathbb{S}_s$$

Here f_a and f_t represent the dynamic models of the approaching and terminal phases, respectively, while x_0 and x_f denote the initial and target berthing states. $\overline{(\bullet)}$ denotes the maximum value. The final constraints represent the collision avoidance condition. Here, $\mathbb{S}_b$ and $\mathbb{S}_s$ indicate the safety boundary of the ship and state constraints, as shown in Fig. 4.

To address the nonlinear optimization problem formulated in this manner, we utilized the Interior Point Optimizer (IPOPT) (Wächter and Biegler, 2006), implemented in the CasADI framework (Andersson et al., 2019), within the in the MATLAB environment.

4. Simulation Results

Simulations were executed within the MATLAB environment to evaluate the effectiveness of the proposed trajectory optimization algorithm. We incorporated the port geometry of Jangsaengpo Port in Ulsan, Korea, and devised two scenarios featuring distinct initial and final positions. The state constraints were formulated convexly, considering the berthing position, the port layout, and the ship's navigable area. It is worth noting that the specific configuration of these constraints can be altered based on the available space in the intended target port. The parameters of the supply ship's model used for simulation are derived from (Skjetne et al., 2004), with the

remaining parameters detailed in Table 1. The parameters specific to our proposed algorithm can be found in Table 2. The results of the first simulation are visually represented in Figs. 5-7.

Table 1 The model parameters of the ship

Parameter	Value
$k_{D\delta_1}$	0.093
$k_{D\delta_2}$	0.727
$k_{L\delta}$	0.920
l_{x_1} (m)	-33
l_{x_2} (m)	33
l_y (m)	7

Table 2 Parameters of the trajectory optimization problem

Parameter	Value
ρ_t	30
Q_a	diag ([0.0, 0.0, 1.0E6])
P_a	diag ([0.1, 0.1, 1.0, 1.0, 0.1])
R_a	diag ([1.0, 1.0, 1.0, 1.0, 1.0])
$Q_a^{T_{\Pi}}$	diag ([1.0, 1.0, 5.0E4])
Q_t	diag ([1.0E2, 0.0, 0.0])
P_t	diag ([0.0, 0.0, 1.0, 1.0, 0.0])
R_t	diag ([0.01, 0.01, 1.0, 1.0, 0.01])
$\overline{T_1}$, $\overline{T_2}$ (kN)	200
$\overline{R_1}$, $\overline{R_2}$ (deg)	30
$\overline{T_3}$ (kN)	100

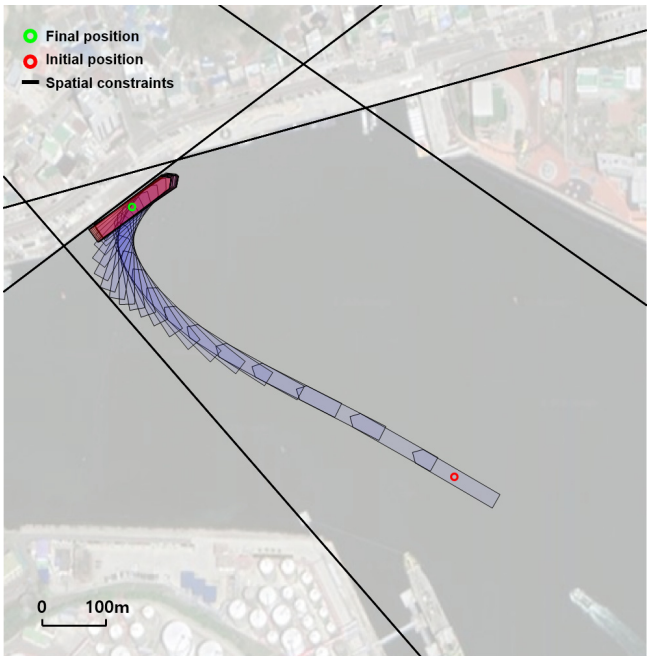

Fig. 5 The result of the first scenario

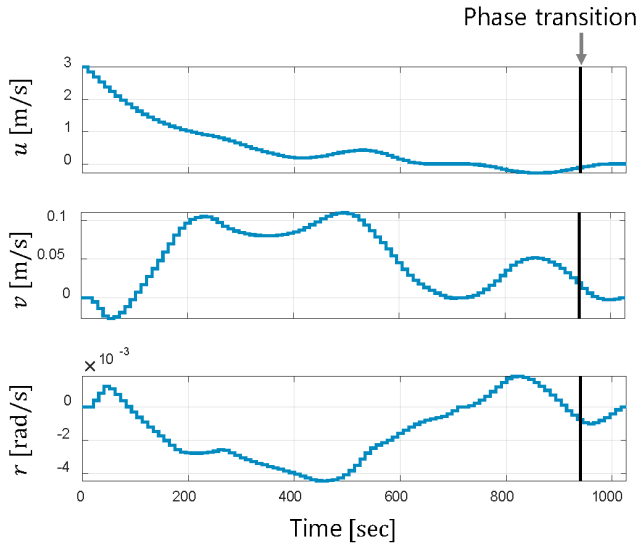

Fig. 6 Time trajectories of velocities (first scenario)

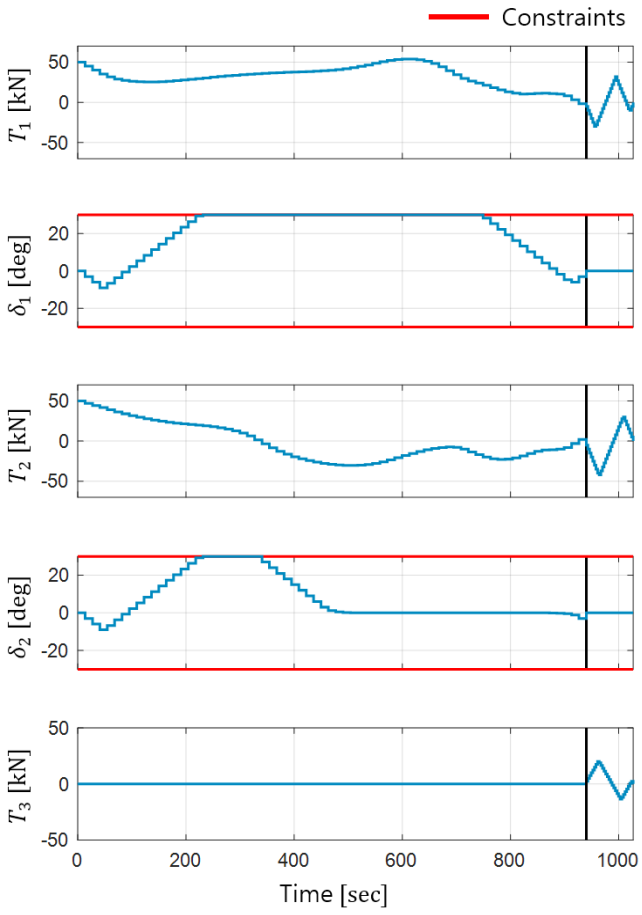

Fig. 7 Time trajectories of control inputs (first scenario)

Fig. 5 illustrates the time trajectory for a port side berthing scenario. In this figure, the blue ship trajectory corresponds to the approaching phase, while the red ship trajectory represents the terminal phase. Fig. 6 illustrates the variation in velocities over the course of the berthing process, which lasts approximately 1026 seconds, with the approaching phase accounting for 940 seconds of this duration. This

highlights a distinct phase switch. Fig. 7 shows the alterations in control input over time. These results corroborate that the proposed algorithm effectively considers the characteristic of not utilizing a rudder when the propeller is in reverse rotation.

In the second scenario, the objective is to berth a ship on the starboard side. The results of this simulation are depicted in Figs. 8-10. Fig. 8 displays the time trajectories for each phase. Figs. 9 and 10, on the other hand, portray the velocities and control input fluctuations over time, respectively. Contrary to the first scenario, the second scenario does not require a phase transition. This result arises from the optimization process determining that a sole emphasis on the approaching phase, without a phase transition, is more efficient for this scenario.

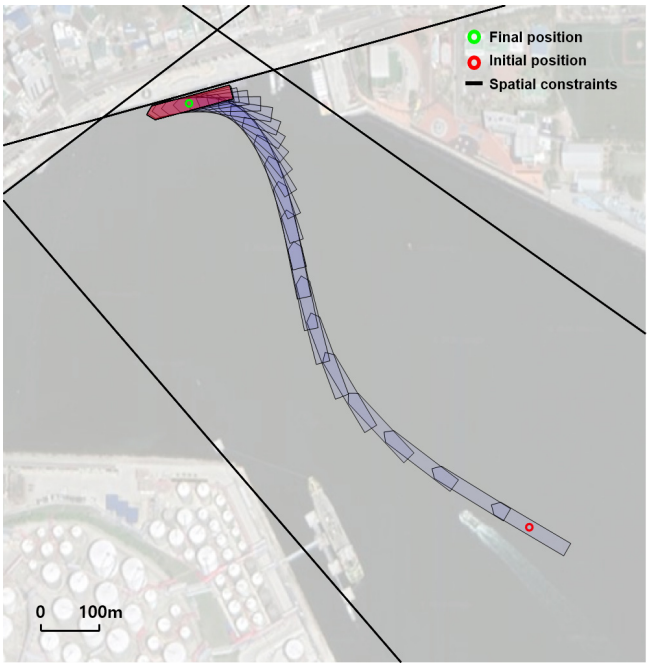

Fig. 8 The result of the second scenario

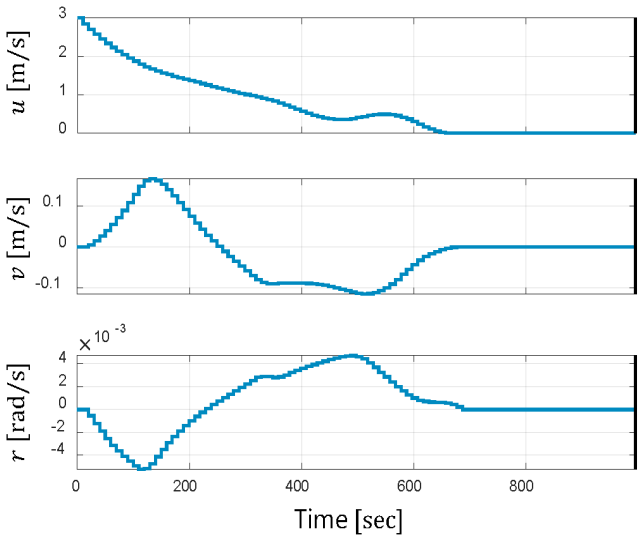

Fig. 9 Time trajectories of velocities (second scenario)

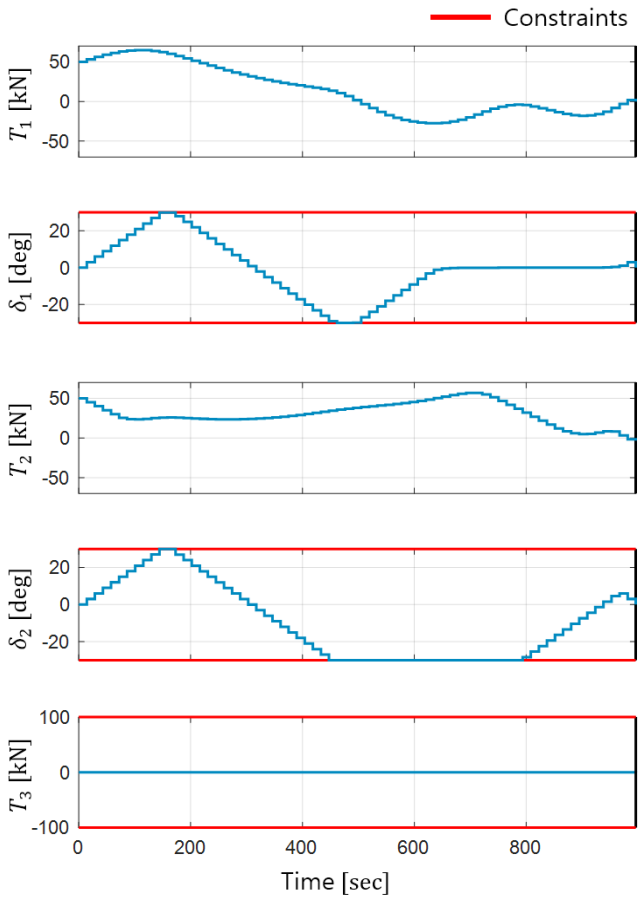

Fig. 10 Time trajectories of control inputs (second scenario)

5. Conclusions

In this study, we have proposed a two-phase berthing trajectory optimization algorithm for the autonomous berthing of a twin-propeller, twin-rudder ship. The berthing process was segregated into two distinct phases, taking into account the ship's dynamic characteristics and actuator properties. We formulated models for each phase and generated dynamically feasible trajectories using a two-phase, two-point boundary value problem. To assess the practicality and effectiveness of our proposed algorithm, we created two scenarios grounded in real-world port geometries and conducted comprehensive numerical simulations.

Conflict of Interest

Jinwhan Kim serves as a editorial board member of the Journal of Ocean Engineering and Technology, but he had no role in the decision to publish this article. No potential conflict of interest relevant to this article was reported.

Funding

This research was supported by a grant from the National R&D Project "Development of an electric-powered car ferry and a

roll-on/roll-off power supply system" funded by the Ministry of Oceans and Fisheries, Korea (Grant No. PMS4420).

References

Andersson, J. A. E., Gillis, J., Horn, G., Rawlings, J. B., & Diehl, M. (2019). CasADi: A software framework for nonlinear optimization and optimal control. *Mathematical Programming Computation*, *11*(1), Article 1. https://doi.org/10.1007/s12532-018-0139-4

Bitar, G., Eriksen, B.-O. H., Lekkas, A. M., & Breivik, M. (2021). Three-Phase Automatic Crossing for a Passenger Ferry With Field Trials. *2021 European Control Conference (ECC)*, 2271–2277. https://doi.org/10.23919/ECC54610.2021.9655139

Bitar, G., Martinsen, A. B., Lekkas, A. M., & Breivik, M. (2020). Trajectory Planning and Control for Automatic Docking of ASVs with Full-Scale Experiments∗∗This work is supported by the Research Council of Norway through the project number 269116 as well as through the Centres of Excellence funding scheme with project number 223254. *IFAC-PapersOnLine*, *53*(2), 14488–14494. https://doi.org/10.1016/j.ifacol.2020.12.1451

Fossen, T. I. (2011). *Handbook of Marine Craft Hydrodynamics and Motion Control*. John Wiley & Sons.

Lindegaard, K.-P. (2003). *Acceleration feedback in dynamic positioning*.

Lindegaard, K.-P., & Fossen, T. I. (2003). Fuel-efficient rudder and propeller control allocation for marine craft: Experiments with a model ship. *IEEE Transactions on Control Systems Technology*, *11*(6), 850–862. https://doi.org/10.1109/TCST.2003.815613

Martinsen, A. B., Bitar, G., Lekkas, A. M., & Gros, S. (2020). Optimization-Based Automatic Docking and Berthing of ASVs Using Exteroceptive Sensors: Theory and Experiments. *IEEE Access*, *8*, 204974–204986. https://doi.org/10.1109/ACCESS.2020.3037171

Martinsen, A. B., Lekkas, A. M., & Gros, S. (2019). Autonomous docking using direct optimal control. *IFAC-PapersOnLine*, *52*(21), Article 21.

Martinsen, A. B., Lekkas, A. M., & Gros, S. (2022). Optimal Model-Based Trajectory Planning With Static Polygonal Constraints. *IEEE Transactions on Control Systems Technology*, *30*(3), Article 3. https://doi.org/10.1109/TCST.2021.3094617

Miyauchi, Y., Sawada, R., Akimoto, Y., Umeda, N., & Maki, A. (2022). Optimization on planning of trajectory and control of autonomous berthing and unberthing for the realistic port geometry. *Ocean Engineering*, *245*, 110390. https://doi.org/10.1016/j.oceaneng.2021.110390

Ødven, P. K., Martinsen, A. B., & Lekkas, A. M. (2022). Static and dynamic multi-obstacle avoidance and docking of ASVs using computational geometry and numerical optimal control. *IFAC-PapersOnLine*, *55*(31), Article 31. https://doi.org/10.1016/j.ifacol.2022.10.408

Quan, T. D., Suh, J.-H., & Kim, Y.-B. (2019). Leader-Following Control System Design for a Towed Vessel by Tugboat. *Journal of Ocean Engineering and Technology*, *33*(5), 462–469. https://doi.org/10.26748/KSOE.2019.075

Rachman, D. M., Maki, A., Miyauchi, Y., & Umeda, N. (2022). Warm-started semionline trajectory planner for ship's automatic docking (berthing). *Ocean Engineering*, *252*, 111127. https://doi.org/10.1016/j.oceaneng.2022.111127

Skjetne, R., Smogeli, Ø. N., & Fossen, T. I. (2004). A Nonlinear Ship Manoeuvering Model: Identification and adaptive control with experiments for a model ship. *Modeling, Identification and Control: A Norwegian Research Bulletin*, *25*(1), 3–27. https://doi.org/10.4173/mic.2004.1.1

Wächter, A., & Biegler, L. T. (2006). On the implementation of an interior-point filter line-search algorithm for large-scale nonlinear programming. *Mathematical Programming*, *106*(1), 25–57. https://doi.org/10.1007/s10107-004-0559-y

Author ORCIDs

Author name	ORCID
Lee, Changyu	0000-0003-1964-9101
Kim, Jinwhan	0000-0001-6886-2449

Instructions for Authors

General information

To submit a manuscript to the Journal of Ocean Engineering and Technology (JOET), it is advised to first carefully read the aims and the scope section of this journal, as it provides information on the editorial policy and the category of papers it accepts. Unlike many regular journals, JOET usually has no lag in acceptance of a manuscript and its publication. Authors that find a match with the aims and the scope of JOET are encouraged to submit as we publish works from all over the world. JOET adheres completely to guidelines and best practices published by professional organizations, including Principles of Transparency and Best Practice in Scholarly Publishing (joint statement by COPE, DOAJ, WAME, and OASPA (http://doaj.org/bestpractice) if otherwise not described below. As such, JOET would like to keep the principles and policies of those professional organizations during editing and the publication process.

Research and publication ethics

Details on publication ethics are found in http://joet.org/authors/ethics.php. For the policies on research and publication ethics not stated in the Instructions, Guidelines on Good Publication (http://publicationethics.org/) can be applied.

Requirement for membership

One of the authors who submits a paper or papers should be member of the Korean Society of Ocean Engineers (KSOE), except a case that editorial board provides special admission of submission.

Publication type

Article types include scholarly monographs (original research articles), technical articles (technical reports and data), and review articles. The paper should have not been submitted to other academic journal. When part or whole of a manuscript was already published to conference papers, research reports, and dissertations, then the corresponding author should note it clearly in the manuscript.

Copyright

After published to JOET, the copyright of manuscripts should belong to KSOE. A transfer of copyright (publishing agreement) form can be found in submission website (http://www.joet.org).

Manuscript submission

Manuscript should be submitted through the on-line submission website (http://www.joet.org). The date that manuscript was received through on-line website is the official date of receipt. Other correspondences can be sent by an email to the Editor in Chief or secretariat. The manuscript must be accompanied by a signed statement that it has been neither published nor currently submitted for publication elsewhere. The manuscript should be written in English or Korean. Ensure that online submission are in a standard word processing format. Corresponding author must write the manuscript using the JOET template provided in Hangul or MS Word format. Ensure that graphics are high-resolution. Be sure all necessary files have been uploaded/ attached.

Authors' checklist

Please refer to “Authors' Checklist” for details.

Article structure

Manuscript must be edited in the following order: (1) Title, (2) Authors' names and affiliations, (3) Keywords, (4) Abstract, (5) Nomenclature (optional), (6) Introduction, (7) Main body (analyses, tests, results, and discussions), (8) Conclusions, (9) Conflict of interest, (10) Funding (optional), (11) Acknowledgements (optional), (12) References, (13) Appendices (optional), (14) Author’s ORCIDs.

Abstract

A concise and factual abstract is required. The abstract should state briefly the background, purpose and methods of the research, the principal results and conclusions. An abstract should be written in 150-200 words. References are not cited in abstract whenever possible. Also, non-standard or uncommon abbreviations should be avoided, but if essential they must be defined at their first mention in the abstract itself.

Keywords

Immediately after the abstract, provide a maximum of 5 or 6 keywords.

Unit

Use the international system units(SI). If other units are mentioned, please give their equivalent in SI.

Equations

All mathematical equations should be c1early printed/typed using well accepted explanation. Superscripts and subscripts should be typed clearly above or below the base line. Equation numbers should be given in Arabic numerals enclosed in parentheses on the right-hand margin.

Tables

Tables should be numbered consecutively with Arabic numerals. Each table should be fully titled. All tables should be referred to in the texts.

Figures

Figures should be numbered consecutively with Arabic numerals. Each figure should be fully titled. All figures should be referred to in the texts. All the illustrations should be of high quality meeting with the publishing requirement with legible symbols and legends.

Conflict of interest

It should be disclosed here according to the statement in the Research and publication ethics regardless of existence of conflict of interest. If the authors have nothing to disclose, please state: “No potential

conflict of interest relevant to this article was reported."

Funding

Funding to the research should be provided here. Providing a FundRef ID is recommended including the name of the funding agency, country and if available, the number of the grant provided by the funding agency. If the funding agency does not have a FundRef ID, please ask that agency to contact the FundRef registry (e-mail: fundref.registry@crossref.org). Additional detailed policy of FundRef description is available from http://www.crossref.org/fundref/. Example of a funding description is as follows:

The study is supported by the Inha University research fund (FundRef ID: 10.13039/501100002632), and the Korea Health Personnel Licensing Examination Institute research fund (FundRef ID: 10.13039/501100003647).

Acknowledgments

Any persons that contributed to the study or the manuscript, but not meeting the requirements of an authorship could be placed here. For mentioning any persons or any organizations in this section, there should be a written permission from them.

References in text

References in texts follow the APA style. Authors can also see how references appear in manuscript text through the 'Template'.

Reference list

Reference list follows the APA style. Authors can see how references should be given in reference section through the 'Template'.

Appendices

The appendix is an optional section that can contain details and data supplemental to the main text. If there is more than an appendix, they should be identified as A, B, C, etc. Formulae and equations in appendices should be given separate numbering: Eq. (A1), Eq. (A2), etc.; in a subsequent appendix, Eq. (B1) and so on. Similarly for tables and figures: Table A1; Fig. A1, etc.

ORCID (Open Researcher and Contributor ID)

All authors are recommended to provide an ORCID. To obtain an ORCID, authors should register in the ORCID web site: http://orcid.org. Registration is free to every researcher in the world. Example of ORCID description is as follows:

Joonmo Choung: https://orcid.org/0000-0003-1407-9031

Peer review and publication process

The peer review process can be broadly summarized into three groups: author process, review process, and publishing process for accepted submissions. General scheme is presented in Figure 1.

Check-in process for review

If the manuscript does not fit the aims and scope of the Journal or does not adhere to the Instructions to Authors, it may be rejected immediately after receipt and without a review. Before reviewing, all submitted manuscripts are inspected by Similarity Check powered by iThenticate (https://www.crossref.org/services/similarity-check/), a plagiarism-screening tool. If a too high degree of similarity score is found, the Editorial Board will do a more profound content screening.

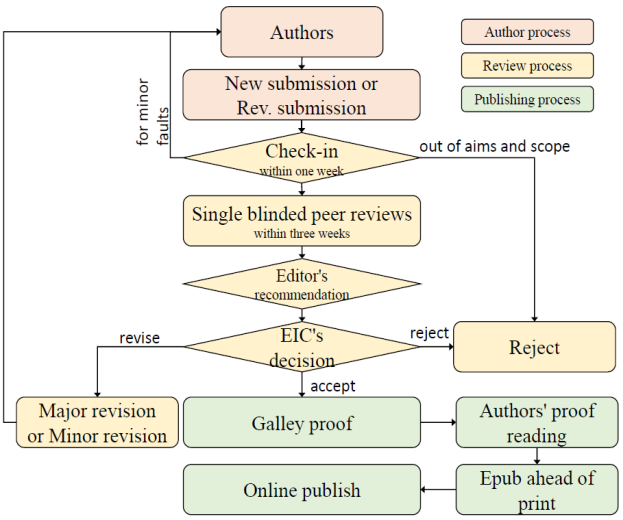

Figure 1 Flow chart of the peer review and publication process of JOET

The criterion for similarity rate for further screening is usually 15%; however, rather than the similarity rate, the Editorial Board focuses on cases where specific sentences or phrases are similar. The settings for Similarity Check screening are as follows: It excludes quotes, bibliography, small matches of 6 words, small sources of 1%, and the Methods section.

Number of reviewers

Reviewers will be selected from the list of reviewers. Manuscripts are then peer reviewed by at least 2 experts in the corresponding field, usually by 2.

Peer review process and the author response to the reviewer comments

JOET adopts single blind review, which means that the authors do not know the identity of the reviews. All papers, including those invited by the Editor, are subject to peer review.

The review period is 4 weeks. Usually the first decision is made within a week after completion of the review. The Editorial Board's decision after the review will be one of followings: Accept, Minor revision, Major revision, or Rejection. The Editorial Board may request the authors to revise the manuscript according to the reviewers' comments. If there are any requests for revision of the manuscript by the reviewers, the authors should do their best to revise the manuscript. If the reviewer's opinion is not acceptable or is believed to misinterpret the data, the author should reasonably indicate that. After revising the manuscript, the author should upload the revised files with a separate response sheet to each item of the reviewer's commentary. The author's revisions should be completed within 3 months after the request. If it is not received by the due date, the Editorial Board will notify the author. To extend the revision period beyond 3 months, the author should negotiate that with the Editorial Board. The manuscript review process can be provided for up two rounds. If the authors wish further review, the Editorial Board may consider it. The Editorial Board will make a final decision on the approval of the submitted manuscript for publication and can request any further corrections, revisions, and deletions of the article text if necessary. Statistical editing is also performed if the data requires professional statistical review by a statistician.

Processing after acceptance

If the manuscript is finally accepted, the galley proof will be sent to the corresponding author after professional manuscript editing and English proofreading. Proofreading should be performed for any misspellings or errors by the authors. Proofreading manuscript for publication is provided to the corresponding author, and the corresponding author must review the proofreading manuscript. Corresponding authors are responsible for the content of the proofreading manuscript and any errors. After final proofreading, the manuscript may appear at the journal homepage as an article in press with a unique DOI number for rapid communication. All published articles will be replaced by the replacement XML file and a final PDF.

Feedback after publication

If the authors or readers find any errors, or contents that should be revised, it can be requested from the Editorial Board. The Editorial Board may consider erratum, corrigendum or a retraction. If there are any revisions to the article, there will be a CrossMark description to announce the final draft. If there is a reader's opinion on the published article with the form of Letter to the editor, it will be forwarded to the authors. The authors can reply to the reader's letter. Letter to the editor and the author's reply may be also published.

How the journal handle complaints and appeals

The policy of JOET is primarily aimed at protecting the authors, reviewers, editors, and the publisher of the journal. If not described below, the process of handling complaints and appeals follows the guidelines of the Committee of Publication Ethics available from: https://publicationethics.org/appeals

- *Who complains or makes an appeal?*

Submitters, authors, reviewers, and readers may register complaints and appeals in a variety of cases as follows: falsification, fabrication, plagiarism, duplicate publication, authorship dispute, conflict of interest, ethical treatment of animals, informed consent, bias or unfair/inappropriate competitive acts, copyright, stolen data, defamation, and legal problem. If any individuals or institutions want to inform the cases, they can send a letter via the contact page on our website: https://www.joet.org/about/contact.php. For the complaints or appeals, concrete data with answers to all factual questions (who, when, where, what, how, why) should be provided.

- *Who is responsible to resolve and handle complaints and appeals?*

The Editorial Board or Editorial Office is responsible for them. A legal consultant or ethics editor may be able to help with the decision making.

- *What may be the consequence of remedy?*

It depends on the type or degree of misconduct. The consequence of resolution will follow the guidelines of the Committee of Publication Ethics (COPE).

Article processing charge

Payment due

Article processing charge (APC) covers the range of publishing services JOET provides. This includes provision of online tools for editors and authors, article production and hosting, and customer services. Upon editorial acceptance of an article for the regular review service and upon submission of an article for the fast review service, the corresponding author will be notified that payment is due.

APC

The APC up to 6 pages is ₩300,000 (or ＄300) and ₩650,000 (or ＄650) for the for the regular and fast review services, respectively. An extra APC of $100 per page is charged for papers longer than 6 pages, No taxes are included in this charge. For the fast review service, an advance fee of ₩250,000 ($250) should be paid on submission.

Payment methods

Credit card payment can be made online using a secure payment form as soon as the manuscript has been editorially accepted. We will we send a receipt by email once payment has been processed. Please note that payment by credit card carries a surcharge of 10% of the total APC.

Invoice payment is due within 7 days of the manuscript receiving editorial acceptance. Receipts are available on request.

JOET Template 2022.08.27

Journal of Ocean Engineering and Technology 00(0), 000-000, December, 2100
https://doi.org/10.26748/KSOE.2100.000
pISSN 1225-0767
eISSN 2287-6715

Original Research Article, Technical Article, Review Article, etc

Title of Article

Firstname Lastname[1], Firstname Lastname[2] and Firstname Lastname[3]

[1]*Professor, Department of OO, OO School, OO University, Busan, Korea*
[2]*Graduate Student, Department of OO, OO University, Seoul, Korea*
[3]*Senior Researcher, Department of OO, OO Engineering. Corp., Seoul, Korea*

KEYWORDS: Lumped mass line model, Explicit method, Steel lazy wave riser (Provide a maximum of 5 or 6 keywords.)

ABSTRACT:

Abstract Construction Guidelines
1) Describe the research background and aims in 1-2 sentences
2) Describe the research/analysis method (method section) in 2-3 sentences.
3) Describe the research/analysis results (results) in 2-3 sentences.
4) Describe the research conclusion in 1-2 sentences.
Abstract Editing Guidelines
1) Review English grammar.
2) Describe in 150-200 words.
3) When using an abbreviation or acronym, write the acronym after full words.
4) Abbreviations (acronyms) used only once should be written in full words only, and no acronyms.
5) References are not included in the abstract.

Nomenclature (Optional)

ITOC	Increment of total operating cost ($/yr)
LHV	Lower heating value (kJ/kg)
Pw	Power (kW)
T	Temperature (K)
V	Volume (m^3)
ρ	Density (kg/m^3)

1. Introduction

The introduction should briefly place the study in a broad context and highlight why it is important. It should define the purpose of the work and its significance. The current state of the research field should be reviewed carefully and key publications cited. Please highlight controversial and diverging hypotheses when necessary. Finally, briefly mention the main aim of the work and highlight the principal conclusions. As far as possible, please keep the introduction comprehensible to scientists outside your particular field of research.

Received 00 February 2100, revised 00 October 2100, accepted 00 October 2100
Corresponding author Firstname Lastname: +82-51-759-0656, e-mail@e-mail.com
It is a recommended paper from the proceedings of 2019 spring symposium of the Korea Marine Robot Technology (KMRTS).

2. General Information for Authors

2.1 Research and Publication Ethics

Authorship should be limited to those who have made a significant contribution to the conception, design, execution, or interpretation of the reported study. All those who have made significant contributions should be listed as co-authors. Where there are others who have participated in certain substantive aspects of the research project, they should be acknowledged or listed as contributors.

The corresponding author should ensure that all appropriate co-authors and no inappropriate co-authors are included on the paper, and that all co-authors have seen and approved the final version of the paper and have agreed to its submission for publication.

Details on publication ethics are found in the journal's website (http://joet.org/authors/ethics.php). For the policies on research and publication ethics not stated in the Instructions, Guidelines on Good Publication (http://publicationethics.org/) can be applied.

2.2 Requirement for Membership

One of the authors who submits a paper or papers should be member of The Korea Society of Ocean Engineers (KSOE), except a case that editorial board provides special admission of submission.

2.3 Publication Type

Article types include scholarly monographs (original research articles), technical articles (technical reports and data), and review articles. The paper should have not been submitted to another academic journal. When part or whole of a manuscript was already published to conference papers, research reports, and dissertations, then the corresponding author should note it clearly in the manuscript.

Example: It is noted that this paper is revised edition based on proceedings of KAOST 2100 in Jeju.

2.4 Copyright

After published to JOET, the copyright of manuscripts should belong to KSOE. A transfer of copyright (publishing agreement) form can be found in submission website (http://www.joet.org).

2.5 Manuscript Submission

Manuscript should be submitted through the on-line submission website (http://www.joet.org). The date that manuscript was received through on-line website is the official date of receipt. Other correspondences can be sent by an email to the Editor in Chief or secretariat. The manuscript must be accompanied by a signed statement that it has been neither published nor currently submitted for publication elsewhere. The manuscript should be written in English or Korean. Ensure that online submission is in a standard word processing format. Corresponding author must write the manuscript using the JOET template provided in Hangul or MS Word format. Ensure that graphics are high-resolution. Be sure all necessary files have been uploaded/ attached.

2.5.1 Authoer’s checklist

Authoer’s checklist and Transfer of copyright can be found in submission homepage (http:/www.joet.org).

3. Manuscript

Manuscript must be edited in the following order: (1) Title, (2) Authors' names and affiliations, (3) Keywords, (4) Abstract, (5) Nomenclature (optional), (6) Introduction, (7) Main body (analyses, tests, results, and discussions), (8) Conclusions, (9) Conflict of interest, (10) Funding (optional), (11) Acknowledgements (optional), (12) References, (13) Appendices (optional), (14) Author’s ORCIDs.

3.1 Unit

Use the international system units (SI). If other units are mentioned, please give their equivalent in SI.

3.2 Equations

All mathematical equations should be clearly printed/typed using well accepted explanation. Superscripts and subscripts should be typed clearly above or below the base line. Equation numbers should be given in Arabic numerals enclosed in parentheses on the right-hand margin. The parameters used in equation must be defined. They should be cited in the text as, for example, Eq. (1), or Eqs. (1)–(3).

$$G_{GEV}(x;\mu,\sigma,\xi)=\begin{cases}\exp[-(1+\xi(x-\mu)/\sigma)^{-1/\xi}] & \xi\neq 0\\ \exp[-\exp(-(x-\mu)/\sigma)] & \xi=0\end{cases} \quad (1)$$

in which μ, σ, and ξ represent the location ("Shift" in figures), scale, and shape parameters, respectively.

3.3 Tables

Tables should be numbered consecutively with Arabic numerals. Each table should be typed on a separate sheet of paper and be fully titled. All tables should be referred to in the texts.

Table 1 Tables should be placed in the main text near to the first time they are cited

Item	Buoyancy riser
Segment length[1)] (m)	370
Outer diameter (m)	1.137
Inner diameter (m)	0.406
Dry weight (kg/m)	697
Bending rigidity ($N\cdot m^2$)	1.66E8
Axial stiffness (N)	7.098E9
Inner flow density ($kg\cdot m^3$)	881
Seabed stiffness ($N/m/m^2$)	6,000

[1)]Tables may have a footer.

3.4 Figures

Figures should be numbered consecutively with Arabic numerals. Each figure should be fully titled. All the illustrations should be of high quality meeting with the publishing requirement with legible symbols and legends. All figures should be referred to in the texts. They should be referred to in the text as, for example, Fig. 1, or Figs. 1−3.

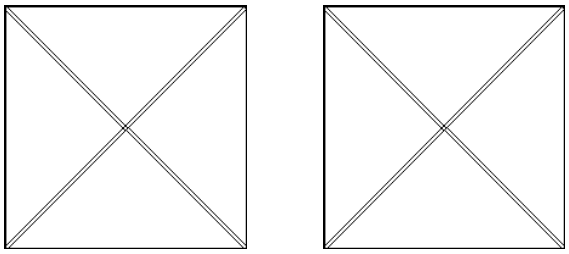

(a) (b)

Fig. 1 Schemes follow the same formatting. If there are multiple panels, they should be listed as: (a) Description of what is contained in the first panel; (b) Description of what is contained in the second panel. Figures should be placed in the main text near to the first time they are cited

3.5 How to Describe the References in Main Texts

- JOET recommends to edit authors' references using MS-Word reference or ZOTERO plug-in
- How to add a new citation and source to a document using MS-Word is found in MS Office web page: https://support.microsoft.com/en-us/office/add-citations-in-a-word-document-ab9322bb-a8d3-47f4-80c8-63c06779f127
- How to add a new citation and source to a document using ZOTERO is found in zotero web page: https://www.zotero.org/

4. Results

This section may be divided by subheadings. It should provide a concise and precise description of the experimental results, their interpretation as well as the experimental conclusions that can be drawn. Tables and figures are recommended to present the results more rapidly and easily. Do not duplicate the content of a table or a figure with in the Results section. Briefly describe the core results related to the conclusion in the text when data are provided in tables or in figures. Supplementary results can be placed in the Appendix.

5. Discussion

Authors should discuss the results and how they can be interpreted in perspective of previous studies and of the working hypotheses. The findings and their implications should be discussed in the broadest context possible. Future research directions may also be highlighted

6. Conclusions

This section can be added to the manuscript.

Conflict of Interest

It should be disclosed here according to the statement in the Research and publication ethics regardless of existence of conflict of interest. If the authors have nothing to disclose, please state: “No potential conflict of interest relevant to this article was reported.”, “The authors declare no potential conflict of interest.”, “The authors declare that they have no conflict of interests.”

Funding (Optional)

Please add: “This research was funded by Name of Funder, grant number XXX” and “The OOO was funded by XXX”. Check carefully that the details given are accurate and use the standard spelling of funding agency names at https://search.crossref.org/funding

Acknowledgments (Optional)

In this section you can acknowledge any support given which is not covered by the author contribution or funding sections. This may include administrative and technical support, or donations in kind (e.g., materials used for experiments). For mentioning any persons or any organizations in this section, there should be a written permission from them.

References

JOET follows the American Psychological Association (APA) style.

- Some samples are found in following web pages: https://apastyle.apa.org/style-grammar-guidelines/references/examples or https://www.ntnu.edu/viko/apa-examples
- JOET recommends editing authors’ references using MS-Word reference or ZOTERO plug-in
- How to add a new citation and source to a document using MS-Word is found in MS Office web page: https://support.microsoft.com/en-us/office/add-citations-in-a-word-document-ab9322bb-a8d3-47f4-80c8-63c06779f127
- How to add a new citation and source to a document using ZOTERO is found in ZOTERO web page: https://www.zotero.org/

Appendix (Optional)

The appendix is an optional section that can contain details and data supplemental to the main text. For example, explanations of experimental details that would disrupt the flow of the main text, but nonetheless remain crucial to understanding and reproducing the research shown; figures of replicates for experiments of which representative data is shown in the main text can be added here if brief, or as Supplementary data. Mathematical proofs of results not central to the paper can be added as an appendix.

All appendix sections must be cited in the main text. In the appendixes, Figures, Tables, etc. should be labeled starting with ‘A’, e.g., Fig. A1, Fig. A2, etc.

Examples:

https://doi.org/10.26748/KSOE.2019.022

https://doi.org/10.26748/KSOE.2018.4.32.2.095

Author ORCIDs

All authors are recommended to provide an ORCID. To obtain an ORCID, authors should register in the ORCID web site: http://orcid.org. Registration is free to every researcher in the world. Example of ORCID description is as follows:

Author name	**ORCID**
So, Hee	0000-0000-000-00X
Park, Hye-Il	0000-0000-000-00X
Yoo, All	0000-0000-000-00X
Jung, Jewerly	0000-0000-000-00X

Authors' Checklist

The following list will be useful during the final checking of a manuscript prior to sending it to the journal for review. Please submit this checklist to the KSOE when you submit your article.

< Checklist for manuscript preparation >

☐ I checked my manuscript has been 'spell-checked' and 'grammar-checked'.

☐ One author has been designated as the corresponding author with contact details such as
- E-mail address
- Phone numbers

☐ I checked abstract 1) stated briefly the purpose of the research, the principal results and major conclusions, 2) was written in 150−200 words, and 3) did not contain references (but if essential, then cite the author(s) and year(s)).

☐ I provided 5 or 6 keywords.

☐ I checked color figures were clearly marked as being intended for color reproduction on the Web and in print, or to be reproduced in color on the Web and in black-and-white in print.

☐ I checked all table and figure numbered consecutively in accordance with their appearance in the text.

☐ I checked abbreviations were defined at their first mention there and used with consistency throughout the article.

☐ I checked all references mentioned in the Reference list were cited in the text, and vice versa according to the APA style.

☐ I checked I used the international system units (SI) or SI-equivalent engineering units.

< Authorship checklist >

JOET considers individuals who meet all of the following criteria to be authors:

☐ Made a significant intellectual contribution to the theoretical development, system or experimental design, prototype development, and/or the analysis and interpretation of data associated with the work contained in the article.

☐ Contributed to drafting the article or reviewing and/or revising it for intellectual content.

☐ Approved the final version of the article as accepted for publication, including references.

< Checklist for publication ethics >

☐ I checked the work described has not been published previously (except in the form of an abstract or as a part of a published lecture or academic thesis).

☐ I checked when the work described has been published previously in other proceedings without copyright, it has clearly noted in the text.

☐ I checked permission has been obtained for use of copyrighted material from other sources including the Web.

☐ I have processed Plasgiarism Prevention Check through reliable web sites such as www.kci.go.kr, http://www.ithenticate.com/, or https://www.copykiller.org/ for my submission.

☐ I agree that final decision for my final manuscript can be changed according to results of Plasgiarism Prevention Check by JOET administrator.

☐ I checked one author at least is member of the Korean Society of Ocean Engineers.

☐ I agreed all policies related to 'Research and Publication Ethics'

☐ I agreed to transfer copyright to the publisher as part of a journal publishing agreement and this article will not be published elsewhere including electronically in the same form, in English or in any other language, without the written consent of the copyright-holder.

☐ I made a payment for reviewing of the manuscript, and I will make a payment for publication on acceptance of the article.

☐ I have read and agree to the terms of Authors' Checklist.

Title of article	:	
Date of submission	: DD/MM/YYYY	
Corresponding author	:	signature
Email address	:	

※ E-mail this with your signature to ksoehj@ksoe.or.kr

Publishing Agreement

ARTICLE DETAILS

Title of article :

Corresponding author :

E-mail address :

DOI : https://doi.org/10.26748/KSOE.2XXX.XXX

YOUR STATUS

I am one author signing on behalf of all co-authors of the manuscript.

ASSIGNMENT OF COPYRIGHT

I hereby assign to the Korean Society of Ocean Engineers, the copyright in the manuscript identified above and any tables, illustrations or other material submitted for publication as part of the manuscript (the "Article"). This assignment of rights means that I have granted to Korean Society of Ocean Engineers the exclusive right to publish and reproduce the Article, or any part of the Article, in print, electronic and all other media (whether now known or later developed), in any form, in all languages, throughout the world, for the full term of copyright, and the right to license others to do the same, effective when the Article is accepted for publication. This includes the right to enforce the rights granted hereunder against third parties.

SCHOLARLY COMMUNICATION RIGHTS

I understand that no rights in patents, trademarks or other intellectual property rights are transferred to the Journal owner. As the author of the Article, I understand that I shall have: (i) the same rights to reuse the Article as those allowed to third party users of the Article under the CC-BY-NC License, as well as (ii) the right to use the Article in a subsequent compilation of my works or to extend the Article to book length form, to include the Article in a thesis or dissertation, or otherwise to use or re-use portions or excerpts in other works, for both commercial and non-commercial purposes. Except for such uses, I understand that the assignment of copyright to the Journal owner gives the Journal owner the exclusive right to make or sub-license commercial use.

USER RIGHTS

The publisher will apply the Creative Commons Attribution-Noncommercial Works 4.0 International License (CC-BY-NC) to the Article where it publishes the Article in the journal on its online platforms on an Open Access basis.

The CC-BY-NC license allows users to copy and distribute the Article, provided this is not done for commercial purposes and further does not permit distribution of the Article if it is changed or edited in any way, and provided the user gives appropriate credit (with a link to the formal publication through the relevant DOI), provides a link to the license, and that the licensor is not represented as endorsing the use made of the work. The full details of the license are available at http://creativecommons.org/licenses/by-nc/4.0/legalcode.

REVERSION OF RIGHTS

Articles may sometimes be accepted for publication but later rejected in the publication process, even in some cases after public posting in "Articles in Press" form, in which case all rights will revert to the author.

☑ I have read and agree to the terms of the Journal Publishing Agreement.

Corresponding author:

name signature

※ E-mail this with your signature to ksoehj@ksoe.or.kr (Papers will not be published unless this form is signed and returned)

(사)한국해양공학회 특별회원

한국해양공학회의 특별회원은 다음과 같으며, 귀사의 찬조에 진심으로 감사드립니다.(순서: 입회순)

한국선급 / 현대중공업㈜ / 한화오션 / 선박해양플랜트연구소 /
대양전기공업㈜ / ㈜대영엔지니어링 / 한국조선해양기자재연구원 /
한국조선해양플랜트협회 / ㈜파나시아 / 선보공업㈜ / SK에코플랜트㈜ /
삼성중공업㈜ / ㈜유에스티21 / ㈜해양정보기술 / ㈜이앤코 / ㈜포스코

한국해양공학회 특별회원 가입방법은 학회홈페이지(www.ksoe.or.kr)의
입회안내를 참고하시고, 기타사항은 학회 사무국으로 연락주시기 바랍니다.

Research and Publication Ethics

Journal of Ocean Engineering and Technology (JOET) adheres to the guidelines published by professional organizations, including Committee on Publication Ethics (COPE; https://publicationethics.org/)

1. Authorship

JOET considers individuals who meet all of the following criteria to be authors:

1) Made a significant intellectual contribution to the theoretical development, system or experimental design, prototype development, and/or the analysis and interpretation of data associated with the work contained in the article.
2) Contributed to drafting the article or reviewing and/or revising it for intellectual content.
3) Approved the final version of the article as accepted for publication, including references.

Contributors who do not meet all of the above criteria may be included in the Acknowledgment section of the article. Omitting an author who contributed to your article or including a person who did not fulfill all of the above requirements is considered a breach of publishing ethics.

Correction of authorship after publication: JOET does not correct authorship after publication unless a mistake has been made by the editorial staff.

2. Originality and Duplicate Publication

All submitted manuscripts should be original and should not be in consideration by other scientific journals for publication. Any part of the accepted manuscript should not be duplicated in any other scientific journal without permission of the Editorial Board, although the figures and tables can be used freely if the original source is verified according to the Creative Commons Attribution License (CC BY-NC). It is mandatory for all authors to resolve any copyright issues when citing a figure or table from other journal that is not open access.

3. Conflict-of-Interest Statement

Conflict of interest exists when an author or the author's institution, reviewer, or editor has financial or personal relationships that inappropriately influence or bias his or her actions. Such relationships are also known as dual commitments, competing interests, or competing loyalties. These relationships vary from being negligible to having a great potential for influencing judgment. Not all relationships represent true conflict of interest. On the other hand, the potential for conflict of interest can exist regardless of whether an individual believes that the relationship affects his or her scientific judgment. Financial relationships such as employment, consultancies, stock ownership, honoraria, and paid expert testimony are the most easily identifiable conflicts of interest and the most likely to undermine the credibility of the journal, the authors, or of the science itself. Conflicts can occur for other reasons as well, such as personal relationships, academic competition, and intellectual passion. If there are any conflicts of interest, authors should disclose them in the manuscript. The conflicts of interest may occur during the research process as well; however, it is important to provide disclosure. If there is a disclosure, editors, reviewers, and reader can approach the manuscript after understanding the situation and the background of the completed research.

4. Management Procedures for the Research and Publication Misconduct

When JOET faces suspected cases of research and publication misconduct such as a redundant (duplicate) publication, plagiarism, fabricated data, changes in authorship, undisclosed conflicts of interest, an ethical problem discovered with the submitted manuscript, a reviewer who has appropriated an author's idea or data, complaints against editors, and other issues, the resolving process will follow the flowchart provided by the Committee on Publication Ethics (http://publicationethics.org/resources/flowcharts). The Editorial Board of JOET will discuss the suspected cases and reach a decision. JOET will not hesitate to publish errata, corrigenda, clarifications, retractions, and apologies when needed.

5. Editorial Responsibilities

The Editorial Board will continuously work to monitor and safeguard publication ethics: guidelines for retracting articles; maintenance of the integrity of the academic record; preclusion of business needs from compromising intellectual and ethical standards; publishing corrections, clarifications, retractions, and apologies when needed; and excluding plagiarism and fraudulent data. The editors maintain the following responsibilities: responsibility and authority to reject and accept articles; avoiding any conflict of interest with respect to articles they reject or accept; promoting publication of corrections or retractions when errors are found; and preservation of the anonymity of reviewers.

6. Hazards and human or animal subjects

If the work involves chemicals, procedures or equipment that have any unusual hazards inherent in their use, the author must clearly identify these in the manuscript. If the work involves the use of animal or human subjects, the author should ensure that the manuscript contains a statement that all procedures were performed in compliance with relevant laws and institutional guidelines and that the appropriate institutional committee(s) has approved them. Authors should include a statement in the manuscript that informed consent was obtained for experimentation with human subjects. The privacy rights of human subjects must always be observed.

Ensure correct use of the terms sex (when reporting biological factors) and gender (identity, psychosocial or cultural factors), and, unless inappropriate, report the sex and/or gender of study participants, the sex of animals or cells, and describe the methods used to determine sex and gender. If the study was done involving an exclusive population, for example in only one sex, authors should justify why, except in obvious cases. Authors should define how they determined race or ethnicity and justify their relevance.

7. Secondary publication

It is possible to republish manuscripts if the manuscripts satisfy the conditions of secondary publication. These are:

- The authors have received approval from the Editorial Board of both journals (the editor concerned with the secondary publication must have access to the primary version).
- The priority for the primary publication is respected by a publication interval negotiated by editors of both journals and the authors.
- The paper for secondary publication is intended for a different group of readers
- The secondary version faithfully reflects the data and interpretations of the primary version.
- The secondary version informs readers, peers, and documenting agencies that the paper has been published in whole or in part elsewhere, for example, with a note that might read, "This article is based on a study first reported in the [journal title, with full reference]"
- The title of the secondary publication should indicate that it is a secondary publication (complete or abridged republication or translation) of a primary publication.

8. Complaints and Appeals

The process of handling complaints and appeals follows the guidelines of the COPE available from: https://publicationethics. org/appeals

9. Post-publication discussions and corrections

The post-publication discussion is available through letter to editor. If any readers have a concern on any articles published, they can submit letter to editor on the articles. If there found any errors or mistakes in the article, it can be corrected through errata, corrigenda, or retraction.

The Korean Society of Ocean Engineers